Master of Science Thesis

Aerodynamic Investigation of an Exit Guide Vane Followed by a Curved Duct

A Numerical Study

O. F. Pfeifle

Delft University of Technology

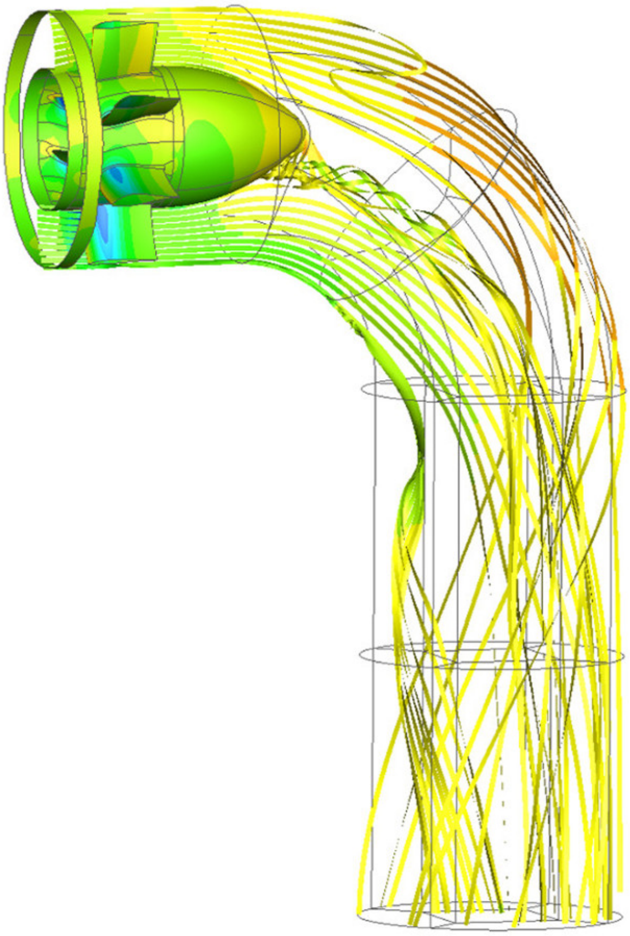

Faculty of Aerospace Engineering · Delft University of Technology

Aerodynamic Investigation of an Exit Guide Vane Followed by a Curved Duct

A Numerical Study

Master of Science Thesis

For obtaining the degree of Master of Science in Aerospace Engineering
at Delft University of Technology,
to be defended publicly on Thursday November 23, 2017

O. F. Pfeifle

Faculty of Aerospace Engineering · Delft University of Technology

The work in this thesis was supported by MTU Aero Engines. Their cooperation is gratefully acknowledged.

Delft University of Technology
Faculty of Aerospace Engineering
Department of Flight Performance and Propulsion

GRADUATION COMMITTEE

To be defended on: 23.11.2017

Committee members:

Dr. ir. A.G. Rao

Dr. ir. F.F.J. Schrijer

Dr. ir. M. Pini

ir. S. Vitale

Thesis number: 170#17#MT#FPP

Abstract

Curved exhaust ducts are used in aero engine applications for different purposes, including thrust vectoring, shielding of parts from the exhaust or improving stealth properties. Their integration, however, regularly represents a design problem due to flow separation and high aerodynamic losses occurring in the bend. Curved duct flows for both compressible and incompressible conditions have been studied extensively in the past. However, no experimental results of a high Reynolds number flow through a turbine exit guide vane (EGV) followed by a curved duct have yet been published. An in-depth CFD analysis of the aerodynamic effects is therefore carried out, using the RANS solvers TRACE (at MTU Aero Engines) and SU2, to analyze the flow field and geometric sensitivities of a high Reynolds number flow through an EGV followed by a 90° bent duct. The geometry of interest is investigated at a Reynolds number of $Re = 10^6$ and a ratio of bend radius to duct diameter of $R_c/D \sim 1$. The inflow conditions are prescribed to closely resemble typical flow conditions at the low pressure turbine exit plane of a turbojet engine.

After validating the solver with experimental data using the test case of an 90° duct, an initial CFD analysis of the combined exit guide vane geometry with curved duct is carried out to identify the dominant flow phenomena and mutual effects of the EGV and the bend. Three zones of flow separations are found, each at the convex and concave sides of the bend and one at the lower side of the plug. Secondary flows caused by the bend are found to have an effect on the flow upstream of the EGV, leading to a non-uniform flow inlet angle and aerodynamic loading of the individual blades. Separation downstream of the EGV is influenced by the presence of low velocity wakes from the EGV.

Subsequently, a sensitivity study is carried out to find the effect of different geometrical parameters on the flow field. Main investigated parameters are the ratio of bend radius to diameter R_c/D and the distance between EGV and bend, l/D. Additionally, the aerodynamic effects of the circumferential EGV positioning, swirl and the plug shape are investigated. It is found that an increase in both R_c/D and l/D improves aerodynamic efficiency, while swirl can decrease pressure losses in the duct for small bend radii of $R_c/D < 0.8$. Improving the plug shape and rotating the EGV allows to further increase the aerodynamic efficiency without weight increase. For further optimization of the geometry, it is recommended to include duct geometries with a non-constant bend radius and outer duct diameter to increase the design space.

Nomenclature

Symbols

c	chord length of exit guide vanes [m]
c_1	absolute velocity at EGV inlet [$\frac{m}{s}$]
c_2	absolute velocity at EGV exit [$\frac{m}{s}$]
c_p	pressure coefficient [-]
D	pipe diameter [m]
E	turbulent kinetic energy [$\frac{J}{kg}$]
e	internal energy per unit mass [$\frac{J}{kg}$]
$\vec{F}^c$	vector of convective fluxes
$\vec{F}^v$	vector of viscous fluxes
De	Dean number [-]
k	turbulent kinetic energy [$\frac{J}{kg}$]
k_t	thermal conductivity constant [$\frac{kg \cdot m}{s^3 \cdot K}$]
l	distance between EGV and bend [m]
Ma	Mach number [-]
p	pressure [Pa]
$\bar{p}$	mean inlet pressure [Pa]
Q	source term
r	local duct radius [m]
R_c	bend radius of curvature [m]
R_i	inner duct radius [m]
R_o	outer duct radius [m]
Re	Reynolds number [-]
S_1, S_2, S_3	principle planes used for turbomachinery design
T	temperature [K]
$\bar{T}$	mean inlet temperature [K]
t	time [s]
U	state vector
u	absolute flow velocity [$\frac{m}{s}$]
$\bar{u}$	mean inlet velocity [$\frac{m}{s}$]
u'	velocity fluctuation [$\frac{m}{s}$]
$\vec{u}$	velocity vector in Cartesian coordinates (u_1, u_2, u_3) [$\frac{m}{s}$]
u^+	wall velocity scale [-]

u_τ	friction velocity $[\frac{m}{s}]$
x, y, z	Cartesian coordinates [m]
y^+	wall length scale [-]
α_1	swirl at EGV inlet [°]
α_2	swirl at EGV exit [°]
δ	Kronecker delta [-]
ϵ	turbulence dissipation $[\frac{m^2}{s^3}]$
θ	angular position on duct cross-section [°]
θ_{EGV}	circumferential alignment of EGV ($\theta = 0°$ for symmetry with $y = 0$) [°]
κ	Van Karman constant [-]
λ	relative streamwise total pressure [-]
μ	dynamic viscosity $[\frac{kg}{s \cdot m}]$
ν	kinematic viscosity $[\frac{m^2}{s}]$
ν_t	turbulent viscosity $[\frac{m^2}{s}]$
ρ	density $[\frac{kg}{m^3}$
τ	shear stress $[\frac{N}{m^2}]$
τ_w	wall shear stress $[\frac{N}{m^2}]$
ϕ	angular position along duct bend [°]
ω	specific turbulence dissipation $[\frac{1}{s}]$
ζ_v	pressure loss coefficient [-]
$DC60$	60° distortion coefficient
$SC60$	60° swirl coefficient

Subscripts

x, y, z	Cartesian coordinate indices
i, j, k	Einstein summation indices
inl	at duct inlet
max	maximum
rel	relative, non-dimensionalized by dividing through base geometry value
t	total
ϕ	circumferential
60	60° segment

Abbreviations

AIP	Aerodynamic Interface Plane
CFD	Computational Fluid Dynamics
EGV	Exit Guide Vane
LPT	Low Pressure Turbine
TU Delft	Delft University of Technology

Table of Contents

Nomenclature **ix**

Preface **xix**

1 Introduction **1**

2 Literature Review **5**
- 2.1 Turbulent, wall-bounded flows . . . 5
- 2.2 Curved duct flows . . . 8
- 2.3 Sensitivity studies . . . 13

3 Methodology **15**
- 3.1 Research design . . . 15
  - 3.1.1 Research question . . . 16
  - 3.1.2 Research objective . . . 16
  - 3.1.3 Reference system . . . 18
  - 3.1.4 Assumptions . . . 19
  - 3.1.5 Boundary conditions . . . 20
  - 3.1.6 In- and Output parameters . . . 21
  - 3.1.7 Research procedure . . . 22
- 3.2 2D and quasi-3D methods . . . 22
  - 3.2.1 Quasi-3D streamline curvature analysis . . . 24
  - 3.2.2 2D Euler analysis . . . 25
- 3.3 3D Modeling and RANS calculation . . . 25
  - 3.3.1 Preprocessing . . . 26
  - 3.3.2 RANS calculation . . . 36
  - 3.3.3 Post-processing . . . 39
- 3.4 Grid convergence . . . 40
- 3.5 Validation . . . 41
- 3.6 Limitations . . . 45

4 Results **47**

4.1 EGV with straight vs curved duct . . . 47

4.1.1 Flow through an EGV followed by a straight duct . . . 47

4.1.2 Flow phenomena in the curved duct . . . 48

4.1.3 Upstream effect of the curved duct . . . 53

4.1.4 Exit guide vane effect on curved duct flow . . . 55

4.2 Sensitivity study . . . 56

4.2.1 Radius of curvature . . . 56

4.2.2 Effect of bend radius on flow symmetry . . . 59

4.2.3 Distance between the EGV and the bend . . . 60

4.2.4 Effect of swirl . . . 62

4.2.5 Circumferential EGV positioning . . . 65

4.2.6 Plug shape . . . 67

4.3 Comparison of SU2 with TRACE results . . . 69

5 Conclusion and Recommendations **73**

5.1 Conclusion . . . 73

5.2 Recommendations . . . 74

References **75**

List of Figures

1.1 R79V-300 turbojet engine with variable exit geometry for VTOL capabilities [1] . 1

1.2 Last stage of the low pressure turbine (left), followed by EGV and duct with exhaust plug. Exhaust flow is finally accelerated in the converging nozzle (right) [2] 2

1.3 Straight and curved exhaust duct after exit guide vane (from MTU project proposal) 2

1.4 Functional breakdown diagram for a turbojet/turbofan exhaust geometry. Functions applying to a constant-area exhaust (without nozzle) are indicated in grey . 3

2.1 Turbulent kinetic energy distribution $E(k)$ over large, inertial and small scales ($E = \frac{1}{2}\overline{u'^2_i}$, k= wave number) 6

2.2 Typical velocity profile and turbulence production/dissipation in turbulent wall-bounded flows [3] 7

2.3 Dean vortices at the outlet of a curved pipe (right side is concave wall of bend) [4] 9

2.4 LES simulation showing Dean vortices at the outlet of a curved duct (right side is concave wall of bend) [5] 9

2.5 Development of secondary flows in a pipe bend showing (a) the adverse pressure gradient on concave and convex walls and (b) the direction of the secondary flow [6] 9

2.6 Streamwise distribution of wall static pressure along convex (In), concave (Out) and side (Bottom) walls of a 90° elbow duct with circular cross-section [7], starting from a distance equal to the duct diameter ($1\,D$) upstream of the bend until five diameters ($5\,D$) downstream of the bend. 10

2.7 Distribution of time mean longitudinal velocity $\overline{W}$ at different sections along a circular 90° elbow duct [7] 11

2.8 Time-averaged velocity field near the inside wall in an elbow duct obtained from PIV measurements showing flow separation and reattachment [8] 11

2.9 Experimental results for velocity profile after elbow bend at different streamwise positions. Definitions of the aerodynamic interface planes (AIPs) used for the measurements are given in Fig. 3.25 12

3.1 Definition of principle directions in the Cartesian coordinate system 18

3.2 Definition of swirl α, view from casing towards hub 19
3.3 Definition of ϕ, indicating location of cross-section through the bend 19
3.4 Inlet boundary conditions for total pressure p_t, temperature T_t and swirl α. Temperature and pressure are non-dimensionalized for reasons of confidentiality. . . . 21
3.5 Schematic procedure for the aerodynamic investigation of an EGV followed by a curved duct 23
3.6 2D cut definitions in a blade row 24
3.7 Quasi-3D streamline solution for an EGV geometry with straight plug and exhaust duct, using streamline curvature analysis 24
3.8 Example Mach/pressure distribution and definition of zones for a turbine blade [9] 25
3.9 Structured mesh in curvilinear and uniform cartesion representation [10] 26
3.10 O-Grid (structured) [11] 27
3.11 C-Grid around an airfoil (structured) [11] 27
3.12 Multi-block structure for improved element quality [12] 28
3.13 Multi-block grid of a turbine stage [13] 29
3.14 Common element types used in unstructured 3D meshes 29
3.15 Hybrid mesh on a leading edge flap [14] 31
3.16 Structured multi-block mesh of single EGV passage 33
3.17 Fully structured duct meshes 33
3.18 Hybrid mesh consisting of O-grid and tetrahedral cells [15] 34
3.19 360° EGV geometry with eight vanes modeled in Autogrid 34
3.20 Final geometry and multi-block mesh topology 35
3.21 Mesh topology at the EGV spinner and the plug 35
3.22 Mesh topology at the Outlet face 36
3.23 Relative pressure loss factor $\zeta_{v_{rel}}$ and exit temperature $T_{2_{rel}}$ for meshes of different cell count (non-dimensionalized with results for 12 M cell mesh) 40
3.24 Non-dimensional streamwise velocity at $\phi = 0°$ for curved duct $(R_c/D = 1)$ using different mesh resolutions 41
3.25 Test case geometry of elbow duct and AIP definition for validation 42
3.26 TRACE and SU2 streamwise velocity results compared to experimental results for velocity profile after elbow bend at different streamwise positions (AIPs) for flat inlet profile 43
3.27 TRACE streamwise velocity results compared to experimental results for velocity profile after elbow bend at different streamwise positions (AIPs) for developed inlet profile 43
3.28 TRACE results compared to experimental results for secondary flow velocities $(u_{xy}/\overline{u})$ after elbow bend at different streamwise positions 44

4.1 Absolute flow velocity $u/\overline{u}$ at $y = 0$ for straight duct 48
4.2 Absolute flow velocity $u/\overline{u}$ at $y = 0$ for curved duct $(R_c/D = 1)$ 48
4.3 Velocity profiles for straight and curved duct at corresponding streamwise cross-sections (same mean-line duct legth) 49
4.4 Static pressure along concave and convex bend walls 49

4.5 Iso-surfaces of zero streamwise velocity showing zones of separation for $R_c/D = 1$ 50

4.6 Absolute flow velocity for curved duct ($R_c/D = 1$) and straight duct at the EGV exit - left for curved duct, right for straight duct 50

4.7 Boundary layer velocity profile at concave (Outer) and convex (Inner) walls at the 45° plane F 51

4.8 Upstream influence of Dean vortices on swirl distribution at the EGV inlet 53

4.9 Pressure distribution for individual vanes (angle corresponds to circumferential position around x-axis) (a) and vane numbering (b) 53

4.10 Asymmetry parameters $DC60$ and $SC60$ at different aerodynamic interface planes 54

4.11 Influence of exit guide vane wake on the boundary layer at the EGV exit plane C . 55

4.12 Absolute flow velocity for different duct radii 56

4.13 Absolute flow velocity for different R_c/D at various positions along the duct. First row (**(a)**-**(c)**) at position $\phi = 30°$, second row (**(d)**-**(f)**) at $\phi = 90°$ 57

4.14 Turbulent viscosity for different duct radii 57

4.15 Velocity profiles for curved ducts of different R_c/D at corresponding streamwise cross-sections 58

4.16 Asymmetry parameters $DC60$ and $SC60$ at different aerodynamic interface planes 59

4.17 Pressure loss and inflow asymmetry shown for different combinations of R_c/D and l/D 61

4.18 Absolute flow velocity for different swirl angles at the EGV exit 62

4.19 Absolute flow velocity for curved duct ($R_c/D = 1$) without residual swirl (left) and with a residual swirl of $\alpha = 10°$ (right). First row (**(a)**-**(b)**) at position $\phi = 0°$, second row (**(c)**-**(d)**) at $\phi = 30°$ and third row (**(e)**-**(f)**) at $\phi = 90°$ 63

4.20 Effect of residual swirl on loss factor and streamwise total exit pressure for different R_c/D 64

4.21 Loss factor for different circumferential guide vane positioning (rotated around the x-axis by θ) 65

4.22 Absolute flow velocity for curved duct ($R_c/D = 1$) with symmetrical vane positioning (left) and $\theta_{EGV} = 17.5°$ (right) at different streamwise cross-sections (ϕ) . . . 66

4.23 Absolute flow velocity for different spinner geometries 67

4.24 Absolute flow velocity for standard plug, increased length plug and plug with pronounced upper curvature (columns left to right) at different streamwise positions (ϕ) along the bend 68

4.25 Absolute flow velocity obtained using the solvers SU2 and TRACE at $\phi = 0°$ . . . 69

4.26 Absolute flow velocity obtained using the solvers SU2 and TRACE at $y = 0$ 70

4.27 Comparison of circumferential $DC60$ distribution after the bend ($\phi = 90°$) for TRACE and SU2 70

List of Tables

2.1 Experimental and numerical studies on flows through circular 90° pipe bends . . . 8

3.1 Boundary conditions for closed problem formulation 20
3.2 Independent geometric design variables leading to a parametric geometry of the exhaust system 21
3.3 Point of reattachment, given downstream of the bend for flat inlet profile 44
3.4 Effect of swirl in a curved duct on total pressure loss and streamwise total pressure 45

4.1 Pressure losses in the combined geometry with either a straight or a curved duct . 52
4.2 Pressure losses for different radii of curvature 59
4.3 Pressure losses for different distances between the EGV and the bend, l/D 60
4.4 Total loss factors with and without complete swirl removal by the EGV 64
4.5 Pressure losses for individual plug shapes 67
4.6 Pressure losses obtained from TRACE and SU2 71

Preface

I would like to thank my supervisor Dr. ir. A.G. Rao at the Faculty of Aerospace Engineering at the TU Delft and Dr. ir. G. Ramm from MTU Aero Engines for their continuous assistance and support during the writing of this thesis as well as ir. S. Vitale for his valuable help regarding the SU2 solver. Many hours of meetings and conversations, both at the TU Delft and at MTU Aero Engines in Munich, contributed to the work in this report. Without your support and experience this work would not have been possible.

O. Pfeifle
Delft, November 2017

Chapter 1

Introduction

Most turbojet and turbofan engines nowadays employ a purely axial layout with thrust being provided in the direction of flight. However, for certain engine applications a deflection of the thrust is required. Curved exhausts ducts have been applied for a number of different applications, including thrust-vectoring, VTOL capabilities (Fig. 1.1), directing hot gases away from structural components or to decrease the engine's infrared signature. Similarly, for marine and industrial ground-based gas turbine applications, low pressure turbines are often coupled with a curved exhaust duct or gas collector. This can be the case where due to the setup of a power plant, thermodynamic cycle, space requirements or preferred exhaust direction, a deflection of the exhaust gases is desired.

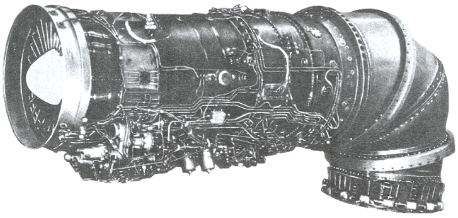

Figure 1.1: R79V-300 turbojet engine with variable exit geometry for VTOL capabilities [1]

The low pressure turbine in a two-spool aero engine is situated after the high pressure turbine and delivers shaft power, used to drive a compressor or generator. In a standard turbine configuration the last turbine stage is usually followed by an exit guide vane, consisting of a number of large airfoils positioned in the flow at evenly spaced locations. The exit guide vanes provide structural integrity and also remove swirl left in the flow after the last turbine stage. An exhaust plug is often connected at the inner wall, after the turbine outlet to gradually transform the annular cross-section of the turbine outlet into the circular cross-section of the nozzle. The outer duct wall usually forms a circular duct, but can be conical or straight. The exhaust plug after the EGV and the duct should be designed such that separation along the walls due to flow diffusion is avoided. The geometry of an EGV with exhaust plug and nozzle is schematically shown in Fig. 1.2 for the example of a turbojet engine.

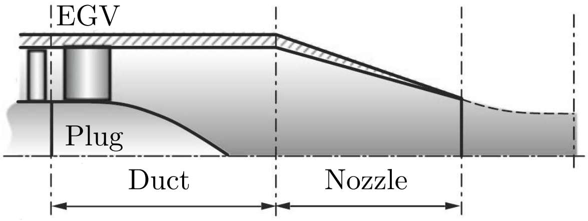

Figure 1.2: Last stage of the low pressure turbine (left), followed by EGV and duct with exhaust plug. Exhaust flow is finally accelerated in the converging nozzle (right) [2]

Including a curved exhaust duct in an aero engine can have a significant impact on the overall engine performance. When situated after the turbine exit guide vane (EGV) and including a plug geometry as indicated in Fig. 1.2, a curved exhaust can lead to significant flow separation, pressure losses and asymmetric flow through the EGV. Investigating the influence of different geometrical parameters on the flow field in an EGV, followed by a curved duct, will help to minimize pressure losses and separation and provide valuable insight for future work and products. A numerical approach is used to simulate the flow and to carry out a sensitivity study on the exhaust and exit guide vane geometry. In the course of this numerical study, both the industry code TRACE [13] and the open-source code SU2 [16] are used. The initial geometry of a curved duct compared to a conventional straight duct, not including the nozzle section, is sketched in Fig. 1.3.

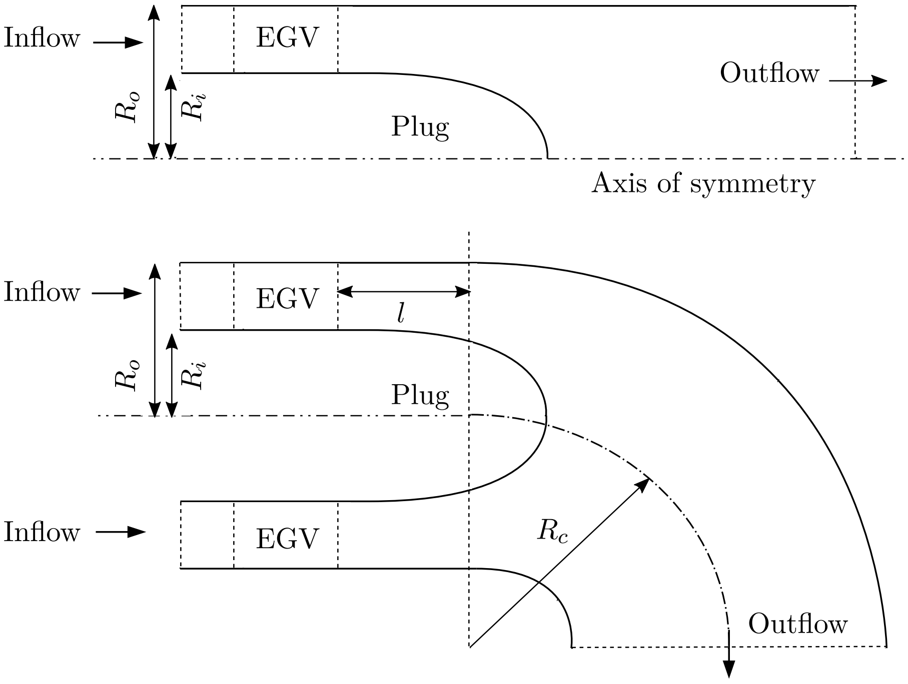

Figure 1.3: Straight and curved exhaust duct after exit guide vane (from MTU project proposal)

The main function of the nozzle in a turbojet or turbofan with low bypass ratio is to transform the static pressure that is left in the high temperature exhaust flow into kinetic energy by accelerating the flow and to regulate the overall engine performance and mass flow [2]. The functional breakdown diagram for a turbojet engine duct and nozzle configuration as shown in Fig. 1.2 is presented in Fig. 1.4. For a duct with constant cross-sectional area, not including the final nozzle geometry, only part of the functions of a complete exhaust and nozzle geometry apply. From the functional breakdown in Fig. 1.4 it can be concluded that the main functions of the curved exhaust will be the deflection of the flow and transformation from an annular to a circular cross-section with minimum pressure losses, removing any swirl left and providing a homogeneous flow profile at both the EGV and the exit. Secondary flow phenomena in the curved duct include counter-rotating Dean-vortices [17] and separation at the convex wall. A curved geometry therefore poses a number of challenges for an exhaust duct with the functions presented in Fig. 1.4.

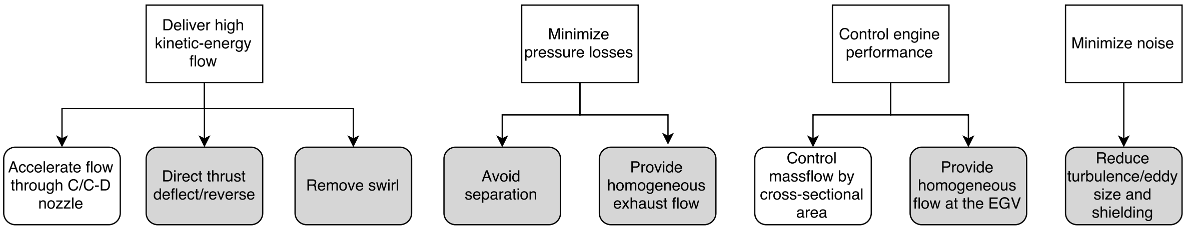

Figure 1.4: Functional breakdown diagram for a turbojet/turbofan exhaust geometry. Functions applying to a constant-area exhaust (without nozzle) are indicated in grey

The purpose of this research is to facilitate the future design of aero-engines employing a curved exit geometry by investigating the aerodynamic phenomena in an exit guide vane followed by a curved duct and performing a CFD-based sensitivity study. The research question is therefore to find out where pressure losses in an exit guide vane of a low pressure turbine followed by a 90° curved duct occur and how they can be minimized. For the numerical study, both the open-source code SU2 [16] and the industry turbomachinery CFD code TRACE [13] (developed at the german aerospace agency DLR) are used. After validating TRACE on an elbow duct test case, the combined geometry of EGV and duct is generated and discretized, using a structured multi-block mesh. TRACE is then used to analyze the flow phenomena occurring in the combined geometry, using both a straight and a curved duct to identify the effects of the bend. First, the influences of the EGV wake on flow separation within the duct are analyzed. In a next step, secondary flows caused by the bend (both upstream and downstream of the bend) are investigated. Finally, the effect of these secondary flows on the aerodynamic efficiency of the EGV is studied. A sensitivity study then shows the influence of bend radius and plug shape on the results and proposes improvements of the initial geometry.

The geometry optimization is limited by computational time and cost. The outer-diameter of the EGV and curved duct geometry is therefore kept constant during the analysis and a constant radius of curvature is used. With the shape of the individual vanes fixed, the variable parameters during the sensitivity study are: the bend radius R_c, the circumferential arrangement of the vanes, the plug shape and the distance between bend and EGV, l. Furthermore, unsteady effects from the low pressure turbine on the inlet conditions are assumed to be negligible. The inlet profile is taken as a fixed radial distribution of swirl, total pressure, total temperature and turbulence intensity. Non-reflecting boundary conditions are employed at inlet and outlet and the outlet static pressure adjusted to achieve a specified mass flow, leading to a complete set of boundary conditions. Independently changing the geometric variables during a sensitivity study allows to understand the dominant flow phenomena and to propose geometry improvements in order to minimize pressure losses and increase the overall engine efficiency.

Chapter 2

Literature Review

With the general problem laid out, this Chapter gives an overview about the work that has been carried out on the subject. It gives an impression of the current understanding and the methods employed in recent studies. First, some basics on turbulent, wall-bounded flows from literature are presented, before previous studies and recent work on curved duct flows are discussed. The last section takes a look at the meaning of sensitivity studies for aerodynamic shape optimizations.

2.1 Turbulent, wall-bounded flows

This section presents the basics of turbulent, wall-bounded flows, in order to give an overview of the terms and findings from previous research. Turbulent flows can generally be classified into free or isotropic turbulence, open jets and wall-bounded turbulence. Wall-bounded turbulence, usually encountered in internal flows, is shortly discussed in this section, including quantities that are used during the analysis. For more information on the topic, the reader is referred to the works of F. T. M. Nieuwstadt [18] and F. M. White [19] on turbulence and viscous flows.

Turbulent flows are three dimensional, rotational and show an intrinsic spatial and temporal complexity. They consist of a wide range of strongly interacting scales and are highly dissipative and diffusive. The turbulence structure with the largest dimensions is referred to as the macro-structure [18]. This large-scale turbulence extracts energy from the mean flow and carries the majority of turbulent kinetic energy. It is subjected to the macroscopic effects of the geometry and responsible for turbulence production. Only little dissipation occurs in this range of essentially inviscid flow. The macro-structure is therefore independent of Reynolds number and viscosity, making turbulence a property of the flow and not of the fluid [18].

The inertial subrange is independent of large and small scales. It is inviscid and transfers turbulent kinetic energy from large to small scales, where the transfer rate depends on the local wavelength. In 3D, vortex stretching is the prominent mechanism of energy transfer [19]. The small (Kolmogorov) scales are also known as the dissipation range. Turbulence is received from the larger scales and dissipated at the smallest scales due to the effects of viscosity. The large range of scales involved makes it a challenge to generate meshes that resolve all coherent structures in turbulent flows. Figure 2.1 illustrates the different scales as an energy cascade.

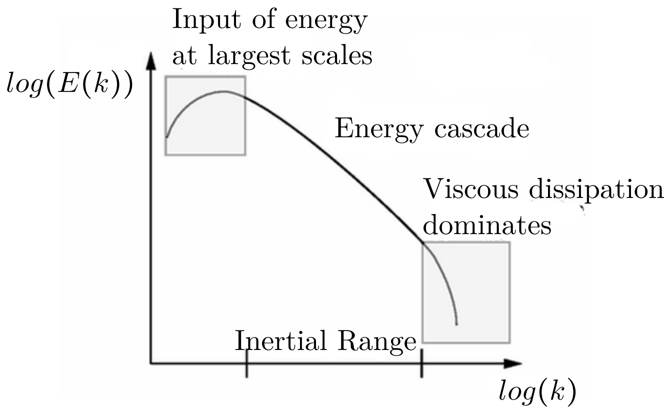

Figure 2.1: Turbulent kinetic energy distribution $E(k)$ over large, inertial and small scales ($E = \frac{1}{2}\overline{u'^2_i}$, $k=$ wave number)

Understanding the different scales of turbulence is essential in generating meshes with appropriate local cell sizes. Several non-dimensional parameters have been defined to quantify flow properties and distances close to the wall, where the mesh size is critical to obtaining reliable results. The friction or shear velocity (Equ. 2.1) is used to express a shear stress, such as the wall shear stress τ_w, in units of velocity. It allows to compare the flow velocity to a velocity that relates shear between flow layers. Using the friction velocity, the flow velocity and distance from the wall are non-dimensionalized and expressed using the wall units (Equ. 2.2 and 2.3).

$$u_\tau = \sqrt{\frac{\tau_w}{\rho}} \tag{2.1}$$

Wall units are a common way of expressing boundary layer flow profiles in a general way and are used to determine the required cell sizes of the first mesh layers to resolve the boundary layer flow. y^+ and u^+ represent the non-dimensionalized distance from the wall and flow velocity, respectively. Their understanding is essential in building a high-quality mesh that correctly resolves the boundary layer.

$$y^+ = \frac{y u_\tau}{\nu} \tag{2.2}$$

$$u^+ = \frac{u}{u_\tau} \tag{2.3}$$

Using the method of wall functions, the general velocity profile of a turbulent, wall-bounded flow over a flat plate can be analytically derived for the viscous sublayer, assuming a hydraulically smooth surface. The law of the wall is used to determine the u^+ distribution in the viscous sublayer (Equ. 2.4), followed by the logarithmic layer (Equ. 2.5). B and κ are constants, with κ also being known as the Van Karman constant. The outer layer is modeled using the law of the wake. More detailed information on wall functions is omitted here but can be found in Frank White's extensive work on viscous flows [19]. Most nowadays RANS CFD codes allow the use of wall functions at solid boundaries to obtain a first approximate solution without employing a high resolution grid to resolve the boundary layers. When using the generic velocity profiles provided by wall functions, the mesh can be considerably coarser at solid boundaries, saving computational time. In case the boundary layer is to be resolved for a more accurate and physical solution, information on the flow field or iteration is necessary to find the height required for the first cell to lie in the boundary layer. A value of $y^+ \sim 1$ for the cells directly adjacent to the solid boundary is usually desirable for a RANS calculation.

$$\text{Viscous sublayer: } \bar{u}^+ = y^+ \tag{2.4}$$

$$\text{Overlap/log layer: } \bar{u}^+ = \frac{1}{\kappa}\ln\left(y^+\right) + B \tag{2.5}$$

Figure 2.2 shows a typical velocity profile, together with the turbulence production and dissipation for turbulent wall-bounded flows. It can be seen how turbulent kinetic energy is mostly dissipated at the wall in the viscous sublayer. This distribution is influenced by the exit guide vane wake and pressure gradients from the curved geometry. Experiments concerning this effect have been conducted by E. Tulapurkara et al. in 2001 [20]. His findings are explained in Section 2.2 on secondary flow phenomena in curved ducts.

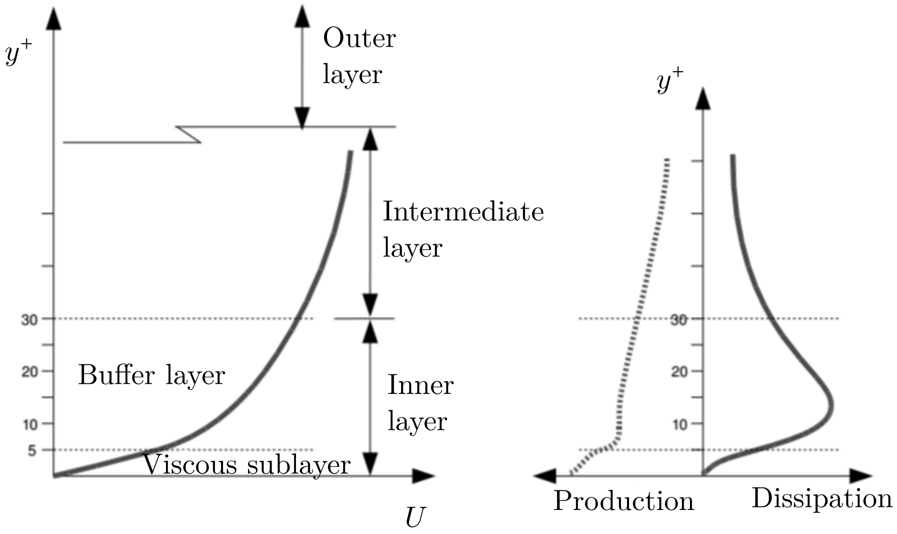

Figure 2.2: Typical velocity profile and turbulence production/dissipation in turbulent wall-bounded flows [3]

2.2 Curved duct flows

The flow of water, oil or gas through curved ducts has been the subject of numerous experimental and numerical studies, due to its wide range of applications in industry. Table 2.1 shows a number of experimental and numerical studies that have been carried out on the subject of a 90° bent pipe flow. The available experimental data is used to understand the dominant flow phenomena and to validate the numerical method. For Reynolds numbers above $2\text{x}10^5$ in an elbow (= 90° bend) pipe flow, it was shown by Fried and Idelchik in 1989 [21] that the total pressure loss coefficient remains constant with higher Reynolds numbers. The region of $Re > 2\text{x}10^5$ was therefore called the post-critical regime. The region of $Re < 10^5$ showed a larger value for the pressure loss and was called the sub-critical regime. In the transitional region between $Re = 10^5$ and $Re = 2\text{x}10^5$ the pressure loss coefficient shows a sudden decrease for higher Reynolds numbers [22]. This dependency of an elbow flow on the Reynolds number has to be taken into account when validating the numerical method with experimental data. In order to achieve dynamic similarity, the geometries of the numerical model and the reference experiment are selected to have a similar ratio of R_c/D. Reynolds similarity is achieved when the Reynolds numbers are in the same (post-critical) regime, where changes become negligible. Mach similarity finally ensures that the effects of compressibility are comparable.

Table 2.1: Experimental and numerical studies on flows through circular 90° pipe bends

Conductors	Method	Re	R_c/D [-]	D (m)	Working fluid
Kalpakli et al [23]	experimental	$2.4\text{x}10^4$	1.25	0.04	air
Enayet et al [24]	experimental	$4.3\text{x}10^4$	2.8	0.048	water
Ono et al [8]	experimental	$1.8\text{x}10^5$, $5.4\text{x}10^5$	1, 1.5	0.15	water
Kawamura et al [25]	experimental	$4\text{x}10^4$, $5\text{x}10^5$	0.55, 1, 2	0.1	water
Shiraishi et al [26]	experimental	$3.2\text{x}10^5 \sim 8.6\text{x}10^6$	1	0.413	water
Sudo et al [7]	experimental	$6\text{x}10^4$	2	0.104	air
Tan et al [5]	LES	$1\text{x}10^4$	1, 2	0.104	air
Pruvost et al [27]	$k-\epsilon$	$6\text{x}10^4$	2	0.104	air
Kim et al [28]	RNG $k-\epsilon$	$6\text{x}10^4$, $2\text{x}10^5$	2	0.104	air
Tanaka et al [22]	LES	500 - $1.47\text{x}10^7$	1, 2, 3	0.125	air

The secondary flow pattern of a Newtonian fluid in a curved pipe is governed by two counter-rotating Dean-vortices, named after W. R. Dean, who first wrote about their existence in 1959 [4]. Dean vortices are caused by the centrifugal forces and radial pressure distribution occurring in an elbow duct flow and have been the subject of extensive studies. In a 90° bend, Dean vortices have been shown to, after first increasing in strength, split up into a 4-cell complex at around 60° and decrease in strength towards the exit. This was shown by Mees et al. in 1996 [29] and confirmed by Ozaki et al. in a study on curvature effects in compressible flows in 2004 [30]. An example cross-sectional flow field from an LES analysis by Tan et al. from 2014 [5], showing the Dean vortices at the exit of a curved elbow duct, is given in Fig. 2.4.

Decreasing the mean radius of curvature has been shown to induce a strong increase in secondary flows transverse to the bulk velocity. This effect was shown during the studies of Ozaki et al. [30] and Muench et al. [31], using both experimental and numerical methods. The intensification was found to occur mainly due to the increase in radial pressure gradient

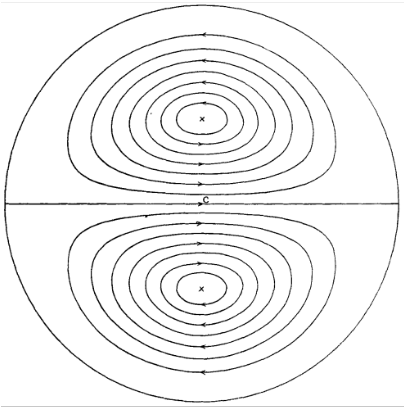

Figure 2.3: Dean vortices at the outlet of a curved pipe (right side is concave wall of bend) [4]

Figure 2.4: LES simulation showing Dean vortices at the outlet of a curved duct (right side is concave wall of bend) [5]

driving the secondary flows. An illustration of the secondary flow structures in a curved pipe is shown by Miller in his works on internal flow systems [6] (Fig. 2.5), together with the pressure gradients developing at the concave and convex walls.

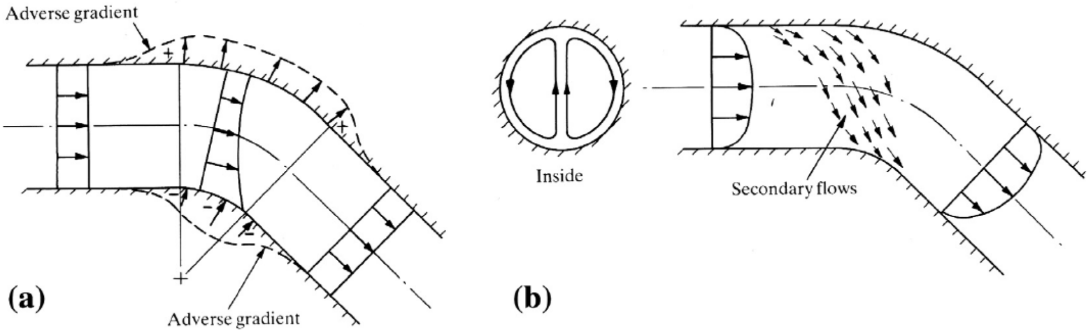

Figure 2.5: Development of secondary flows in a pipe bend showing (a) the adverse pressure gradient on concave and convex walls and (b) the direction of the secondary flow [6]

Different experimental studies confirm the existence of the pressure gradients along the duct walls, as can be seen by the experimental results presented in Fig. 2.6, obtained by Sudo et al. in 1998 [7] during an extensive study on turbulent flows in a circular-sectioned 90° bend. Large eddy simulations performed by Muench et al. in 2007 investigated the boundary layer behavior in a curved duct and found that the adverse streamwise pressure gradient decreases u^+ and induces a lower logarithmic behavior than for a flat plate [31]. At the same time, the turbulence level and boundary layer thickness increase. The opposite is true for the convex side (Fig. 2.6), where the decreasing pressure leads to an acceleration of the flow and a reduction in turbulence level. It was further shown that the pressure gradients, caused by the bend, induce strong deviations from a logarithmic behavior on the convex wall. On the concave wall, a logarithmic behavior is only present for large radii of curvature [31]. Wall functions, introduced in Section 2.1, have therefore to be used with care and only to allow for a first flow field initialization.

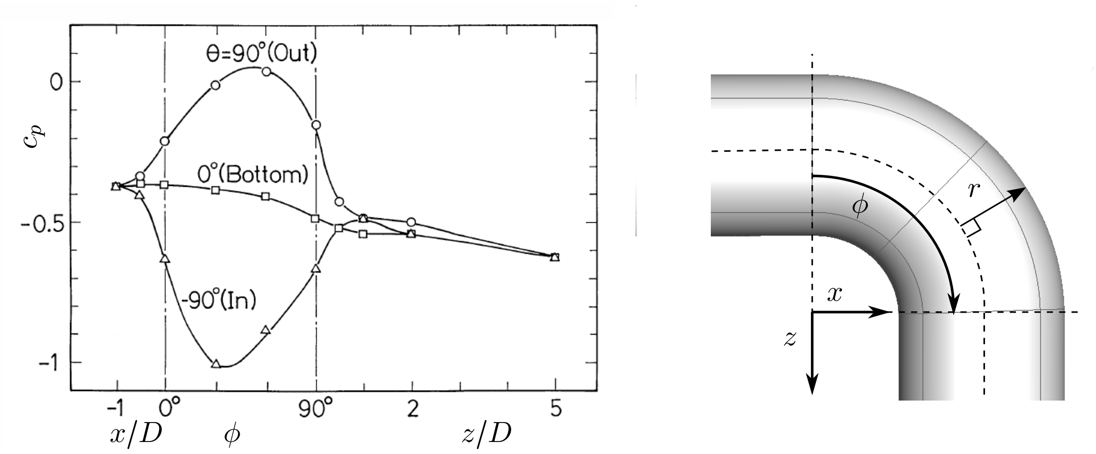

Figure 2.6: Streamwise distribution of wall static pressure along convex (In), concave (Out) and side (Bottom) walls of a 90° elbow duct with circular cross-section [7], starting from a distance equal to the duct diameter ($1\,D$) upstream of the bend until five diameters ($5\,D$) downstream of the bend.

The experimental results obtained by Sudo et al [7], shown in Fig. 2.7, show the acceleration of the flow around the convex side ($r/D = -0.5$), followed by a deceleration at the end of the bend. The opposite effect can be seen on the concave side ($r/D = 0.5$). Separation has been observed to occur at some point along the convex wall during numerous experimental studies [32–35].

In the case of laminar flow and moderate radii of curvature, laminar separation and reattachment of the flow can occur on the convex side, leading to a closed separation bubble. Figure 2.8 shows a time-averaged flow field that was obtained by PIV measurements and published by Ono et al. in 2011 [8]. During the experiment, conducted at a similar Reynolds number and sharpness factor as the curved exhaust duct, reattachment is found to occur at $z/D = 0.27$. Similar results were found by J. Gartner and M. Amitay in 2014 [35]. In shaft power turbines, separation can also occur around the hub.

An experimental study by Solodov et al. in 2013 [36] on gas turbine exhaust pipes confirmed that the main part of total pressure losses usually occurs near the pipe bend on the convex

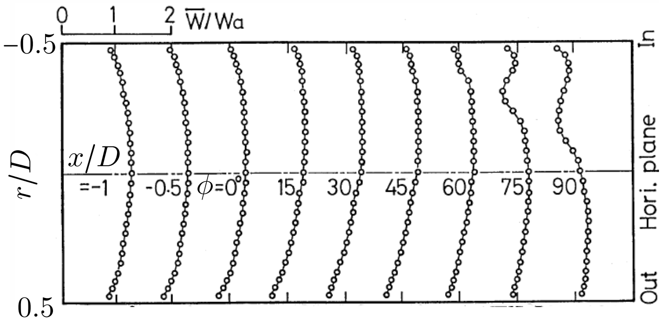

Figure 2.7: Distribution of time mean longitudinal velocity $\overline{W}$ at different sections along a circular 90° elbow duct [7]

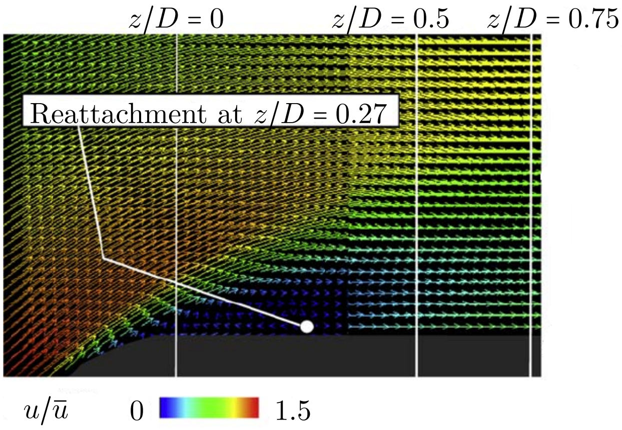

Figure 2.8: Time-averaged velocity field near the inside wall in an elbow duct obtained from PIV measurements showing flow separation and reattachment [8]

side of the exhaust system.

For the coupling of an exit guide vane geometry and a curved diffuser, one also has to take into account the interaction between the wake of the exit guide vane and the boundary layer in the bend. Low velocity turbulent flow from the wake, interacting with a boundary layer, can lead to earlier separation, whereas high velocity flows can re-energize the boundary layer and delay separation. An experimental study by Tulapurkara in 2001 [20] showed that the interaction of a wake with a boundary layer on both a convex or a concave wall is similar to the interaction on a straight wall. The wall's curvature promotes asymmetries in the wake, which compensate for the effects of the change in boundary layer thickness on the curved walls. An extensive experimental study by Majumdar et al. from 1998 [37] on the boundary layer flow in a 90° curved diffuser shows, what kind of boundary layer behavior is to be expected in the absence of an EGV wake.

In terms of inlet conditions, it was found during two studies (2010 by Roh et al. [38] and 2014 by Birk et al. [39]) that a small amount of inlet swirl can in certain cases help to avoid separation within the duct. However, the total thrust, in the case of aircraft applications, usually decreases when swirl is not removed. A study on a bent ejector with inlet swirl, by Maqsood et al. in 2006 [40], therefore found that an inlet swirl of 20° improves the aerodynamic efficiency of a curved diffuser, but reduces the kinetic energy of the exit flow. Furthermore, Fu et al. showed in 2008 [41], during a study on inflow conditions in turbine exhaust hoods, that an optimized radial distribution of the inlet total pressure can help to decrease negative effects caused by swirl, thereby increasing the overall aerodynamic performance. The introductions of jet flows and vortex generators within the curved geometry have also been found to increase the aerodynamic efficiency, by re-energizing the boundary layer and delaying separation. This was found by Sun et al. in 2006 [42], but is not the subject of this study.

The considerable amount of research on the topic provides a solid basis for the flow phenomena that can be expected during the analysis and serves as a means of validation for the numerical results. However, no detailed analysis has been published yet on the flow through a combined geometry of an EGV and a curved exhaust duct. Therefore, in order to validate the numerical results, the solver is used for an additional calculation of a flow through a 90° curved pipe with circular cross-section. This test case, without an exit guide vane or exhaust cone, is used for the validation of the solver for curved internal flows.

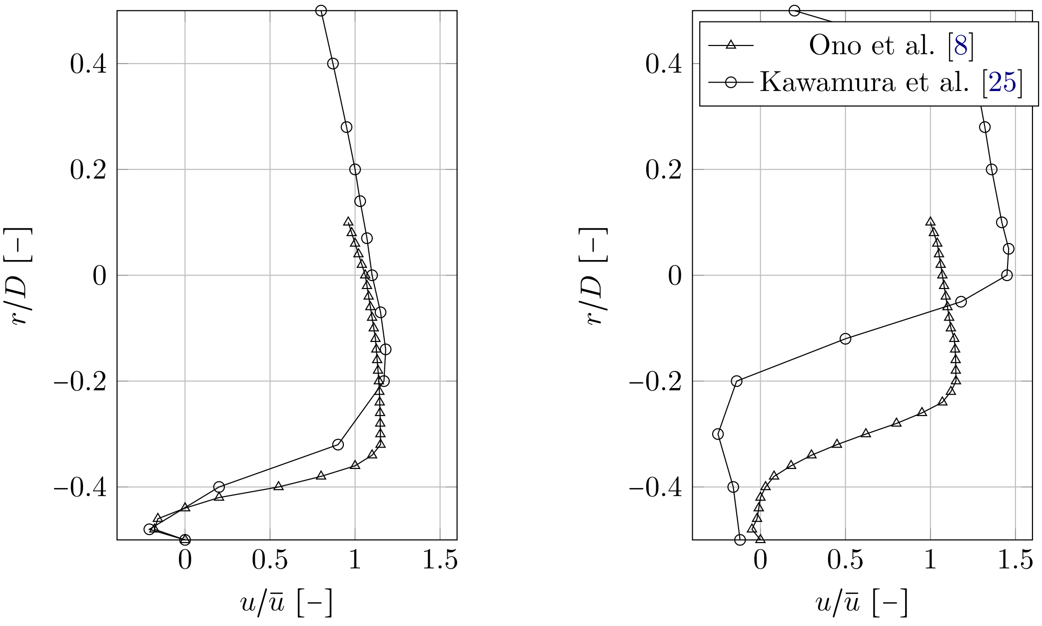

(a) At the end of the bend ($\phi = 90°$) **(b)** $0.25\,D$ downstream of the bend

Figure 2.9: Experimental results for velocity profile after elbow bend at different streamwise positions. Definitions of the aerodynamic interface planes (AIPs) used for the measurements are given in Fig. 3.25

The experimentally obtained results from Ono et al. in 2011 [8] and Kawamura et al. in 2002 [25] are taken at similar elbow geometries (R_c/D) within the post-critical Reynolds regime. They have been used for validation of numerous other experimental and numerical studies. Ono et al. and Kawamura et al. present streamwise velocity data at identical positions and therefore serve as a baseline during this research for validation of the numerical method employed for this research. Figure 2.9 shows the combined experimental results from the mentioned studies for the velocity profile after the bend and at a length of $0.25\,D$

downstream of the bend. Separation and reattachment can be observed at the convex wall, as visualized in Fig. 2.8. Differences for separation and reattachment are likely due to different inflow conditions. While Ono et al. [8] used a buffer tank with conical exit to obtain a flat inflow velocity profile, Kawamura et al. [25] employed a fully developed flow at the inlet. The latter causes a considerably thicker boundary layer, explaining the earlier and larger separation. With the previous experimental work on curved duct flows discussed, Section 2.3 gives a short overview over the method of sensitivity studies.

2.3 Sensitivity studies

In order to vary the geometry of the curved duct, to minimize pressure losses and to improve the flow through the exit guide vane, a sensitivity study is carried out.

While showing the effects of a number of design parameters on the objective function, a sensitivity study also gives an indication on the relative importance of the design variables and can allow to reduce the set of variables that is used during a later optimization procedure. At the same time, data from a sensitivity study can be used to create a database, which is a prerequisite for training surrogate-model based optimization routines. An example optimization using a Kriging based adaptive approach with eight geometry variables was carried out by Wang et al. in 2010 [43].

A carefully conducted sensitivity analysis is therefore essential both in understanding the link between design variables, flow phenomena and objective function value and in laying the groundwork for an efficient optimization procedure. Sensitivity analysis formed an essential part in recently developed optimization strategies, in some cases running simultaneously with the design optimization, as employed recently by Lee et al. in 2014 for 3D turbine blade design [44]. In 2012, Backhaus et al. used an initial sensitivity study for the training of a surrogate model and selection of a set of design parameters for the aerodynamic design of a counter rotating turbofan [45].

This review of previous work on the topics of EGV and curved duct flows and aerodynamic shape optimization has shown that, while a considerable amount of research has been conducted on the flow through curved ducts, no aerodynamic investigation of the mutual effects of an EGV and a curved exhaust duct has been done yet. Previous experimental studies on curved duct geometries are used for validation of the methodology. Together with a sensitivity the numerical analysis will provide insight into the aerodynamic phenomena and flow sensitivities to geometry changes in an EGV followed by a curved duct. This will help to design more efficient turbine outlet geometries in the future and serve as a guide to similar shape optimization problems.

Chapter 3

Methodology

The aim of this research, as stated in Chapter 1, is to investigate the aerodynamic flow phenomena occurring in an exit guide vane (EGV) followed by a curved duct by means of a RANS simulation.

First, the influence of the EGV wake on flow separation within the duct is analyzed. In a next step, secondary flows, as caused by the bend, (both upstream and downstream of the bend) are investigated. Finally, the effect of these secondary flows on the aerodynamic efficiency of the EGV is studied. The results are then quantified and a sensitivity study conducted to propose improvements on the initial geometry.

With the research problem stated and previous studies on the topics of curved channel flows and aerodynamic shape optimization discussed, this chapter sets out to present the tools and methods used to answer the research question. First, the research procedure is presented with a more detailed view on the research objective and sub-questions, before the following sections discuss the methods and procedures used.

The industry design tools used for generating a first geometry for the given flow conditions are presented and the preliminary design process explained. Section 3.3 then explains the 3D RANS calculation procedure for the aerodynamic analysis, by giving an overview over geometry generation and domain discretization, introducing the solver and presenting the methods used for post-processing. The methods and tools are then validated by computing a test case and comparing the numerical results to experimental data from the previous studies presented in Chapter 2. Finally, the procedure for the sensitivity study is discussed.

3.1 Research design

This section presents the research question and states the objectives that, when achieved, will provide an answer to the research question. The general research question is formulated and split up into sub-questions as follows. Answering the lower-level questions will provide a result for higher-level questions.

3.1.1 Research question

"Where do pressure losses in an exit guide vane of a low pressure turbine followed by a 90° curved duct mainly occur and how can they be minimized by means of a sensitivity study using a CFD analysis?"

1. What are the main flow phenomena occurring in an exit guide vane (EGV) followed by a 90° curved duct?
    - What main flow phenomena can be found in a 90° curved duct using a RANS analysis?
    - Do the numerical results match experimentally obtained data for similar elbow duct flows from literature?
    - How does a curved exhaust duct influence the flow through an exit guide vane?
    - What is the effect of an exit guide vane wake on boundary layer and separation in a flow through a bend?
    - What is the effect of a curved duct on residual swirl after the exit guide vane?
2. What relation can be found by means of a CFD analysis between zones of separated flow or flow asymmetry and pressure losses in an exit guide vane followed by a curved duct?
3. What is the effect of the following geometry changes on the pressure loss in an exit guide vane followed by a 90° curved duct?
    - What is the influence of the bend radius on the flow through the exit guide vane, on flow asymmetry and total pressure losses?
    - What is the influence of the plug shape on the flow through the exit guide vane and pressure losses in the curved duct?
    - What is the influence of the circumferential exit guide vane arrangement on pressure losses in the curved duct?
    - What is the influence of the residual swirl on flow homogeneity at the exit and on pressure losses in the curved duct?

3.1.2 Research objective

"The objective of this research is to investigate the aerodynamic flow phenomena occurring in an exit guide vane (EGV) of a low pressure turbine followed by a 90° curved duct by means of a RANS simulation. The influence of the EGV wake on boundary layer development within the duct and the influence of the curved exhaust duct on the flow symmetry at the EGV are to be investigated. A sensitivity study will show the influence of the bend radius and plug shape on the results and propose improvements on the initial geometry to minimize pressure losses."

The research objective leads to the following main steps and sub-goals.

- Geometry generation for a straight and curved exhaust duct with exhaust cone
- Design of an exit guide vane (EGV) to efficiently remove swirl (partly) from a specified inflow profile in a straight duct
- Generation of a structured multi-block mesh of the combined EGV and duct geometries (straight and curved) and calculation of the flow field using DLR's RANS solver TRACE at MTU
- Validation of the TRACE results for a 90° bent duct geometry without the EGV by comparison with experimental data from literature
- Calculation of flow field through the combined geometry of the EGV and the bent exhaust duct with a second RANS solver (SU2) for comparison
- Comparison of the flow solutions for the EGV with straight and curved duct. Investigation of the mutual influences of the EGV and the bend, such as asymmetric flow through the EGV and wake-boundary layer interaction, in the curved duct
- Performing a sensitivity study on the effect of the following geometry parameters: bend radius of curvature R_c/D, distance between the EGV and the bend l/D, plug geometry, circumferential EGV positioning and residual swirl. Main parameters of interest are the total pressure loss and the flow asymmetry at the EGV.

The aerodynamic investigation of this industry-relevant but complex flow problem will provide MTU Aero Engines with valuable insight and at the same time serve as a contribution and validation of the open-source SU2 suite.

The numerical study is split up into a qualitative analysis of the flow phenomena and a sensitivity study, including quantitative correlations between geometry changes, flow phenomena and pressure losses occurring in the duct. No direct physical experiments are conducted during this research due to the time and cost required for physical testing of the high temperature, high Mach and Reynolds number flow. The investigation is therefore purely numerical, employing two different Navier-Stokes solvers, TRACE and SU2. Both solvers provide the necessary functionality of different numerical schemes and turbulence models for the present flow regime. Due to the distance between the last stage and exit guide vane, unsteady wake effects are ignored and inflow conditions are assumed to be steady. In contrast to stator and rotor in a turbine stage, the domain for this problem involves no relative motion of consecutive rows. To limit computational cost, the flow is therefore assumed to be steady. Run times are further reduced by splitting up the domain into blocks for parallel calculations,.

In order to validate the solver for the geometry at hand, a test case consisting of a curved duct without exit guide vane is first computed with TRACE and the obtained flow field compared to experimental results from literature, as presented in Table 2.1. The same critical Reynolds number regime ($Re > 2\text{x}10^5$, Section 2.2), geometrical similarity (R_c/D) and $Ma < 0.3$ in the curved duct for both the TRACE calculation and the experimental results ensure dynamic similarity, as described in Section 2.2. The real geometry first consists of the exit guide vane and a core plug, followed by a straight exit duct, as shown in Fig. 1.3. The exit guide vane geometry for the CFD calculations is generated using meshing and geometry generation tools available at MTU Aero Engines, resulting in a multi-block .cgns file. TRACE calculations on the combined exit guide vane and exhaust geometry are then performed on the MTU computer cluster. In a next step, the straight exit duct is exchanged for a curved duct, using a parametrized geometry, allowing the modification of the radii of curvature and distance between the EGV and the bend more easily. The mesh of the combined EGV and duct geometry is generated both as a structured multi-block and as an unstructured single-block mesh, to allow for calculations with both TRACE and SU2.

3.1.3 Reference system

The combined geometry of the EGV and the curved duct is represented in 3D using a Cartesian coordinate system with the principal directions defined as shown in Fig. 3.1.

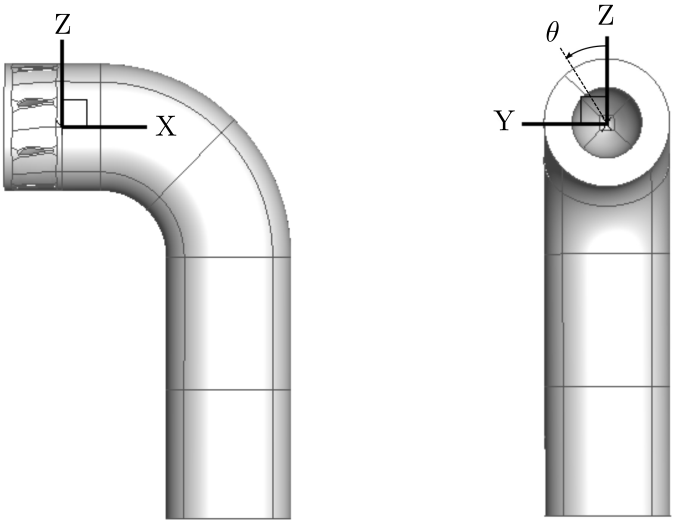

(a) Side view

(b) Front view

Figure 3.1: Definition of principle directions in the Cartesian coordinate system

The inlet flow is aligned with the positive x-axis and the outlet directs the flow into the negative z-direction. The y-axis follows from the right-hand rule. TRACE, however, is based on a cylindrical coordinate system, with the inlet in positive z-direction, the r-direction pointing from the duct center towards the outer walls and θ pointing in circumferential direction of the duct. The use of cylindrical coordinates facilitates the implementation of typical turbomachinery boundary conditions, such as circumferential averaging, radial distributions for inlet conditions and the definition of swirl. The transformation from Cartesian to cylindrical coordinates is done internally and the results are directly transformed back into Cartesian coordinates during post-processing. SU2, not specifically designed for turbomachinery applications, is based on Cartesian coordinates. Some extra definitions are therefore introduced, in order to specify turbomachinery design and flow parameters. The angle θ is used to define the circumferential EGV positioning θ_{EGV}, as mentioned in Section 3.1.6. The swirl α, at the EGV inlet and exit, is defined as in Fig. 3.2. Finally, ϕ is used to define the streamwise position of a cross-sectional cut through the bend (Fig. 3.3).

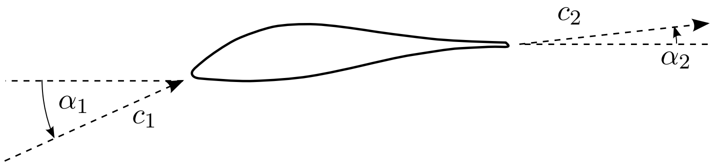

Figure 3.2: Definition of swirl α, view from casing towards hub

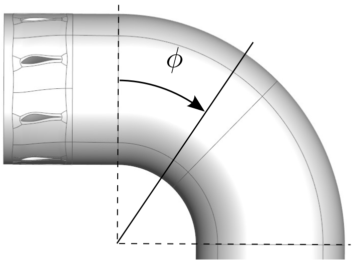

Figure 3.3: Definition of ϕ, indicating location of cross-section through the bend

3.1.4 Assumptions

Due to limited computational resources the complexity of the problem is limited by a number of assumptions. This section gives an overview over the assumptions made during this research and the effects that the individual assumptions are expected to have on the results.

- **Steady inflow conditions**
  Minor unsteady effects from the low pressure turbine wake are not taken into account, due to the distance between the last LPT stage and the EGV. Small unsteady effects from the LPT in reality might lead to earlier flow separation in the EGV.

- **Steady flow through the duct**
  The flow in the EGV and exhaust geometry is assumed to be steady. Oscillatory behavior in the EGV wakes or separation and reattachment at the plug and duct walls moving forwards and backwards can, however, lead to differences in the numerical results.

- **Negligible compressibility effects in the exhaust duct**
  Due to the Mach number remaining below $Ma = 0.3$ after the exhaust plug, compressibility effects are assumed to be negligible in the duct. The calculations performed on the test case of a curved duct can therefore be compared with experimental studies based on incompressible flows (Section 2.2).

- **Smooth duct walls**
  Rough walls in reality could lead to an increased boundary layer growth and higher

pressure losses.

- **Turbulence modelling error negligible**
  It is assumed that the RANS turbulene modelling correctly models the effects of turbulence. In reality, however, as stated in Chapter 2, turbulence models often have problems determining the right amount of turbulence generated on curved duct walls and could lead to slightly wrong results at the curved exhaust walls. The modeling error is addressed during comparison of the two different RANS solvers.

- **Ideal gas**
  The fluid is assumed to behave as an ideal, single-phase gas. In a real exhaust flow, unburned particles, inhomogeneous mixing etc. could lead to locally different flow properties.

- **Spatial and temporal discretization**
  It is assumed that sufficiently small element lengths and time steps are chosen for discretization of the problem, to resolve all important flow phenomena. Not sufficiently resolving major flow structures would lead to an erroneous solution.

3.1.5 Boundary conditions

As laid out in Chapter 1, the inlet conditions, mass flow, EGV shape and inner and outer diameters are fixed. The geometry is shown in Fig. 1.3 with inner and outer diameters R_i and R_o. The total inflow conditions for this research are fixed and taken from reference flow profiles at the low pressure turbine outlet. A non reflecting boundary formulation is used to enforce the boundary values with minimum numerical reflections during the RANS calculation.

In order to completely define the problem, however, additional information at the outlet has to be provided. For this research, the overall pressure losses and flow phenomena for an engine of a certain performance and thrust are of interest. The required mass flow is therefore set, as stated in Table 3.1, and the corresponding outlet pressure found iteratively.

Fixed parameter	value	units	Description
$\dot{m}$	fixed	$[kg/s]$	mass flow
$u'/\bar{u}$	0.04	[-]	turbulence intensity at inlet
l	1.23x10^{-4}	$[m]$	turbulence length scale at inlet
$\frac{p_{t_{inl}}}{\bar{p_t}}$	distribution in Fig. 3.4a	[-]	inlet total pressure
$\frac{T_{t_{inl}}}{\bar{T_t}}$	distribution in Fig. 3.4b	[-]	inlet total temperature
α_1	distribution in Fig. 3.4c	[°]	inlet swirl

Table 3.1: Boundary conditions for closed problem formulation

Turbulence intensity and length scale are set at 0.04 and 1.23x10^{-4} m, respectively. For the total pressure, temperature and swirl at the inflow boundary, a non homogeneous distribution is chosen to obtain a typical pressure, temperature and velocity profile. The distributions are presented in Fig. 3.4.

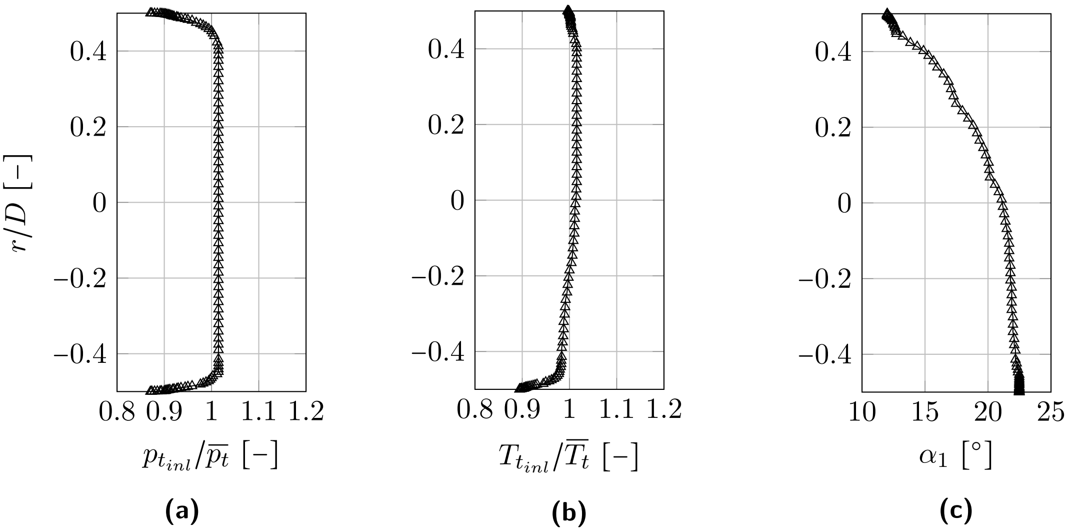

Figure 3.4: Inlet boundary conditions for total pressure p_t, temperature T_t and swirl α. Temperature and pressure are non-dimensionalized for reasons of confidentiality.

Both SU2 and TRACE use the same set of boundary conditions on mass flow, inlet flow profile and swirl distribution. Only for the turbulence quantities, SU2 and TRACE use a different convention. While TRACE uses the turbulent intensity and length scale to compute k and ω, SU2 uses the turbulent intensity, together with the turbulent viscosity ratio μ_t/μ, as input. The two input variables of turbulent viscosity ratio and length scale are, however, related and are set to yield the same inlet turbulence characteristics.

3.1.6 In- and Output parameters

As laid out in Chapter 1, the boundary conditions, EGV shape and diameter of the duct are

Table 3.2: Independent geometric design variables leading to a parametric geometry of the exhaust system

Design variable	units	Description
R_c/D	[−]	Ratio of bend radius and duct diameter
l/D	[−]	Ratio of distance between the EGV exit plane and the start of bend and duct diameter
θ_{EGV}	[°]	Circumferential positioning of exit guide vanes (clockwise deviation from symmetrical arrangement, $\theta = 0°$ for symmetry with $y = 0$)
α_2	[°]	Swirl angle at the EGV exit, controlled by the EGV shape and flow deflection
plug shape	[−]	-

fixed. This section gives a short overview over the independent design variables (Input) to be varied in order to minimize pressure losses, as well as the parameters used to quantify the exhaust system's performance (Output). Table 3.2 states the independent geometric design parameters that are implemented in the parametric geometry.

3.1.7 Research procedure

The exit guide vane geometry consists of the annulus and a number of vanes. Using both 2D and quasi 3D methods, as described in Section 3.2, an initial airfoil shape for the vanes is designed from stacked 2D sections. The flow field in the EGV is then calculated with TRACE, using only one passage of airfoils with periodic boundary conditions, to analyze and optimize the 3D flow field. The final EGV is then analyzed in TRACE, using full 360° calculations with both straight and curved duct, to find the main flow phenomena in the combined geometry.

The same calculations are finally performed in the open-source suite SU2 and the results between both solvers compared. The suitability of SU2 to handle the geometry and boundary conditions, as well as the extra work needed to implement eventually missing routines or boundary conditions, represent a limitation for the use of SU2 during this research. Where SU2 requires more time than available, obtaining a validated solution with TRACE is the main objective and priority.

In a next step, a sensitivity study is performed based on a limited number of geometry parameters, using TRACE. The geometric design parameters presented in Table 3.2 are varied during this study to investigate their effect on the flow loss phenomena. The research procedure is schematically shown in Fig. 3.5.

3.2 2D and quasi-3D methods

Physical testing of turbine exhaust system performance is complex and expensive, due to the mutual aerodynamic influences of low pressure turbine, exit guide vane and the exit duct [36]. Turbomachinery test rigs are expensive to set up and to operate and measuring the required data is not trivial. Industry is therefore focusing increasingly on numerical simulation as a design method.

In general, turbomachinery problems are difficult to solve numerically, due to large domains of several blade rows, involving transition and separation of compressible, unsteady flows. Even with the assumptions made in a Reynolds-averaged Navier-Stokes (RANS) solver, a single turbomachinery calculation often takes hours or days, making geometry optimization an expensive task.

Especially in preliminary design, where a large number of geometries need to be generated and analyzed, simpler methods are often employed. While 1D, 2D and quasi-3D methods only give a crude assumption of the real 3D flow field, they can show qualitative trends and allow for a wide range of optimization strategies.

1D methods are often used on system level to determine the thermodynamic variables at different axial positions, to achieve a desired system performance. When tuned and validated

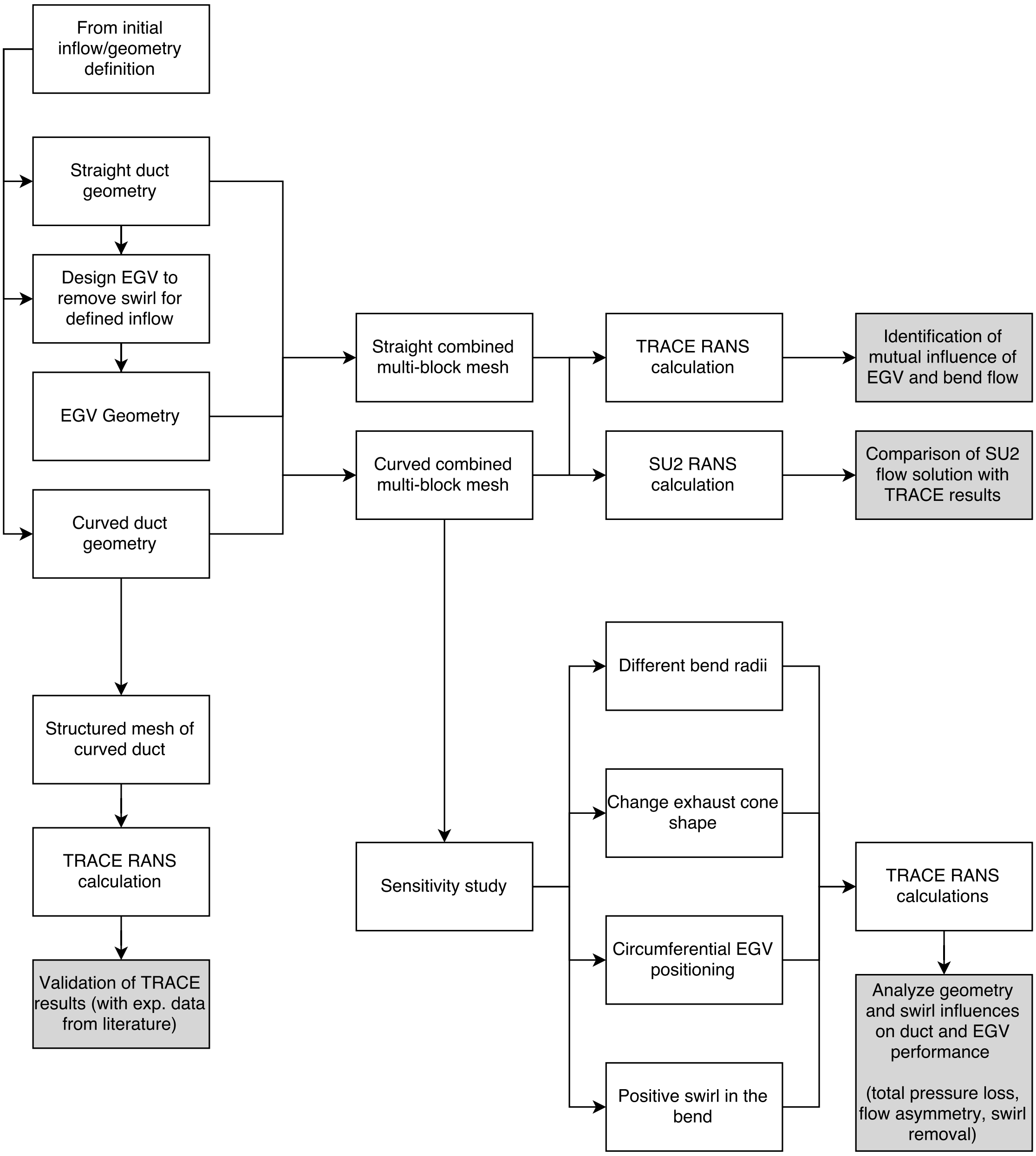

Figure 3.5: Schematic procedure for the aerodynamic investigation of an EGV followed by a curved duct

correctly, 2D and quasi-3D methods can yield good approximations for flow angles and pressure distributions on high aspect ratio blades. The definitions of the individual surfaces used in a turbomachinery stage are given in Fig. 3.6.

The following gives a short overview on methods used in industry for the generation of annulus and blade geometry during the preliminary design phase. These methods also apply for an exit guide vane geometry and are used during the generation and analysis of the exit guide vane and curved duct geometry under consideration. Knowledge of the reader on thermodynamic cycles and performance calculation in gas turbines is assumed. For detailed information on the subject the author refers to [46].

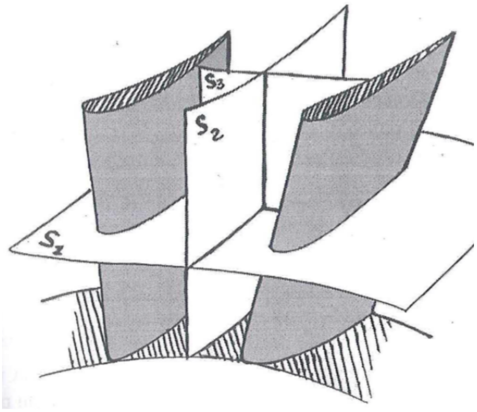

Figure 3.6: 2D cut definitions in a blade row

3.2.1 Quasi-3D streamline curvature analysis

To optimize the annulus geometry and determine the flow angles, a method called streamline curvature analysis is often used in industry. This method uses a Lagrangian formulation for the force equilibrium of a particle on a S_2 surface (Fig. 3.6) positioned exactly between two consecutive blades. The resulting differential equation for the pressure along a quasi-orthogonal direction is solved iteratively to update the S_1 and S_2 surfaces. The streamline position is then found as the cut between S_1 and S_2 surfaces (Fig. 3.6). Run times are in the order of seconds and allow for efficient optimization of the annulus geometry and flow angles. An example for the resulting streamline positions in an exit guide vane geometry with straight plug and exhaust duct, as generated for this study, is shown in Fig. 3.7.

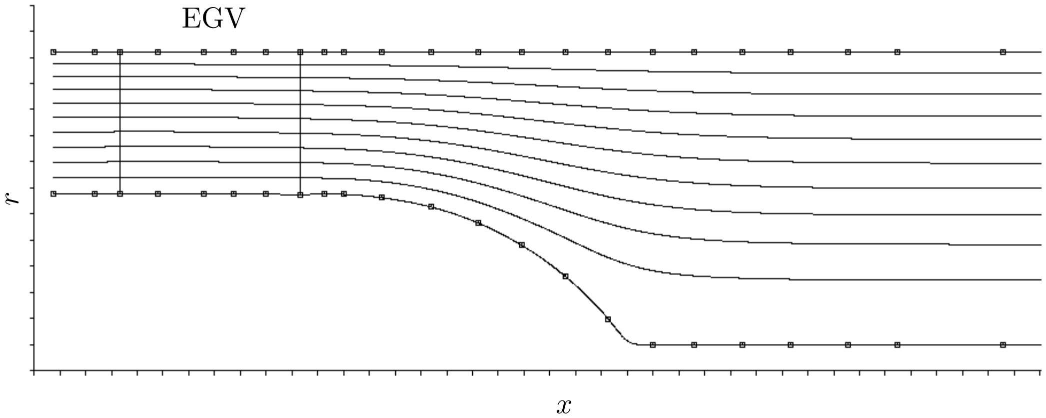

Figure 3.7: Quasi-3D streamline solution for an EGV geometry with straight plug and exhaust duct, using streamline curvature analysis

The flow angles are known along the streamlines and can be used for the blade design, while the thermodynamic variables along the streamlines allow for a flow field initialization during the later RANS calculations. The streamline curvature method therefore provides valuable flow field and design information during the preliminary design phase of the EGV and straight duct geometry. The method, however, relies on axis-symmetric geometries and is therefore only used for the preliminary design of the exit guide vane section.

3.2.2 2D Euler analysis

The exit guide vane is first designed at its midsection in 2D. Besides the required flow deflection angles from the streamline curvature analysis, basic geometric requirements for manufacturing, cooling and structural integrity are taken into account. The influence of 3D flow phenomena such as cross-flow, passage vortices, unsteady wake effects and others are assumed to be negligible at this point, so that a 2D analysis on the mid-span S_1 surface (Fig. 3.6) can be used as a first estimate. Experience shows that for large aspect ratio blades this usually leads to reasonably accurate results, while the use of the 2D Euler equations allows to calculate the flow field within seconds. This makes a first optimization of the pressure distribution (Fig. 3.8) a time efficient process. Performed for multiple blade sections and stacked to a 3D geometry, this gives a good first estimate of the EGV geometry, saving computational time and cost.

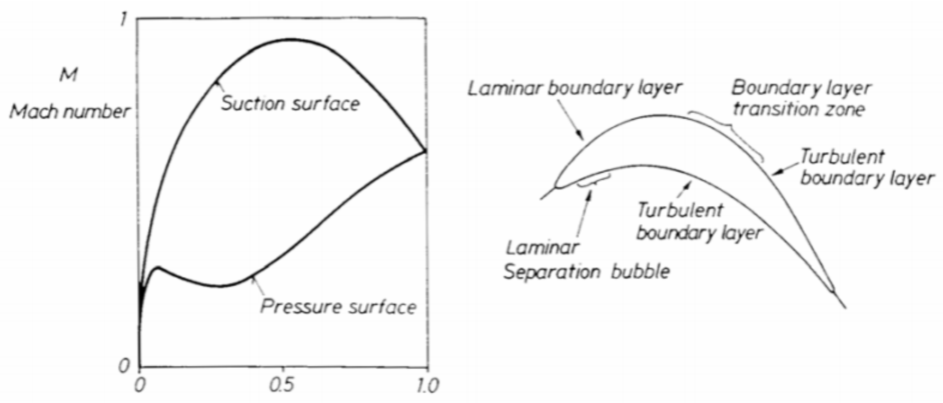

Figure 3.8: Example Mach/pressure distribution and definition of zones for a turbine blade [9]

3.3 3D Modeling and RANS calculation

In the process of numerical simulation, efficient geometry discretization and mesh generation are crucial for saving computational time and providing accurate results. Together with the definition of boundary conditions, this step is referred to as preprocessing and is presented in more detail in Section 3.3.1 for the geometry at hand. Once the mesh is generated and boundary conditions applied, the equations describing the problem are solved on the discretized domain. This step, called processing, is executed by the solver (Section 3.3.2). Once a satisfactory solution is obtained, the results are evaluated and post-processed (Section 3.3.3), where flow parameters are found from the computed solution and visualized for interpretation. The following sections give an overview over the techniques and terminology used, present the equations describing the problem and introduce the two solvers used, TRACE and SU2.

3.3.1 Preprocessing

In order to calculate the flow field using the solvers TRACE and SU2, the EGV and duct geometry is discretized into a finite number of simple geometries and nodes. The resulting finite set of nodes allows to evaluate the discretized governing equations at each node, resulting in a matrix equation to be solved by the solver.
As geometry generation and the building of an efficient multi-block mesh form an essential part of this study, this section gives an overview over the mesh strategies employed to discretize the problem domain. Finally, the chosen structure and topology of the EGV and curved duct mesh are presented.

Structured meshes

Different strategies exist to discretize a geometry and define node and element positions. In structured meshes, the position of every node and neighboring nodes is defined by its position in the computer's memory. This leads to regular sparse matrices, saving both memory and computational effort [12]. Structured meshes are therefore not defined by element type, but by how the data is stored. While a structured mesh usually consists of hexagonal elements, hex-elements can also be used to construct unstructured meshes. Structured meshes can be time-consuming to generate on complex geometries and mesh adaptation is limited to nodal redistribution methods [47]. Hex-elements provide mostly parallel faces and right angles, minimizing mesh-locking of highly skewed cells during elasto-plastic structural analyses and errors from interpolating fluxes on cell faces [12].

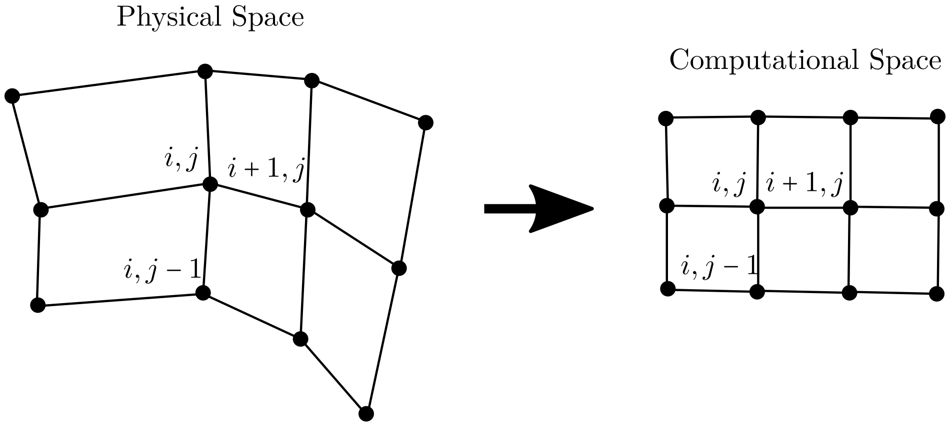

Figure 3.9: Structured mesh in curvilinear and uniform cartesion representation [10]

Figure 3.9 shows a 2D structured mesh. On the left side, the mesh is shown in physical space, a curvilinear mesh obtained by discretizing the geometry. A structured mesh is easily represented as a uniform Cartesian grid, used for solving the governing equations, by storing the nodes in a 2D array, where the connectivity is implicitly defined by the memory structure. The conversion is performed using a mapping function.

Fully structured meshes are bound by the 2D array representation to be defined by four edges, with each two opposing edges having the same node count. By connecting boundaries, those curvilinear meshes come in three basic forms: H-grids (Fig. 3.9, O-grids and C-grids. To form an O-grid, an H-grid is curved, so that two opposing edges (boundaries) are connected (Fig. 3.10), forming a set of concentric circles and creating a periodic boundary condition in computational space.

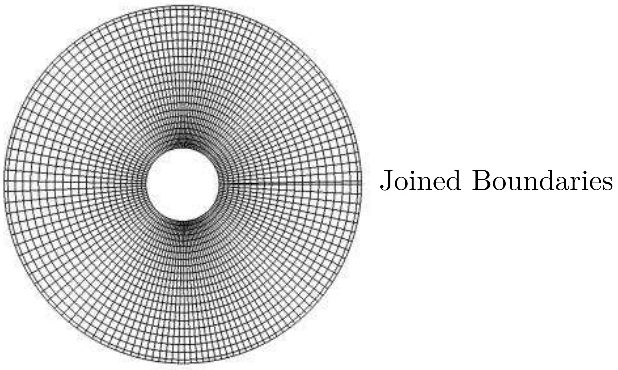

Figure 3.10: O-Grid (structured) [11]

A C-grid is typically created around an airfoil, by folding a H-grid as shown in Fig. 3.11 backwards around the airfoil, with one boundary forming the airfoil surface and being connected to itself from the trailing edge onwards. A H-grid is every structured grid that is not an O-grid or a C-grid.

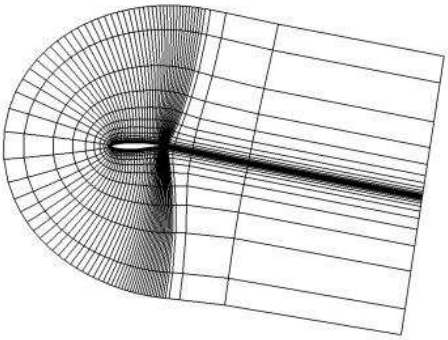

Figure 3.11: C-Grid around an airfoil (structured) [11]

Multi-block meshes

For complex geometries, such as the EGV and duct geometry, discretization as a single H, O or C-grid would lead to largely distorted cells of low element quality. Structured meshes for complex geometries are therefore usually split up into multiple blocks [12]. The method of multi-block meshes is best introduced using 2D meshes. The same principles are used in 3D by extrusion of 2D meshes, as shown in Fig. 3.12. When creating a 2D structured mesh, one block initially consists of four defined edges, where each two opposing edges have the same amount of nodes, in order to allow for a structured block of rectangular elements. On complex geometries, such as the EGV with curved duct, this leads to large mesh distortions with areas of very long and non-ideal cell shapes. In order to overcome these problems, singularities are introduced, dividing the domain effectively in multiple blocks [12]. Figure 3.12 shows, how introducing four singularities (indicated as the intersections of thick lines) divides the domain into eight blocks, connected along shared block boundaries, called 'abutting boundaries'. Such boundaries can be point-matched (i.e. all boundary points coincide) as in the example, which, if possible, is preferable to non-point-matched boundaries.

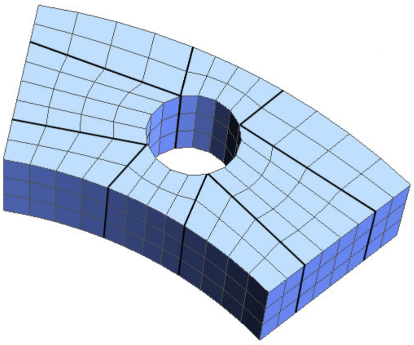

Figure 3.12: Multi-block structure for improved element quality [12]

In the example in Fig. 3.12, the multi-block structure allows to have a larger number of nodes on the outer than on the inner, circular boundary, leading to a more uniform mesh. Within each block, opposing edges will still have the same node count, but an effective division of the domain into blocks allows to generate the desired element size and shape individually at every location. In two dimensions, interior singularities are defined as points where more or less than four elements meet. In 3D, these singularities become singularity lines. When nodes on block edges don't coincide, non-matching boundaries result, where values on neighboring block nodes are interpolated from boundary nodes of the first block. Overlapping boundaries are generated when boundary points of one block are directly connected to interior boundaries of a neighboring block. Point-matched overlapping boundaries are often used to let blocks interact, but are generally difficult to achieve on complex geometries.

Generating structured multi-block meshes by the introduction of singularities is a time consuming process. Therefore, for many engineering applications where similar shapes are meshed repeatedly, templates are generated that define a certain block structure [48]. In the field of turbomachinery, structured meshes are usually desired to resolve the flow more efficiently. The complex geometry of a turbine passage requires a complex multi-block structure to obtain the desired resolution and alignment in every region. Templates are therefore usually used. An example of a structured multi-block mesh for a turbine passage is shown in Fig. 3.13. Recently developed automated block generation techniques often rely on medial-axis theory to align unstructured meshes with the anisotropic flow pattern [47].

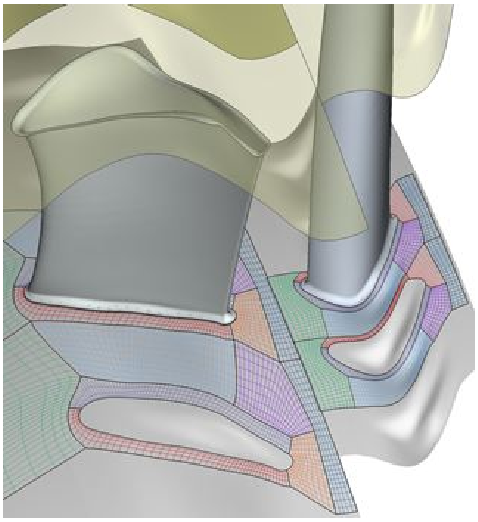

Figure 3.13: Multi-block grid of a turbine stage [13]

Unstructured meshes

Unstructured meshes do not use direct mapping between the location of nodes in real space and in memory. Nodes stored at neighboring positions in memory might have no physical relation [12]. This leads to sparse, but irregular matrices and requires extra computational steps, using transformation matrices to locate neighboring cells, which in turn increases computational time and cost [12]. On the other hand, unstructured meshes are more flexible in the choice of elements. While structured grids are bound to use quadrilaterals in 2D and hexagons in 3D, unstructured grids can use different cell shapes.

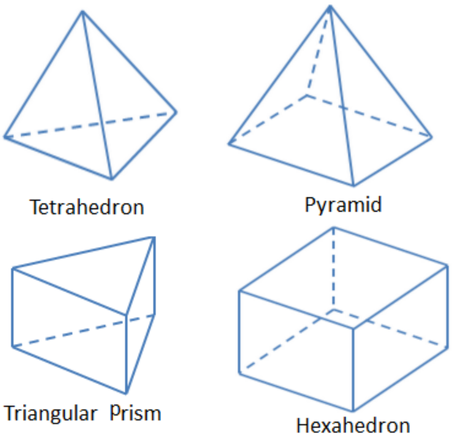

Figure 3.14: Common element types used in unstructured 3D meshes

Figure 3.14 shows a tetrahedral (top left) and a hexagonal element (bottom right), connecting four and eight nodes, respectively. When constructing hybrid meshes, pyramid cells are often used. Prisms are usually employed when a triangular (unstructured) 2D surface mesh is used to create a boundary layer. Extruding the triangular cells to prisms, instead of generating tetrahedral cells, avoids high skewness of tetrahedral cells within the boundary layer. Hex cells, due to their mostly parallel faces and right angles, however, are still considered superior in terms of accuracy, even when used in unstructured meshes [12]. Hybrid meshes often make use of the superior element properties of hexagonal elements in areas of highly anisotropic behavior.

While the use of tetrahedrons is common in most unstructured solvers, many solvers also allow prisms, hexagons or even n-sided polygons. The generation of unstructured grids is therefore much less time consuming and often automated. By splitting cells, the mesh can be refined locally and different mesh adaption techniques are available during mesh generation and at run time [47]. Accuracy and convergence rate is usually less for unstructured tetrahedral meshes, as small angles of skewed cells can lead to cell locking [12] and wrongly interpolated fluxes. Especially in resolved boundary layers, where the height of cells decreases rapidly, this can lead to high skewness or a large amount of cells. Advantages of structured meshes therefore include:

- Banded sparse matrices for fully structured grids, leading to a decrease in required memory and computational time
- Eminently suitable for multi-grid acceleration methods
- Highly efficient for resolving anisotropic features, when appropriately oriented [12]

Hexagonal elements, usually associated with structured grids, but also used for unstructured meshes, are often preferred where possible, due to the following advantages:

- Less susceptible to mesh locking for large-deformation structural analyses
- Smaller discretization errors, as reported in CFD analyses [12]
- Larger time steps feasible due to superior element shape quality (less skewed) [12]
- Anisotropic stretching

The largest disadvantage of structured meshes however, is the time-consuming generation and their missing flexibility for local modifications. Using the advantages of both structured and unstructured regions on complex geometries leads to hybrid meshes, where tetrahedral elements are used in geometrically complex areas.

Hybrid meshes

In commercial meshing software, such as Pointwise [10], hybrid meshes are regularly used to employ hexagonal cells in boundary layers (where possible) by extrusion, before the mesh is grown from the boundary layer, using tetrahedral cells.

Defining outer boundary spacing, growth rate, maximum element size or individual spacing for different areas, allows to control the growth of the tetrahedral mesh and to generate hybrid meshes that make efficient use of the different geometry features and flow regimes. Collision detection techniques are employed to allow implementation of these techniques on almost every geometry.

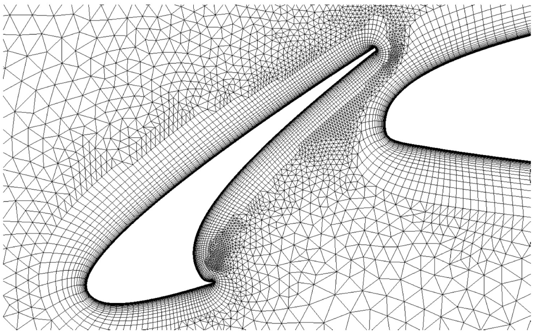

Figure 3.15: Hybrid mesh on a leading edge flap [14]

Cell size

In order to resolve all important flow phenomena, while keeping the total cell count and computational cost at a minimum, an efficient mesh should be refined locally at points where high gradients exist, such as boundary layers, flow separation and shocks. For a fully matching multi-grid mesh, this requires the right topology and node spacing within the blocks. The earlier introduced wall length unit y^+ (Equ. 2.2) provides a good measurement for the height of the first cell needed to resolve the boundary layer. In order to resolve the boundary layer, $y^+ \sim 1$ is desirable. To minimize the cell count and computation time, wall-functions are used during the analysis as an approximation of the boundary layer velocity profile. Calculations based on wall-functions have a less strict requirement on the first cell size, which should only lie within the boundary layer at approximately $y^+ < 30$. Wall functions are also frequently used to provide an initial flow field, which can be used to determine the value of y^+. This allows for a so-called y^+ adaption by refining the mesh for a low Reynolds number calculation. However, as mentioned in Section 2.2, care should be taken when using wall functions with curved duct geometries.

As flow phenomena, such as shocks and flow separation, are usually not known a priori, initial calculations are required to determine the locations where mesh refinement is needed. While unstructured meshes allow for mesh refinement and adaption techniques during run time, this is usually not the case for structured meshes. The one-to-one relationship between cells in physical and computational space usually requires re-meshing of the whole geometry to refine the mesh locally.

Symmetry and Periodicity

The last step during preprocessing is defining symmetry and other boundary conditions that constrain the problem sufficiently to solve it. Standard boundary conditions in turbomachinery problems include inlet and outlet-conditions, both of which have to be defined for subsonic flows.

When node counts become very large due to a wide range of relevant scales, as is often the case for turbomachinery problems, computational effort can increase beyond feasible time and cost. To deal with large, but mainly axis-symmetrical flow problems, the concept of mixing planes has been developed. The method divides multi-stage problems into individual domains with coupled boundary conditions that can be solved efficiently in a parallel manner on multiple processors [13]. Figure 3.13 shows an example of a multi-block mesh for a turbine stage. This mesh can be coupled to the individual meshes of preceding or following stages through mixing planes. At a mixing plane, the total flow properties are averaged circumferentially to obtain the inlet and exit conditions for the following or previous stage. This allows to greatly reduce calculation time by splitting up the problem into manageable domains. Circumferentially inhomogeneous and unsteady wake effects can not pass a mixing plane and have therefore to be modeled by other means, if their effect is considered important [49].

Calculation cost is further decreased by using periodic boundary conditions. Usually the domain has to span only two blades of every row (one passage), assuming axial flow symmetry. For a curved duct, however, this is not possible, as the geometry and the flow field are not axis-symmetric anymore, but affected by the downstream bend. A 360° simulation is therefore carried out, modeling the complete geometry of the EGV and the curved duct. This requires a considerably higher number of mesh points or a coarser mesh, compared to an axis-symmetric flow where only one passage is meshed.

Exit guide vane topology

The geometry of the problem under consideration is split up into two domains for the mesh generation. The exit guide vane is first modeled separately and then connected to the exhaust duct. To analyze the effects of the 90° bend, both a straight and a 90° curved duct are modeled and connected to the EGV. The EGV geometry consists of an axis-symmetric blade passage defined by inner and outer diameter. The industry standard for blade passages in turbomachinery is to use fully structured multi-block grids, relying on predefined templates. The resulting mesh for a single exit guide vane passage is shown in Fig. 3.16, consisting of different H-grids to discretize the passage geometry. It can be seen how the cells are aligned with the general flow direction and more cells are used in areas where small scale flow phenomena are expected. Due to the axis-symmetry of the turbomachinery component, only one passage is modeled and later rotated to achieve the complete 360° mesh.

Curved duct topology

The exhaust duct geometry consists of a curved duct with a plug extruding from the EGV section into the exhaust duct. For the curved duct mesh generation, numerous approaches can be found from literature on channel flows using both structured and unstructured meshes, as shown in Fig. 3.17 and 3.18. Considering the advantages of a fully structured mesh however, as described before, this report focuses on the generation of a structured multi-block topology

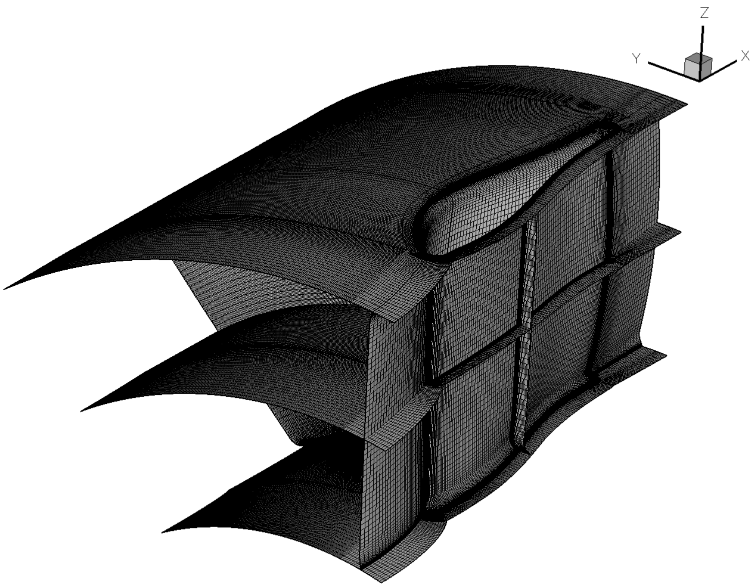

Figure 3.16: Structured multi-block mesh of single EGV passage

for both the EGV and the curved duct sections. The most commonly used topology for structured internal flow meshes is a H-grid positioned at the center of the duct, followed by an O-grid, using a point-matched boundary and decreasing O-grid cell size to resolve the channel boundary layer. Transition between O- and H-grid can be both sudden or smooth (Fig. 3.17b and 3.17c, respectively). Other approaches use a hybrid mesh consisting of a structured O-grid for the boundary layer and an unstructured tetrahedral mesh for the core flow (Fig. 3.18).

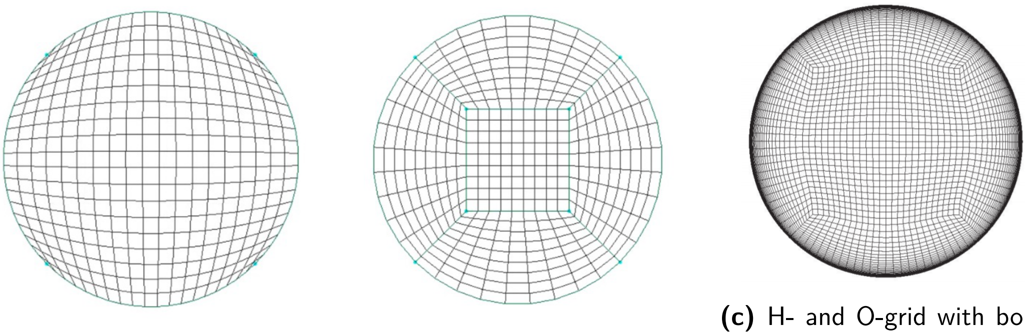

(a) Single H-grid [10] **(b)** H- and O-grid [10] **(c)** H- and O-grid with boundary layer cells [50]

Figure 3.17: Fully structured duct meshes

Besides discretizing the duct flow downstream of the plug, the topology needs to capture the change from an annual cross-section, bounded by inner and outer radius, to a circular cross-section. Many approaches found from literature use a hybrid topology, generating hexagonal boundary layers by extrusion of quadrilateral surface meshes and connecting the meshes with unstructured tetrahedral blocks. More time consuming, but computationally more efficient, is the introduction of singularities near the end of the plug to create a fully structured multi-block topology.

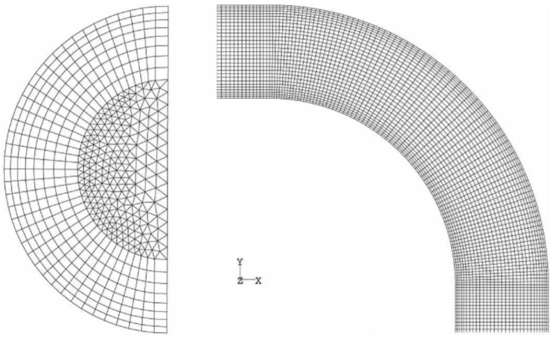

Figure 3.18: Hybrid mesh consisting of O-grid and tetrahedral cells [15]

For the EGV and curved duct geometry, this is done by projecting a H-grid on the end of the plug, followed by an extruded O-grid that continues upstream along the cylindrical plug shape. Singularity lines emanating from the H-grid at the end of the plug define the 3D block boundaries. A fine resolution of the H-grid allows to resolve the flow in the wake of the plug.

Final geometry

The geometry is realized with the topology described in the previous sections, using Numeca's mesh generator modules Autogrid and IGG. In a first step, the wire-frame of the single passage EGV geometry based on stacked 2D profiles (Section 3.2.2) is used to mesh the EGV blade passage in Autogrid. The single passage mesh is repeated and rotated to obtain the full 360° EGV geometry with eight blades as shown in Fig. 3.19. This mesh is then loaded in IGG, where the second half of the geometry, consisting of plug and curved duct, is modeled, meshed and connected to the EGV geometry to form one single 360° structured multi-block mesh.

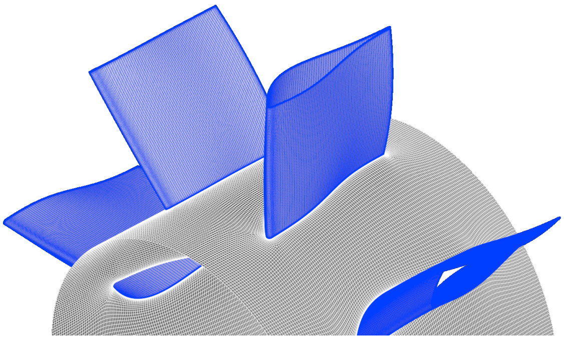

Figure 3.19: 360° EGV geometry with eight vanes modeled in Autogrid

Individual blocks are connected along fully matching boundaries and singularity lines. As presented before, structured multi-block grids allow for superior convergence rates and accuracy. The geometry is therefore sub-divided into a number of smaller blocks, as presented in Fig. 3.20a and 3.21a. The multi-block structure allows to tailor the local mesh size individually for different regions to resolve important flow phenomena while providing high quality hexagonal cells throughout the domain.

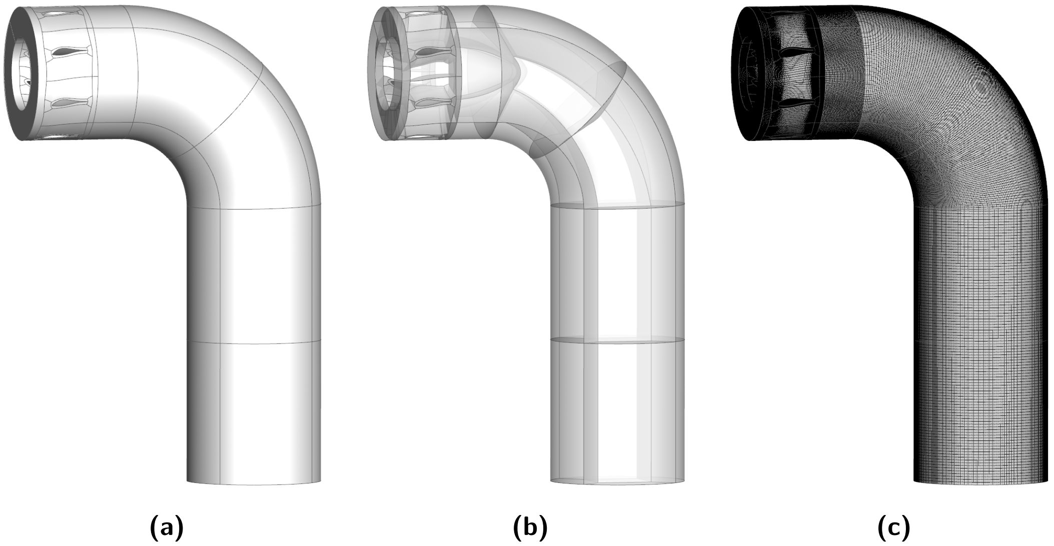

Figure 3.20: Final geometry and multi-block mesh topology

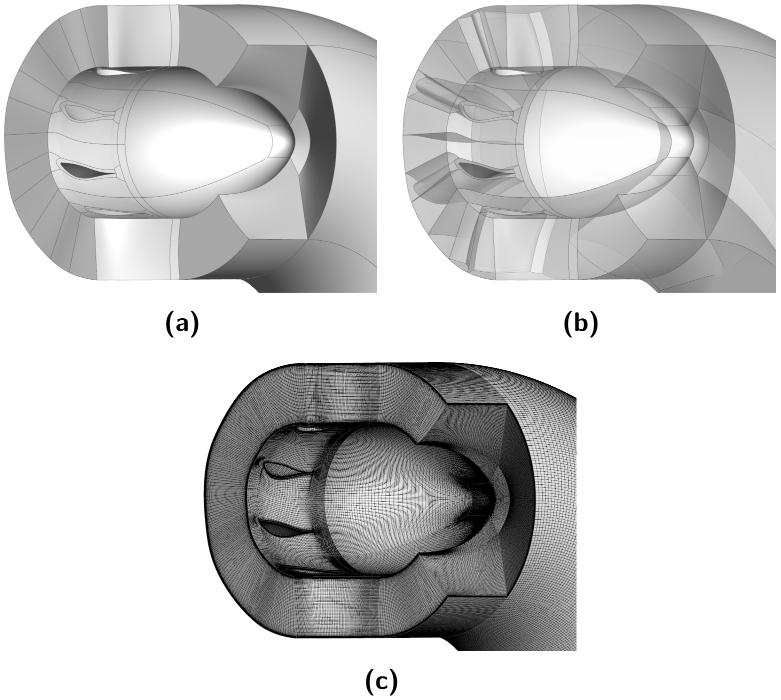

Figure 3.21: Mesh topology at the EGV spinner and the plug

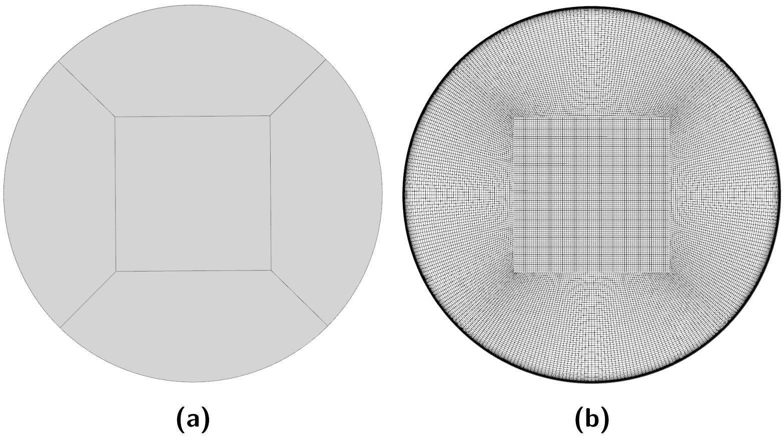
(a) (b)

Figure 3.22: Mesh topology at the Outlet face

Interfaces between blocks are based on fully-matching connections (Fig. 3.20b and 3.21b) defined in Automesh IGG. The final volume mesh is shown in Figures 3.20c and 3.21c. The mesh topology chosen for the curved duct and transition from the radial exit guide vane section over the spinner is shown in Fig. 3.22 and 3.21, respectively. In order to resolve the boundary layer for low-Reynolds computations, a first-cell height of $10^{-5}\,m$ is chosen to achieve y$^+$ values of $y^+ \sim 1$ on all solid boundaries.

During the analysis, the base geometry is varied by varying the radius of the bend, the plug shape and the circumferential positioning of the exit guide vanes. The general mesh topology, however, is kept the same throughout the parameter study.

3.3.2 RANS calculation

The compressible Navier-Stokes momentum equation in its most general, conservative form can be written in Einstein notation for an isentropic fluid as follows (Equ. 3.1),

$$\frac{\partial \rho u_i}{\partial t} + \frac{\partial \rho u_j u_i}{\partial x_j} = -\frac{\partial p}{\partial x_i} + \frac{\partial \tau_{ij}}{\partial x_j} \tag{3.1}$$

where the viscous stress is defined in Equ. 3.2:

$$\tau_{ij} = \mu \left[\left(\frac{\partial u_j}{\partial x_i} + \frac{\partial u_i}{\partial x_j} \right) - \frac{2}{3} \frac{\partial u_k}{\partial x_k} \delta_{ij} \right] \tag{3.2}$$

The left hand side includes the unsteady and convective terms, while the right hand side consists of the pressure, external forces and viscous stresses. Together with the conservation equations for mass (Equ. 3.3) and energy (Equ. 3.4 for adiabatic flow, e = internal energy) this forms a system of partial differential equations to be solved within the domain.

$$\frac{\partial \rho}{\partial t} + \frac{\partial \rho u_i}{\partial x_i} = 0 \tag{3.3}$$

$$\frac{\partial\left(\rho\left(e+\frac{1}{2}u_ju_j\right)\right)}{\partial t}+\frac{\partial\left(\rho u_i\left(e+\frac{1}{2}u_ju_j\right)\right)}{\partial x_i}=\rho u_if_i-\frac{\partial pu_i}{\partial x_i}+\frac{\partial}{\partial x_i}\left(k_t\frac{\partial T}{\partial x_i}\right)+\frac{\partial v_j\tau_{ij}}{x_i} \tag{3.4}$$

Solving the complete Navier-Stokes equations in so-called direct Navier-Stokes (DNS) simulations, however, takes vast amounts of calculation power and time and has only be done for low Reynolds number flows on simple domains and boundary conditions. The exponential scaling of computational effort with increasing Reynolds number makes it unlikely that industrial turbomachinery problems can be solved with DNS calculations in the foreseeable future. While DNS can provide valuable insight in transition mechanisms and helps understanding flow phenomena, it is currently of no use for high Reynolds number flows on complex geometries, as encountered in industry. An efficient technique is to only resolve the larger scales and simulate the effects of the smallest scales by a model (LES - large eddy simulation). This, however, is not yet widely used in industry and still uses a considerable amount of computational resources on complex geometries for large Reynolds numbers.

Most codes and commercial software packages used in industry are based on the Reynolds averaged Navier-Stokes (RANS) equations, where the desired quantity is split up into its average value and a fluctuating component $u=\bar{u}+u'$, known as Reynolds decomposition. Boussinesq' hypothesis is used and the equations consequently averaged to represent the mean flow. The turbulent stress tensor represents the influence of the fluctuating quantities on the mean flow and is replaced by different models. Turbulence is therefore, in contrast to LES and DNS not resolved, only modeled. For different geometries and flow problems, different models have been developed. Prominent examples are the one-equation Spalart-Allmaras model, the two-equation $k-\omega$ and $k-\epsilon$ models and the Reynolds stress models (RSM), calculating the individual Reynolds stresses for a second order closure.

The general equation solved during the processing step has the form shown in Equ. 3.5 with boundary and temporal conditions corresponding to the problem solved.
$U=(\rho,\rho u_x,\rho u_y,\rho u_z,\rho e)^T$ represents the state vector with e the total energy per unit mass and $\vec{u}=(u_x,u_y,u_z)$ the flow velocity in Cartesian coordinates. $\vec{F}^c(U)$ are convective fluxes, $\vec{F}^v(U)$ represent viscous fluxes and $Q(U)$ is a generic source term. Both TRACE and SU2 use this general formulation. However, being specifically developed for turbomachinery applications, TRACE solves the equations in a rotating frame of reference. The complete derivation of the standard formulation of the individual terms for SU2 is presented by F. Palacios et al. [16].

$$\frac{\partial U}{\partial t}+\nabla\cdot\vec{F}^c-\nabla\cdot\vec{F}^v=Q\ \ in\ \Omega,t>0 \tag{3.5}$$

The following sections give a short introduction of the two solvers used during the analysis of the curved duct and exit guide vane flow.

TRACE

Together with the DLR (German center for aerospace engineering), the aircraft engine manufacturer MTU aero engines developed the turbomachinery RANS solver TRACE, which is

also used by SIEMENS Energy for gas turbine applications. The state-of-the art code provides a solver for structured, unstructured and hybrid meshes and is based on a finite-volume method approach, using Roe's flux-difference splitting method for inviscid fluxes and different time integration schemes. The code includes different turbulence and transition models with a number of modifications and extensions specifically designed for turbomachinery flows.
For unsteady calculations, the harmonic-balance approach [51,52] and a time-linearized method are implemented. A discrete adjoint solver [53] can be used to compute sensitivities of objective functionals. The discrete adjoint method has been used successfully for optimization problems involving different geometries. An example for the optimization of a curved subsonic duct can be found in a study performed by B. J. Lee et al. in 2007 [54]. TRACE has been used and validated over many years in the design of industrial and aircraft multi-stage turbines and compressors.

SU2

For comparison with a second solver, the compressible open-source code SU2 [16], initially developed at Stanford University, is used. It relies on contributions from a large community of researchers. Being an inherently compressible solver and providing a clear project-oriented and publicly accessible source code, SU2 is chosen as a second RANS solver for comparison to the results obtained from TRACE. SU2, in contrast to TRACE, relies on unstructured meshes.

The SU2 suite consists of several C++ analysis modules that are written to handle specific jobs, including a RANS CFD solver, domain decomposition code for parallel computing, mesh adaptation, uncertainty quantification, and a mesh deformation code for shape optimization or aero-structural simulations [16]. Like TRACE, SU2 also uses a Finite Volume (or alternatively Finite Element) approach and is capable of parallelization, using both multi-grid and linear solvers. For turbulence modeling it employs the Spalart-Allmaras (one-equation) and SST model (two-equation, a blending of the popular k-ω and k-ϵ models [55] and used during this analysis). Convective fluxes can be calculated using a number of schemes, including JST, Lax-Friedrich, Roe, AUSM, HLLC and Roe-Turkel [16]. Time-integration is performed either implicit or using a Runge-Kutta scheme. Other capabilities of SU2 include nonlinear multi-grid methods for convergence acceleration, preconditioning, dynamic meshes and mesh adaptation. The real strength of SU2, however, is the coupling of individual modules in order to perform complex activities, such as shape optimization or adaptive grid refinement [16].

Both codes provide the functionality needed to analyze the problem. Various sources and studies state that the RANS equations and turbulence models used are capable of simulating and capturing the flow phenomena in a curved duct [17, 34, 56]. In terms of the turbulence model of choice, previous calculations of compressible viscous flows in curved ducts show improved compliance with experimental results for the SST turbulence model [55, 57], especially in adverse pressure gradient boundary flows. The RSM model was found to successfully predict the turbulence dissipation due to convex curvature, but underpredicted the magnitude of turbulence amplification due to concave curvature [56]. Considering the increased computational cost for the second order closure RSM model however, this study restricts itself to the use of first order closure models. The $k - \omega$ model is therefore used in TRACE, while SU2 relies on the SST model.

SU2 is considered more flexible combining different modules and functionality to solve an optimization problem on a complex domain, while TRACE is considered more validated for internal, compressible flows including transition, separation and reattachment through its extensive use and improvement over the years. This might lead to better transition point prediction, which is a difficult task and often relies on empirical data [58].

3.3.3 Post-processing

Both the industrial turbomachinery solver TRACE and the open source framework SU2 are inherently compressible density based solvers, including the density in the state vector U. In order to draw conclusions from the RANS solution, the parameters of interest and dependent flow variables are calculated from the state vector U during post-processing. This section gives an overview of the parameters of interest that are calculated during post-processing to draw conclusions on the flow field and the aerodynamic efficiency of the geometry. Tools used during this analysis include Visual3D (freeware) and TecPlot (commercial), both being available at MTU Aero Engines and the TU Delft.

Output parameters

In order to compare different geometries and judge their aerodynamic efficiency, the parameters of interest are total pressure loss and the occurrence of secondary flows. In order to quantify those flow field properties, a number of output parameters are defined. Pressure loss is quantified using the loss factor ζ_v, where the total pressure loss is divided by the dynamic pressure (Equ. 3.6).

$$\zeta_v = \frac{\Delta p}{\frac{\rho}{2} u^2} \tag{3.6}$$

For reasons of data confidentiality, no absolute loss factor is given, but the loss factors are first divided by the results of a baseline geometry, $\zeta_{v_{ref}}$. The baseline geometry is taken as the EGV geometry with curved duct and $R_c/D = 1$, $l/D = 0.3$, standard plug shape, symmetrical EGV arrangement and complete swirl removal in the EGV. The non-dimensionalized values (Equ. 3.7) allow to directly analyze the effects of different geometry changes to the baseline geometry.

$$\zeta_{v_{rel}} = \frac{\zeta_v}{\zeta_{v_{ref}}} \tag{3.7}$$

While the main dependent variable of interest is the overall pressure loss through the EGV and exhaust duct geometry, other parameters are defined to quantify the direct influence of geometry changes on the flow field. Two parameters that quantify the asymmetry in the flow are given in Equations 3.8 and 3.9, as introduced in literature [59, 60]. While the $DC60$ value gives an indication of the pressure homogeneity, the $SC60$ quantifies the maximum local swirl. Both parameters are taken over an area spanning an arc of 60° and can therefore, when plotted for different arc segments, give an indication of the circumferential flow symmetry characteristics.

$$DC60 = \frac{\overline{p_{t,AIP}} - \overline{p_{t,60}}}{\overline{p_{t,AIP}} - \overline{p_{AIP}}} \tag{3.8}$$

$$SC60 = \frac{\left|\vec{u}_{\phi,max,60}\right|}{\left|\vec{c}_{AIP}\right|} \tag{3.9}$$

For visualization of the flow field, streamlines are found from the velocity vector field by integration and are used together with iso-lines, cuts, vector plots and iso-surfaces to find regions of separation and other flow phenomena for more detailed investigation.

3.4 Grid convergence

To show sufficiency of the mesh quality, the calculation is run on meshes using different resolutions. In order to resolve the boundary layer, a first cell height of $y^+ \sim 1$ is required, as discussed in Section 3.3.1. With a moderate cell growth this results in an initial mesh of around 12 M cells. In order to test the sufficiency of the mesh, several refined meshes with higher cell counts and one coarser mesh are tested and the solutions compared. The total aerodynamic efficiency, expressed as ζ_v, for the different mesh sizes is shown in Fig. 3.23.

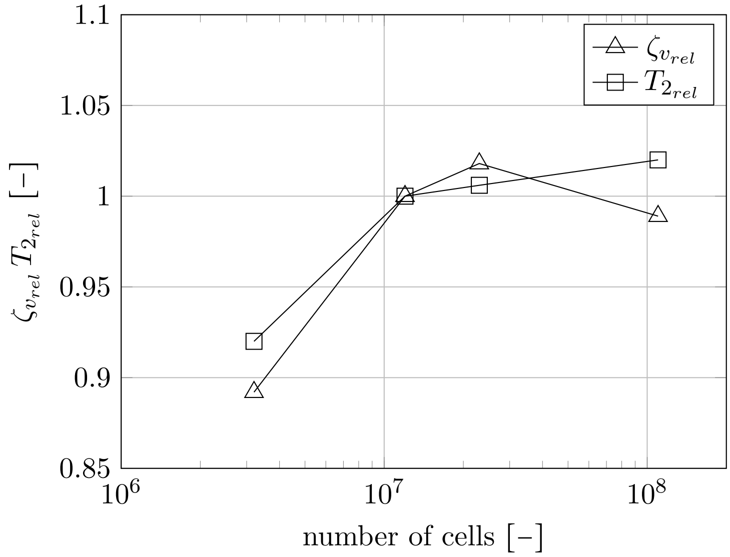

Figure 3.23: Relative pressure loss factor $\zeta_{v_{rel}}$ and exit temperature $T_{2_{rel}}$ for meshes of different cell count (non-dimensionalized with results for 12 M cell mesh)

As can be seen, further refining the mesh does not lead to considerable changes in pressure losses. Some of the observed variations are assumed to occur due to the unsteady and oscillatory behavior of the flow.

The streamwise velocity field of two different meshes is shown, using 12 M and 110 M cells, respectively. While the finer mesh requires considerably more computational time and resources, its solution shows only minor variations to the solution of the 12 M cell mesh. It is therefore concluded that for the aerodynamic analysis and sensitivity study a mesh of 12 M cells provides sufficient accuracy for lower computational time and cost. For coarser meshes, the pressure loss differs significantly, as presented in Fig. 3.23 for a mesh count of 3.2 M cells.

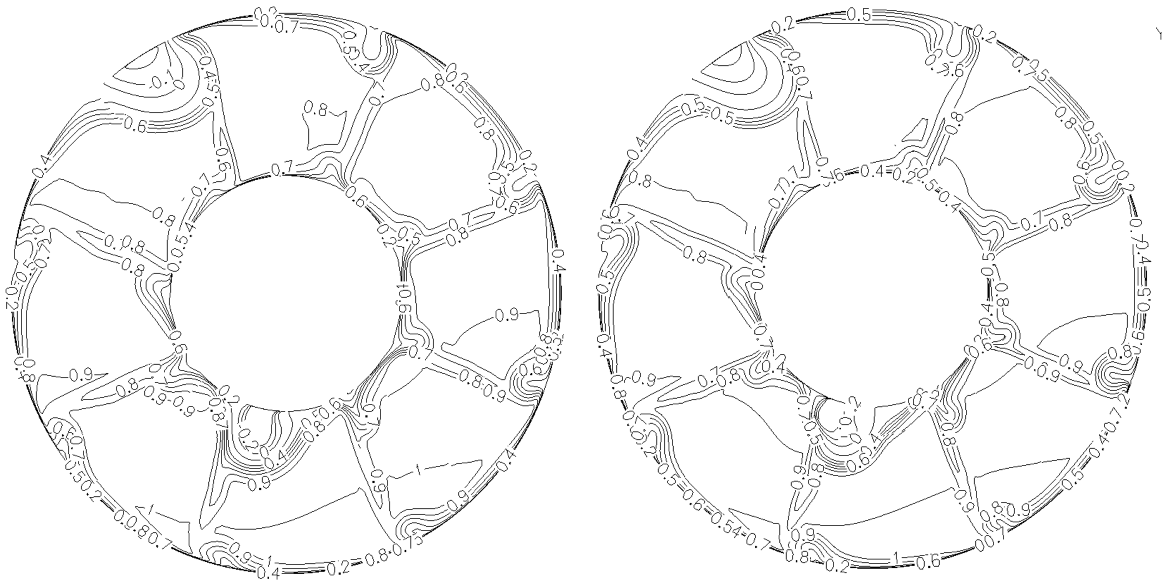

(a) 12 M cells **(b)** 110 M cells

Figure 3.24: Non-dimensional streamwise velocity at $\phi = 0°$ for curved duct ($R_c/D = 1$) using different mesh resolutions

3.5 Validation

In order to validate the numerical method proposed, a pilot study is performed. However, due to the high Reynolds number of $Re \sim 10^6$ and complex geometry, physical testing is beyond the scope of this research. A test case is therefore chosen, for which experimental data for validation is available from literature, as presented in Chapter 2. The test case closely resembles the curved exhaust duct (without EGV) to ensure that the method is validated for the similar geometry of a highly curved flow. The sharpness of the curved (elbow) duct is chosen to be $R_c/D = 1$ with an inlet Mach number of 0.25, leading to a Reynolds number in the post-critical regime ($Re > 2\text{x}10^5$) and negligible compressibility effects. This ensures dynamic similarity between the test case and the real exhaust duct without exit guide vanes. The test case geometry is shown in Fig. 3.25, together with the aerodynamic interface planes (AIP) H-J for validation purposes. A positive validation ensures that the solver is capable of correctly handling the effects of the high temperature internal exhaust flow in a curved geometry.

The test case is first calculated using the RANS solver TRACE. In two separate calculations both a flat and a fully developed inlet velocity profile are used to validate the method for different inlet profiles. The fully developed profile is defined to resemble the profile used in the

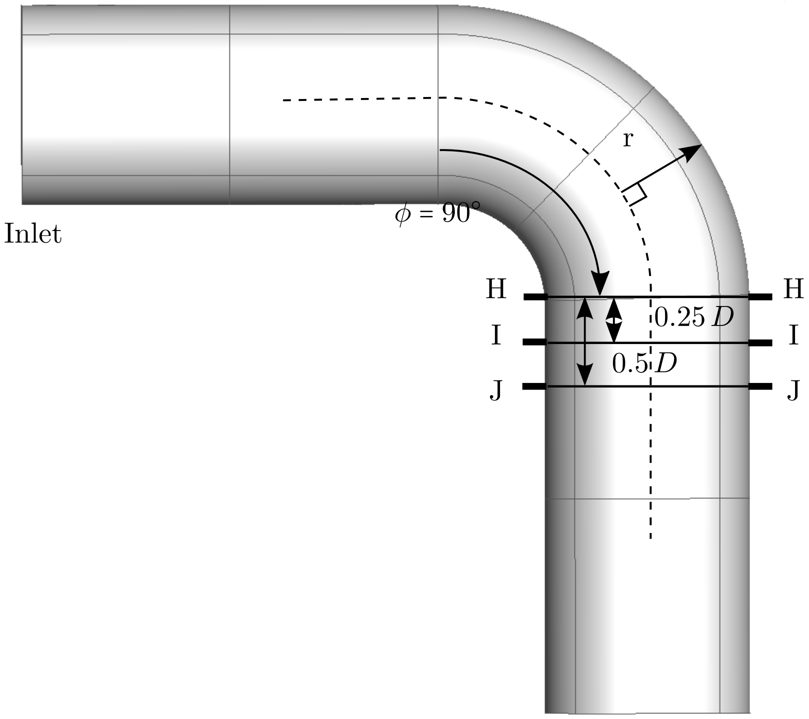

Figure 3.25: Test case geometry of elbow duct and AIP definition for validation

study of Kawamura et al. [25] for comparability of the results. The resulting velocity profiles at two positions downstream of the bend are plotted together with experimental values from literature in Fig. 3.26. It can be seen that the numerical results show the same, experimentally observed, phenomena of separation at the convex wall and downstream reattachment. The TRACE result for a flat inlet profile closely resembles the experimental results obtained by Ono et al. [8], where a flat inlet profile was generated by the use of a buffer tank. The SU2 results differ from the experimental results by showing a larger separation region with reattachment occurring later (Table 3.3). The difference is assumed to result from the turbulence model used, in combination with the high sensitivity of the separation region to small changes in the flow field.

The TRACE calculation for a fully developed profile almost directly matches the experimental results from Kawamura et al. [25] at $\phi = 90°$, who also used a developed profile. Further downstream, the TRACE result for a fully developed profile slightly deviates from the experimental results, showing a larger region of separated flow. This difference is assumed to result from minor differences in the inlet profile, showing a strong sensitivity of the separation region to changes in inflow conditions. Some differences may also result from the turbulence model not being able to capture all wall curvature effects.

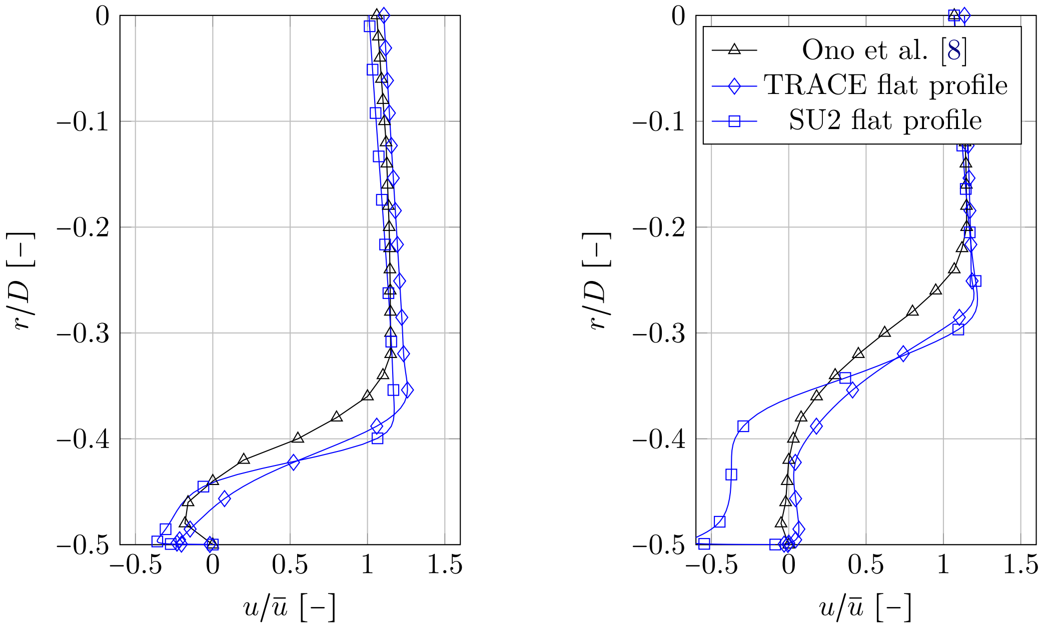

(a) at plane H, $\phi = 90°$ **(b)** at plane I, $0.25\,D$ downstream

Figure 3.26: TRACE and SU2 streamwise velocity results compared to experimental results for velocity profile after elbow bend at different streamwise positions (AIPs) for flat inlet profile

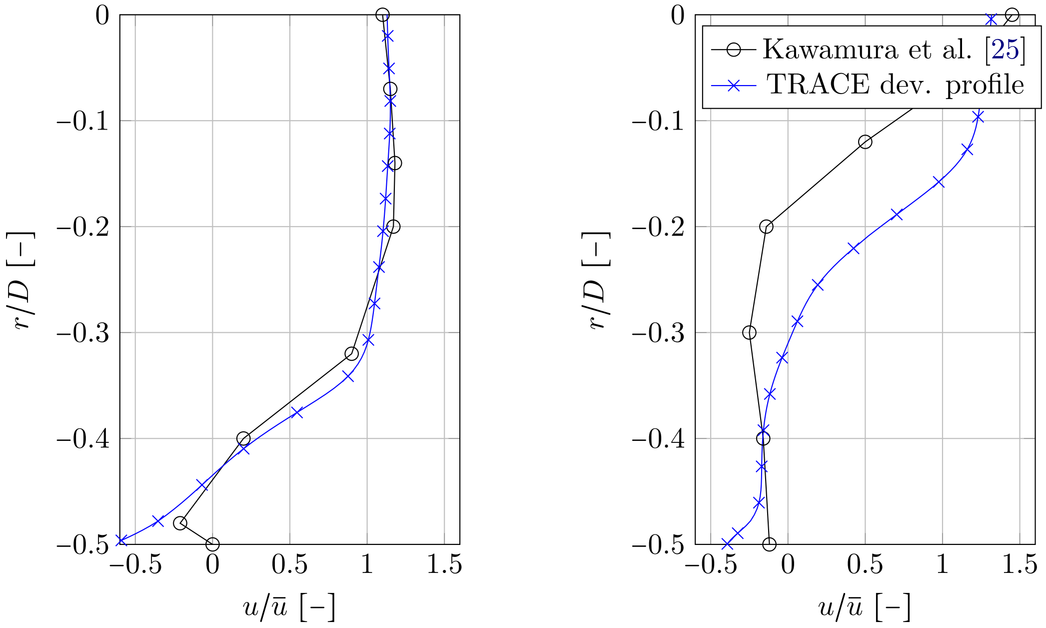

(a) at plane H, $\phi = 90°$ **(b)** at plane I, $0.25\,D$ downstream

Figure 3.27: TRACE streamwise velocity results compared to experimental results for velocity profile after elbow bend at different streamwise positions (AIPs) for developed inlet profile

After comparison of the streamwise velocity profiles with experimental results from literature, the secondary flow structures after the bend, obtained from TRACE calculations, are

	reattachment point
Ono et al. [8]	$0.27\,D$
TRACE flat profile	$0.24\,D$
SU2 flat profile	$0.48\,D$

Table 3.3: Point of reattachment, given downstream of the bend for flat inlet profile

presented in Fig. 3.28 together with experimental PIV measurements from Ono et al. [8].

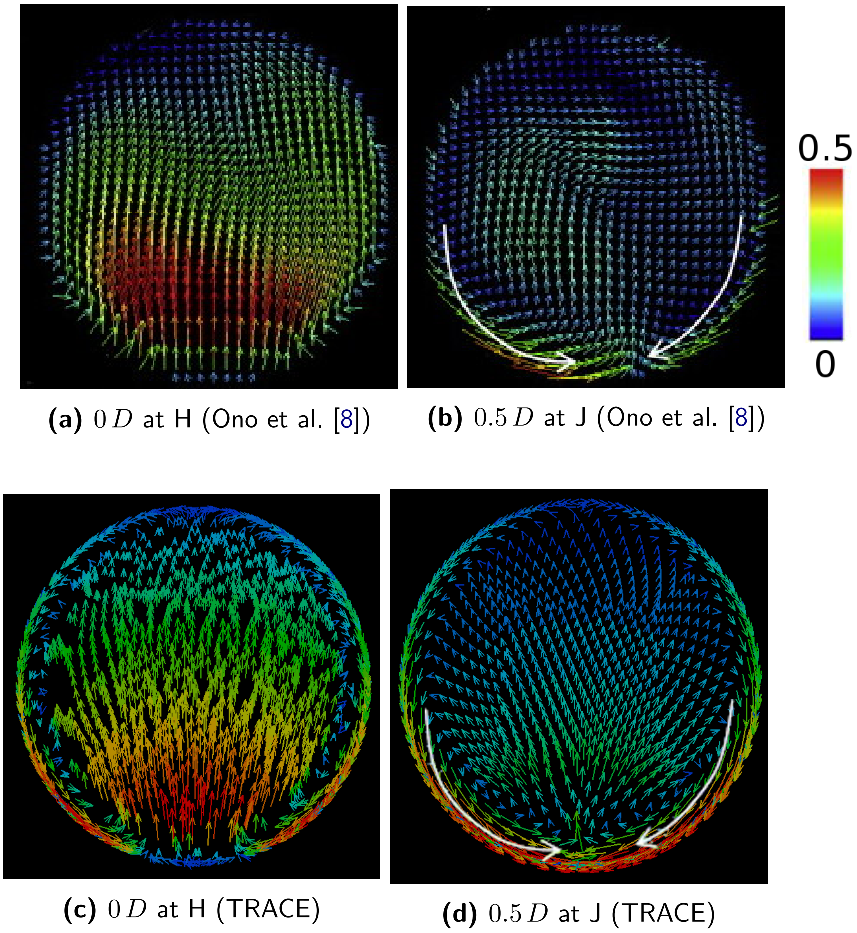

(a) $0\,D$ at H (Ono et al. [8]) **(b)** $0.5\,D$ at J (Ono et al. [8])

(c) $0\,D$ at H (TRACE) **(d)** $0.5\,D$ at J (TRACE)

Figure 3.28: TRACE results compared to experimental results for secondary flow velocities ($u_{xy}/\bar{u}$) after elbow bend at different streamwise positions

Centrifugal forces, acting on the flow in the bend, transport fluid towards the outer duct wall. The air then flows back along the side walls, creating a pair of counter-rotating Dean vortices (Section 2.2). This behavior is observed both from the experimental PIV measurements and from the TRACE results. The strongest secondary flow structures exist at the convex wall. Further downstream, the duct secondary flow velocities decrease and the flow becomes more axial. The effect of the Dean vortices can still be seen and high velocities at the lower side of the duct walls persist. However, some differences between experimental and numerical results, mainly at $0.5\,D$ downstream of the bend, can be observed as well. While the numerical solution is almost fully symmetric, the experimental results show some asymmetry. This is explained by the oscillatory nature of the vortex structures determining the secondary flow field, as shown by the asymmetric experimental results. While the measurements have been time-averaged by Ono et al. [8], the irregular behavior of vortex structures, together with possible irregularities in the test setup, still lead to some asymmetry in the solution. From the validation with experimental data it is concluded that the flow field in a curved duct can be modeled with sufficient accuracy using the RANS solver TRACE. The numerical approach allows to carry out a sensitivity study on the complete geometry presented in Section 3.3.1 to investigate different ways of improving the aerodynamic efficiency.

In order to also validate the solver for curved flows involving swirl, the same test case is calculated for an inlet condition with $\alpha_2 = 20°$ of swirl. This can be of importance as swirl was found to increase the aerodynamic efficiency during several studies on curved ducts, as stated in Chapter 2. Table 3.4 shows the results for the pressure loss factor for both 0° and 10° of swirl. The streamwise total pressure factor λ (Equ. 3.10) is defined to measure the energy available for propulsion purposes relative to the reference geometry.

$$\lambda = \frac{\left(\overline{p + \frac{1}{2}\rho u_k^2}\right)_{exit}}{\left(\overline{p + \frac{1}{2}\rho u_k^2}\right)_{exit,ref}} \tag{3.10}$$

	$\zeta_{v_{rel}}$	λ
$\alpha_1 = 0°$	1	1
$\alpha_1 = 20°$	0.907	0.9974

Table 3.4: Effect of swirl in a curved duct on total pressure loss and streamwise total pressure

It can be seen how swirl, for the used sharpness parameter of $R_c/D = 1$, decreases the total pressure loss. At the same time, however, the total outlet pressure is decreased, when only the stream wise velocity component is considered for the dynamic pressure. Straightening the flow at this point is made difficult by the complex and unsteady flow pattern, so that secondary flows represent energy that is lost for propulsion purposes. This findings match experimental results obtained by Maqsood et al. [40]. However, as stated by Roh et al. [38] and Birk et al. [39], the effects of swirl on efficiency and outlet propulsive energy are greatly influenced by the bend sharpness R_c/D. Based on the results matching experimentally found values from literature, the solver is considered to accurately predict the effects of inlet swirl.

3.6 Limitations

Besides the assumptions stated in Section 3.1.4, the research is limited by time and cost constraints. A large number of cells, in the order of 10 million, is needed for resolving all boundary layers and important flow phenomena in the 360° simulation. The resulting run times for a compressible RANS calculation depend on number and type of processors available, which pose an important limiting factor to the sensitivity study and optimization. Most optimization strategies depend on a large number of function evaluations and therefore become unfeasible when a single RANS calculation takes several hours to converge. The resources available are used in a more efficient way by dividing the domain into blocks for parallel computation and by using a structured multi-grid approach for shorter run times with TRACE.

The availability of software presents a second limiting factor, as licenses are not available for all commercial pre- and post-processing tools at MTU Aero Engines and the TU Delft. While the turbomachinery solver TRACE is only accessible through the MTU cluster, SU2 cannot be set up and run at MTU due to company security protocols. Therefore, all TRACE calculations are performed on the computer cluster at MTU in Munich, while SU2 calculations are performed on the computer cluster hpc12 of the Aerospace Faculty at the TU Delft. In order to get comparable results, the structured multi-block mesh created at MTU is directly transformed into an unstructured hexagonal mesh of the native SU2 format, keeping the same cell and node number and positions. For post-processing, the tool TecPlot, available both at MTU and the TU Delft, is chosen to ensure a consistent output data format, re-usability of post-processing scripts and comparison of results. MTU's confidentiality policy is respected and obligatory security procedures followed in all cases where geometry data is transferred from MTU to the TU Delft and vice-versa. The time restriction for the whole research, including the study of background literature, is a total period of nine months.

Chapter 4

Results

The following chapter sets out to present and discuss the results, obtained by employing the methods presented in Chapter 3, and to answer the individual research questions stated in Section 3.1. During the first part of the chapter, the main flow phenomena in an exit guide vane followed by a curved duct are analyzed by comparing the results to the flow field of an EGV with a straight exhaust duct. The mutual effects of the EGV flow on the curved duct flow, and vice versa, are shown and discussed. In the subsequent sensitivity study, the effects of geometry changes on the flow field are presented. Investigated parameters are the radius of curvature R_c, the distance between the EGV exit and the bend l, the residual swirl α, the plug shape, and the circumferential EGV positioning θ_{EGV}. From the sensitivity study, correlations between pressure losses and geometry changes are derived and the most promising geometry changes stated, to improve the aerodynamic efficiency of future designs.

4.1 EGV with straight vs curved duct

This section gives a first overview over the flow phenomena occurring in an exit guide vane with both a straight and a 90° curved exhaust duct, focusing on asymmetric flow phenomena caused by the 90° bend. Separation zones and pressure losses in the curved duct are shown and related to the radial pressure gradients caused by the bend. Finally, the upstream effect of the bend on the EGV flow and the effect of the EGV wake on the curved duct boundary layer are analyzed.

4.1.1 Flow through an EGV followed by a straight duct

In a first step, the exit guide vane and plug geometry is connected to a straight duct and the flow solution calculated using the RANS solver TRACE with the boundary conditions stated in Chapter 3. The resulting absolute streamwise velocity of the periodic domain at mid-section ($y = 0$) is shown in Fig. 4.1. In general, higher velocities are found at the EGV that tend to decrease towards the outlet of the duct. This effect is mainly due to the transition from an annular to a circular cross-section at the plug, leading to an increase in cross-sectional area and an expansion of the flow. This, in turn, induces an adverse pressure gradient and a decrease in flow velocity. Especially at the plug walls the decrease in velocity eventually leads to flow separation. More detailed information on the straight duct flow field is presented during the comparison with a curved duct in Section 4.1.2.

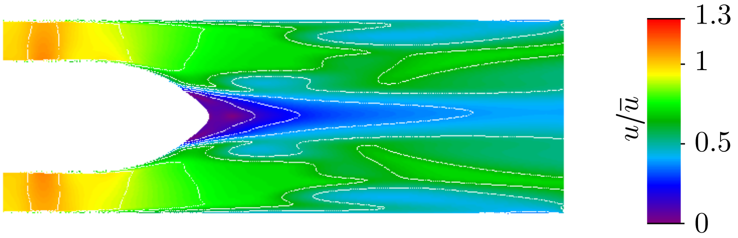

Figure 4.1: Absolute flow velocity $u/\bar{u}$ at $y = 0$ for straight duct

4.1.2 Flow phenomena in the curved duct

With the reference flow field of a straight duct for comparison, the flow through the curved duct geometry presented in Chapter 3 is analyzed and the main flow phenomena caused by the bend identified. Figure 4.2 presents the TRACE solution for the absolute velocity at $y = 0$, showing three regions of separation at the curved walls and the plug, when compared to the straight duct solution.

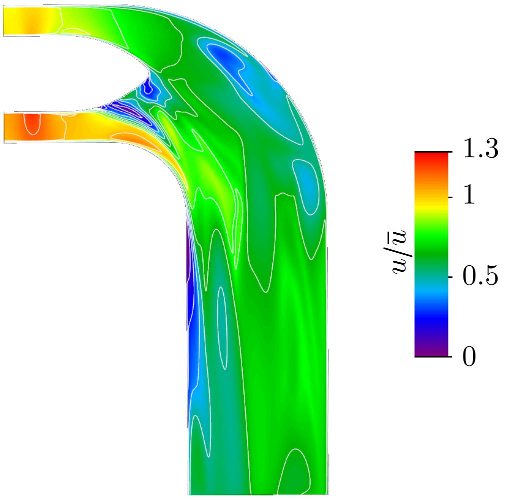

Figure 4.2: Absolute flow velocity $u/\bar{u}$ at $y = 0$ for curved duct ($R_c/D = 1$)

Figure 4.3 directly compares the velocity profiles at different streamwise aerodynamic interface planes (at $y = 0$) with the straight duct solution, showing the developing radial velocity gradient. The flow in the straight duct shows an entirely symmetric velocity profile with higher velocities in the core flow and a low velocity zone in the wake of the separated plug flow. The curved duct, however, develops a significantly asymmetric velocity profile. The curved flow shows a higher velocity on the convex side of the duct and experiences a large region of low velocity flow on the lower plug side (Fig. 4.3b).

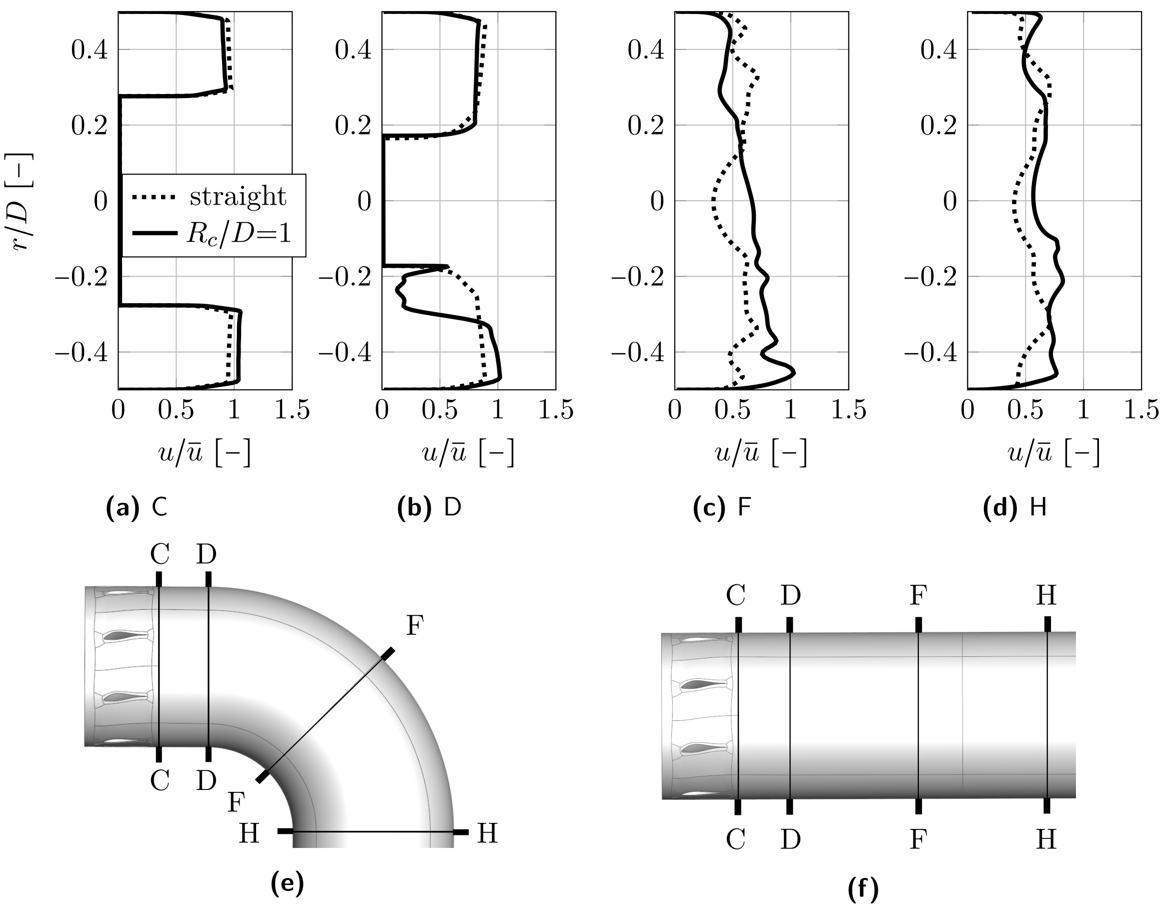

(a) C **(b)** D **(c)** F **(d)** H

(e) **(f)**

Figure 4.3: Velocity profiles for straight and curved duct at corresponding streamwise cross-sections (same mean-line duct legth)

The separation zones along the concave and convex walls of the bend can be understood by looking at the static wall pressure along the concave and convex sides of the duct, as shown in Fig. 4.4.

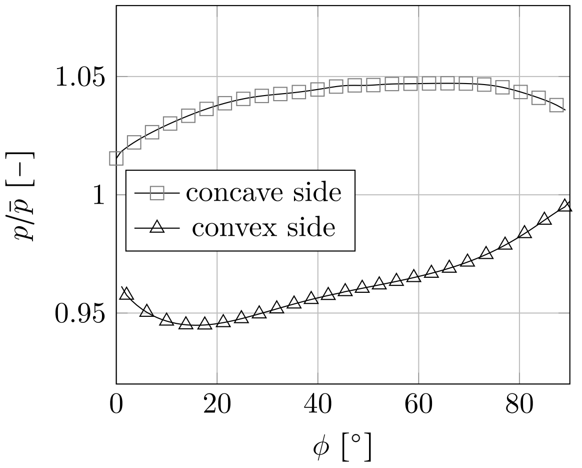

Figure 4.4: Static pressure along concave and convex bend walls

The asymmetric behavior of the wall pressure along the concave and convex sides, respectively, is a direct consequence of the bend. First, the flow is accelerated along the inner (convex) side of the duct at $r/D = -0.5$, while being decelerated on the outer (concave) side at $r/D = 0.5$. On the concave side, the pressure is rising through almost the entire bend due to both curvature and flow expansion, caused by the transition from the annular EGV cross-section to the circular, considerably larger outlet section. On the convex side, the static wall pressure is decreasing in the beginning as a consequence of the effects of centrifugal forces on the radial pressure distribution. From around 15° onward the static pressure is rising again, leading to flow separation towards the end of the convex wall.

Separation zones in an elbow duct are not necessarily occurring symmetrically at $y = 0$, as viewed in Fig. 4.2 and their dimension can be difficult to estimate. In order to give an overview over all separated areas for the curved duct with $R_c/D = 1$, iso-surfaces with a streamwise velocity magnitude of $u = 0$ are used to indicate separated zones red (Fig. 4.5). For different values of R_c/D, however, the individual separation zones can look very different.

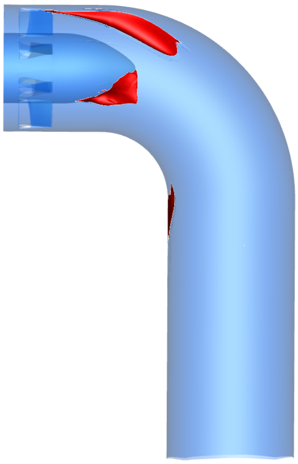

Figure 4.5: Iso-surfaces of zero streamwise velocity showing zones of separation for $R_c/D = 1$

To gain an impression on the circumferential dimension of the separated zones, the total velocity is plotted in Fig. 4.6 at the EGV exit. When compared to the straight exhaust duct, the curved duct shows a strongly asymmetric pattern of high and low velocity zones. While separation on the lower EGV side is suppressed, it is intensified on the upper EGV side. It can be seen how the asymmetric separation in the curved duct originates at the interaction of

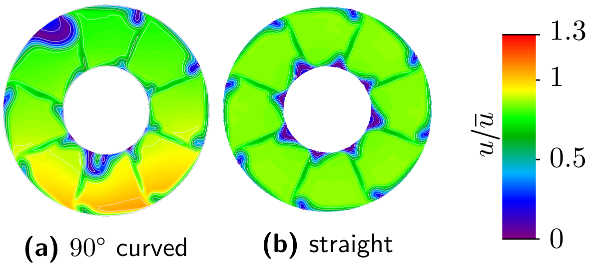

(a) 90° curved **(b)** straight

Figure 4.6: Absolute flow velocity for curved duct ($R_c/D = 1$) and straight duct at the EGV exit - left for curved duct, right for straight duct

the adverse pressure gradient and the low-velocity wake from the exit guide vane. Similarly, separation occurs for the straight duct geometry at the outer wall. The separation for the straight duct, however, is much smaller with no concave wall pressure gradient being present. For the straight duct, small areas of separation occur periodically at the locations of the low-velocity EGV wake, while the flow through the curved duct is dominated by separation zones caused by the convex and concave duct walls. This leads to considerably larger separation zones and pressure losses in the curved duct, presented in Table 4.1. The secondary flow pattern, caused by the flow expansion and Dean vortices in the curved duct, leads to the slight rotation of the EGV wake downstream.

The effect of the pressure gradient developing in the bend (Fig. 4.4) on the boundary layer is shown in Fig. 4.7.

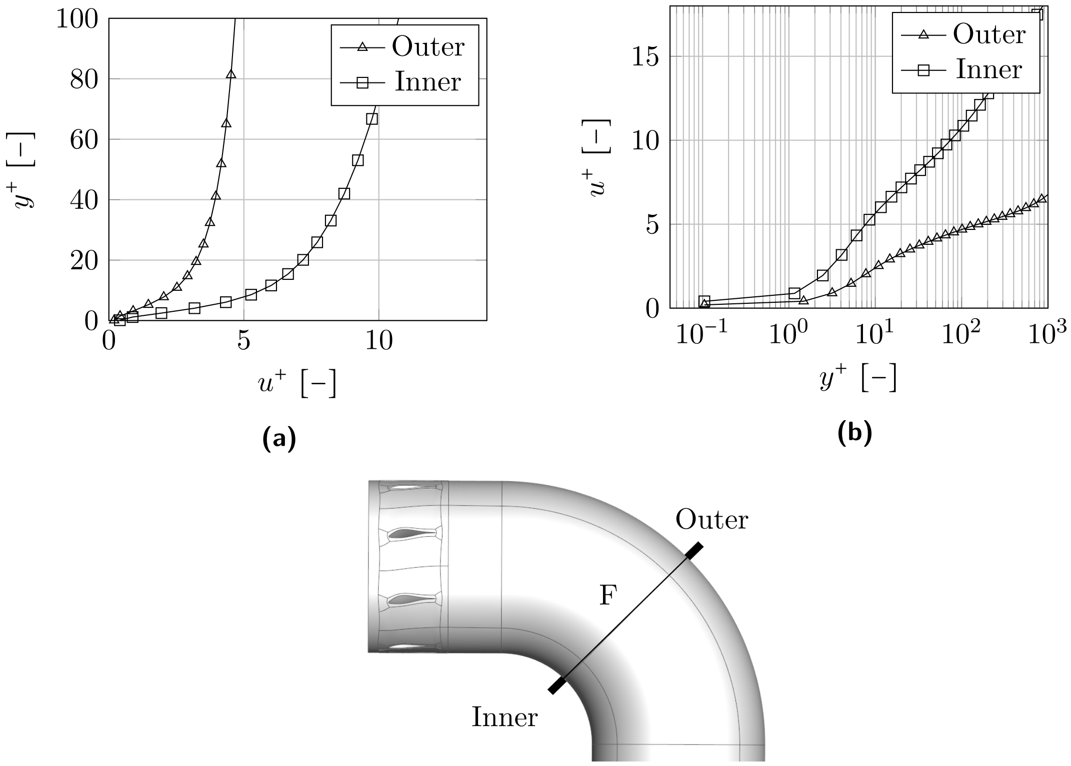

(a)

(b)

(c)

Figure 4.7: Boundary layer velocity profile at concave (Outer) and convex (Inner) walls at the 45° plane F

It can be seen from Fig. 4.7a how the adverse pressure gradient decelerates the flow along the outer wall, which in turn becomes more susceptible to separation. The flow on the inner side, however, is accelerated, leading to a more energized boundary layer. The logarithmic behavior in Fig. 4.7b shows how both profiles deviate from a flat plate profile.

Table 4.1 compares the pressure loss for a straight and for a curved duct. The pressure loss for an EGV followed by a curved duct is found to be about 72% higher than for an EGV connected to a straight duct. As both ducts use the same mean-line length, the losses are mainly due to flow separation and distortion caused by the secondary flows occurring in the bend. Besides this, the curved duct slightly accelerates the core flow, due to a decrease in cross-sectional area by the development of separation zones and growing boundary layers.

	$\zeta_{v_{rel}}$ [−]
90° curved duct	1.72
straight duct	1

Table 4.1: Pressure losses in the combined geometry with either a straight or a curved duct

4.1.3 Upstream effect of the curved duct

Due to pressure waves essentially being sound waves, disturbances in a subsonic flow also affect the upstream flow field. The curved duct therefore leads to an asymmetric flow field upstream of the bend and of the exit guide vane. Figure 4.8 gives a closer view on the flow asymmetry, showing the swirl and the absolute velocity in front of the exit guide vane. It can be seen how the total velocity is higher on the lower side, being accelerated towards the low pressure zone around the convex side of the bend. The opposite is true on the concave side of the bend, where an adverse pressure gradient leads to a decrease in flow velocity. At the same time, the upstream effect of the Dean vortices can be seen from the swirl distribution. By introducing a secondary flow, moving downwards at the outer duct walls, the Dean vortices increase swirl on one side of the duct and decrease it on the opposite side.

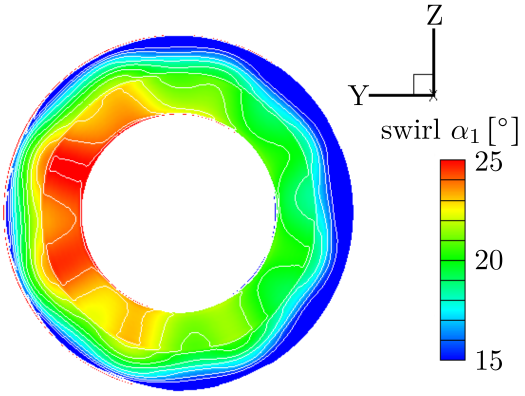

Figure 4.8: Upstream influence of Dean vortices on swirl distribution at the EGV inlet

This asymmetry in swirl and flow velocity leads to differences in the individual aerodynamic blade loading. Figure 4.9 shows this difference in pressure distribution over the individual vanes.

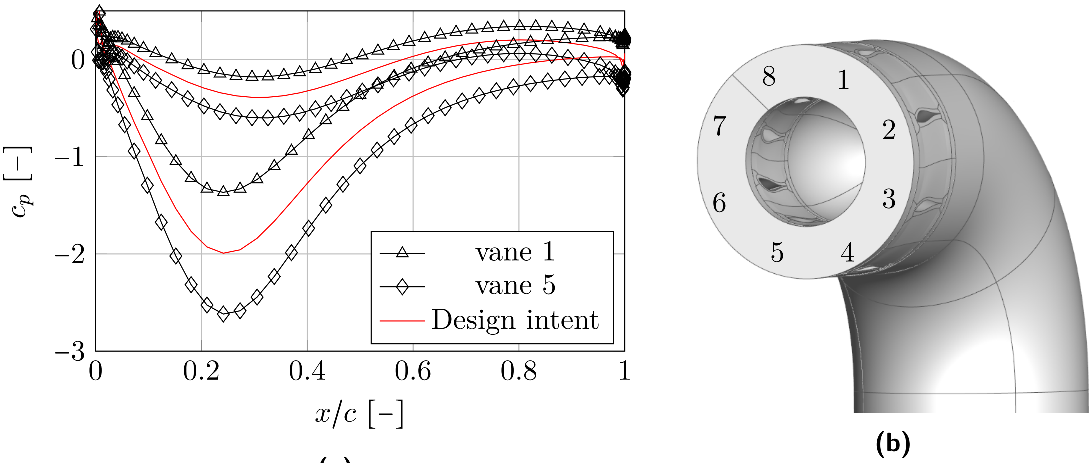

(a)

(b)

Figure 4.9: Pressure distribution for individual vanes (angle corresponds to circumferential position around x-axis) (a) and vane numbering (b)

The effect of the increased velocity on the lower duct side can be seen at the lower vanes, which are experiencing higher aerodynamic loading than vanes on the upper side. Secondly, the asymmetric swirl leads to different inflow angles for the individual vanes. The inflow angle is increased on the side where $y < 0$ and decreased for $y > 0$, when compared to the straight duct. The presence of the bend therefore causes considerable differences in the aerodynamic loading and incidence angle of the individual vanes, eventually leading to flow separation due to a local non-optimal inflow angle α_1.

Important factors to quantify the upstream effects of the bend are the $DC60$ and $SC60$, as introduced in Chapter 3. They are shown for the EGV with curved duct at different streamwise cross-sections in Fig. 4.10. For a straight duct, both parameters should show either a constant or a periodic behavior (with a period of eight, equal to the number of vanes) for both swirl and pressure fluctuations. Any deviation from constant or periodic $DC60$ and $SC60$ must be due to upstream effects of the elbow bend.

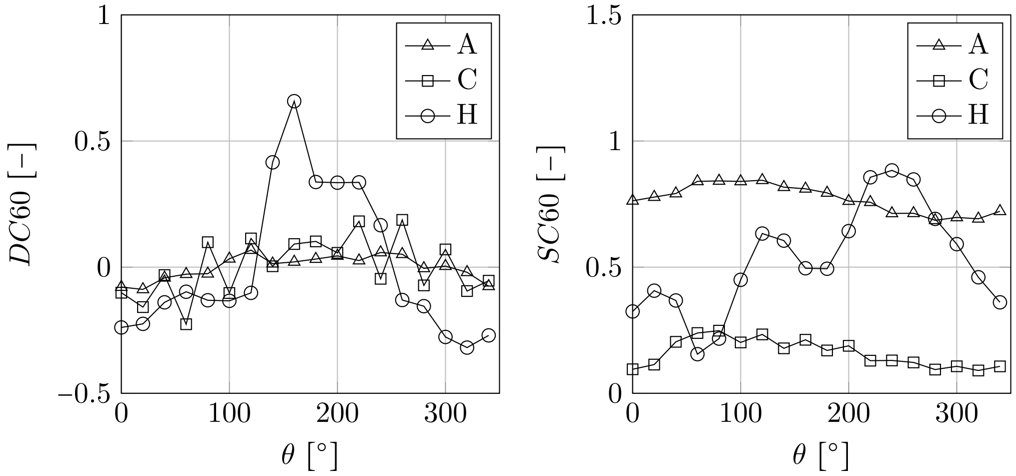

(a) $DC60$ **(b)** $SC60$

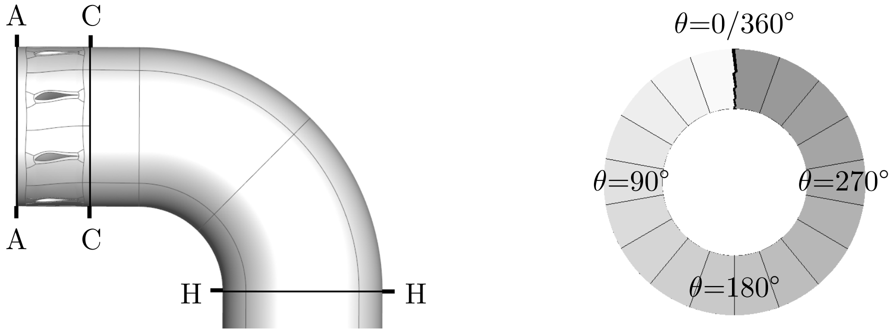

(c) **(d)** Front view on **A**

Figure 4.10: Asymmetry parameters $DC60$ and $SC60$ at different aerodynamic interface planes

When looking at the results presented in Fig. 4.10, the $SC60$ shows an almost constant swirl at the inlet plane. This is only influenced slightly by the pair of Dean vortices from the bend, increasing swirl on one side ($\theta < 180°$) and decreasing it on the opposite side ($\theta > 180°$). The bend influences the upstream pressure distribution at the inlet as well, as shown by the distribution of $DC60$. When looking at the EGV exit plane, one can clearly see that most of the swirl has been removed by the vanes, while the Dean vortex effect persists. From the $DC60$, the EGV wake can be seen as a periodic pattern of high and low pressure zones. At the bend exit ($\phi = 90°$), the Dean vortices are the main secondary flow phenomena, while pressure disturbances are highest on the convex side of the wall. For optimal operation of the EGV and exhaust geometry, the absolute values of both $DC60$ and $SC60$ should be minimized throughout the duct to allow for a uniform and efficient EGV airfoil design and high streamwise total energy at the exit. Especially a low $SC60$ at the duct exit is desired, as complex secondary flows are difficult to transform into streamwise propulsive energy. An analysis of the $DC60$ and $SC60$ for different bend radii R_c/D follows in Section 4.2.

4.1.4 Exit guide vane effect on curved duct flow

Besides the effect of the curved duct on the exit guide vane flow, the EGV wake also affects the flow through the curved duct. The inhomogeneous flow profile behind the EGV, entering the exhaust duct, shows a pattern of high and low velocity zones, created by the wakes of the individual vanes. The inhomogeneous wake pattern leads to regions of high and low energy zones and determines where separation is most likely to occur in the curved duct. This section takes a look at the wake influences on the boundary layer development and separation along the curved duct walls. Figure 4.11 shows the velocity and turbulent kinetic energy profiles of the boundary layer at the EGV exit plane at different circumferential positions (see Fig. 4.9b).

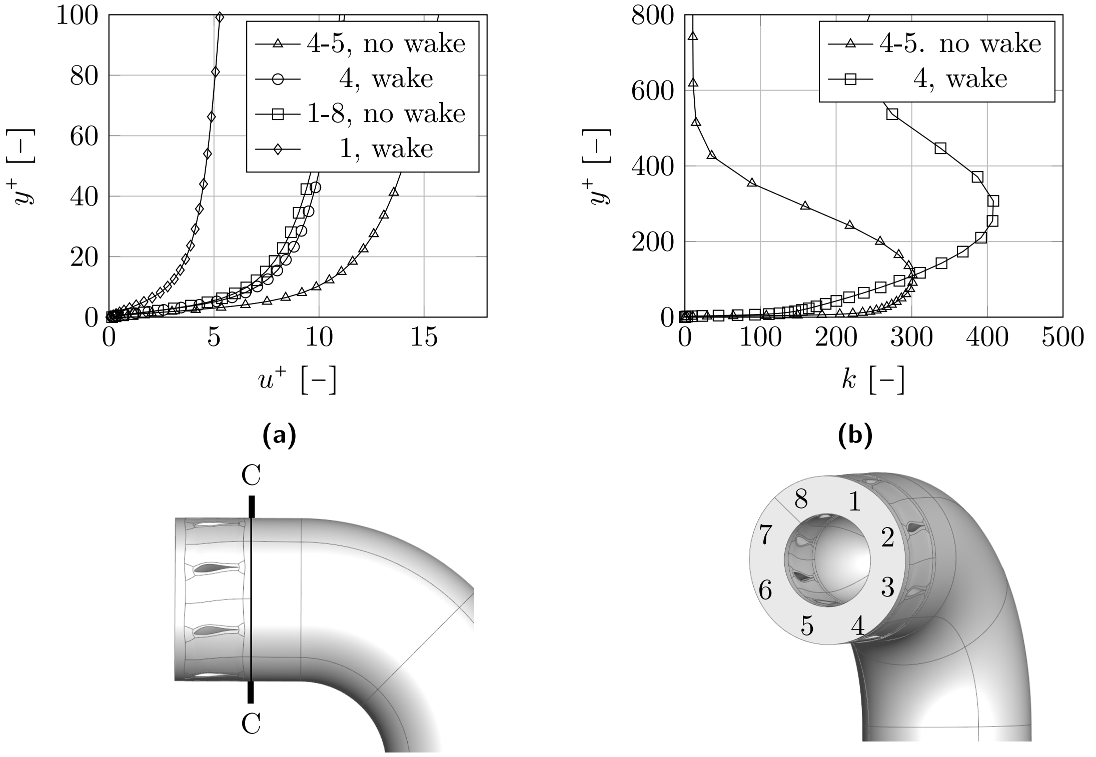

(a)

(b)

(c)

(d)

Figure 4.11: Influence of exit guide vane wake on the boundary layer at the EGV exit plane C

Where no wake is present, the velocity profile is fuller, showing a low shape factor caused by a small displacement and high momentum thickness. Turbulent kinetic energy close to the wall is higher, both on the upper (vanes 1-8) and lower side (vanes 4-5). Where a wake from an exit guide vane is present, velocity close to the wall decreases considerably and turbulent kinetic energy is shifted away from the wall. This leads to a high displacement thickness and shape factor. The regions where the EGV wake encounters an adverse pressure gradient are therefore highly susceptible to flow separation.

4.2 Sensitivity study

After the most important flow phenomena in the flow field of an EGV with curved duct have been shown, this section presents the effects of geometry changes, as stated in Section 3, on the flow field. Main parameters varied during the sensitivity study are: the bend radius R_c/D and the distance between the EGV and the bend l/D, as defined in Section 3. Their individual and combined effect on the flow field and pressure losses is investigated and recommendations given for design improvements. Furthermore, the remaining swirl at the EGV exit, α_2, the plug shape and circumferential EGV positioning θ_{EGV} are varied in order to determine their effect on the aerodynamic efficiency.

4.2.1 Radius of curvature

From the comparison between an EGV with a straight and a curved exhaust duct in Section 4.1, it can be concluded that the non-dimensional bend radius R_c/D must have an important effect on the flow solution and play a significant role in determining the pressure losses. This section sets out to investigate this relation and take a closer look at the effects of the sharpness parameter R_c/D on the aerodynamic efficiency. The sharpness parameter of the constant radius bend is varied in steps and the corresponding flow fields calculated using TRACE to develop a relationship between the sharpness factor, separation zones and pressure losses in the duct.

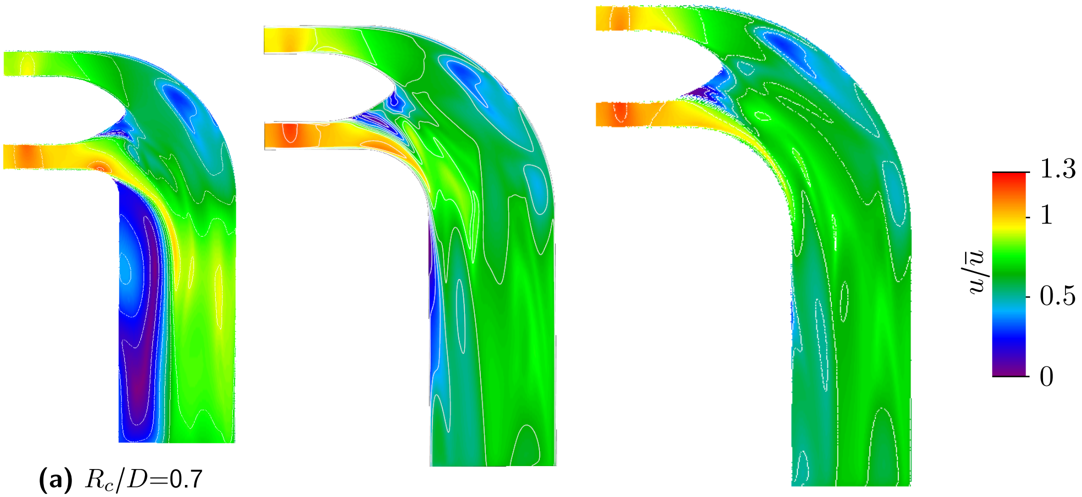

(a) R_c/D=0.7

(b) R_c/D=1

(c) R_c/D=1.3

Figure 4.12: Absolute flow velocity for different duct radii

Figure 4.12 shows the absolute flow velocities for different R_c/D at $y = 0$. It can be seen how separation on the convex duct wall decreases rapidly for larger R_c/D. Similarly, as shown in the cross-sectional cuts in Fig. 4.13, separation at the intersection of the EGV wake and the adverse pressure gradient along the concave wall decreases for larger bend radii.

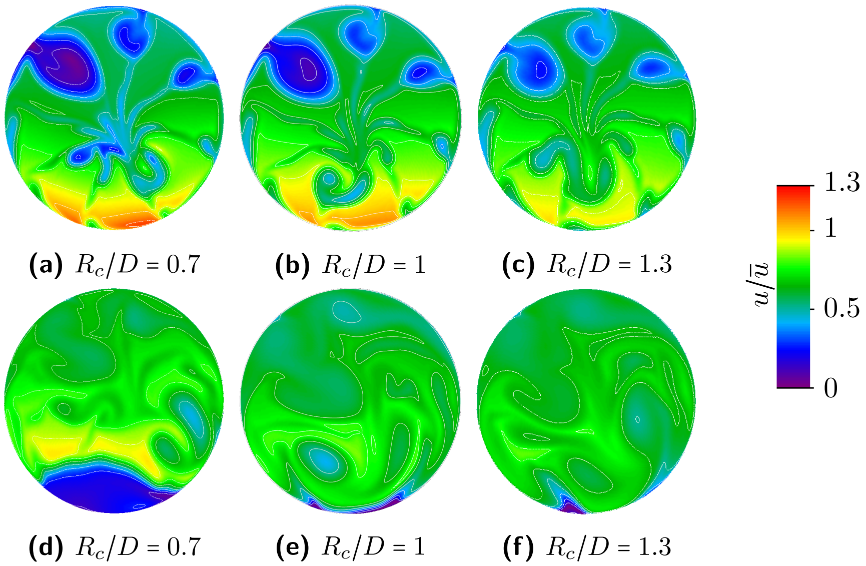

(a) $R_c/D = 0.7$ **(b)** $R_c/D = 1$ **(c)** $R_c/D = 1.3$

(d) $R_c/D = 0.7$ **(e)** $R_c/D = 1$ **(f)** $R_c/D = 1.3$

Figure 4.13: Absolute flow velocity for different R_c/D at various positions along the duct. First row (**(a)**-**(c)**) at position $\phi = 30°$, second row (**(d)**-**(f)**) at $\phi = 90°$

From Fig. 4.14, it can be seen how the separated regions translate into generation of turbulent viscosity, indicating the transfer of momentum by turbulent eddies. This process is similar to the momentum transfer occurring in the case of friction, as modeled with molecular viscosity, and contributes to the overall pressure losses.

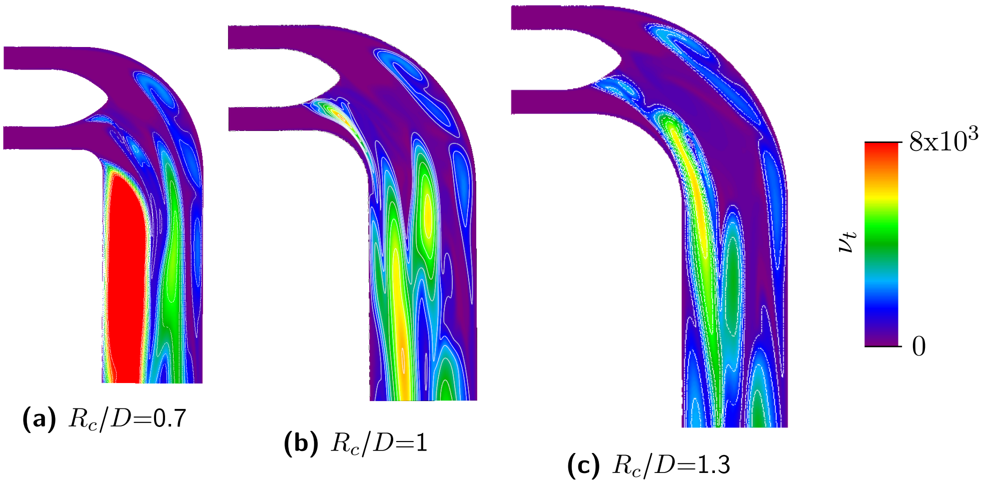

(a) R_c/D=0.7 **(b)** R_c/D=1 **(c)** R_c/D=1.3

Figure 4.14: Turbulent viscosity for different duct radii

Furthermore, some mutual influences seem to exist between separation at the plug and at the convex wall, where high velocity fluid is moving between the outer wall and the plug. When separation occurs on either side, fluid is directed towards the opposite side, re-energizing the flow close to the wall and delaying flow separation. This effect is observed in Fig. 4.12a ($R_c/D = 0.7$), where the large separation zone on the convex side directs the high velocity core flow slightly upwards, delaying separation on the lower plug side, when compared to Fig. 4.12b ($R_c/D = 1$). These effects show a more complicated relation between radius of curvature and flow separation. While, generally, losses tend to increase with smaller R_c/D, outliers exist due to the mutual influences of individual separation zones.

Figure 4.15 presents the velocity profile for different sharpness factors and shows how the radial velocity gradient increases with a decrease in R_c/D. Large flow separation zones at the plug and convex wall can be seen, that decrease with increasing R_c/D.

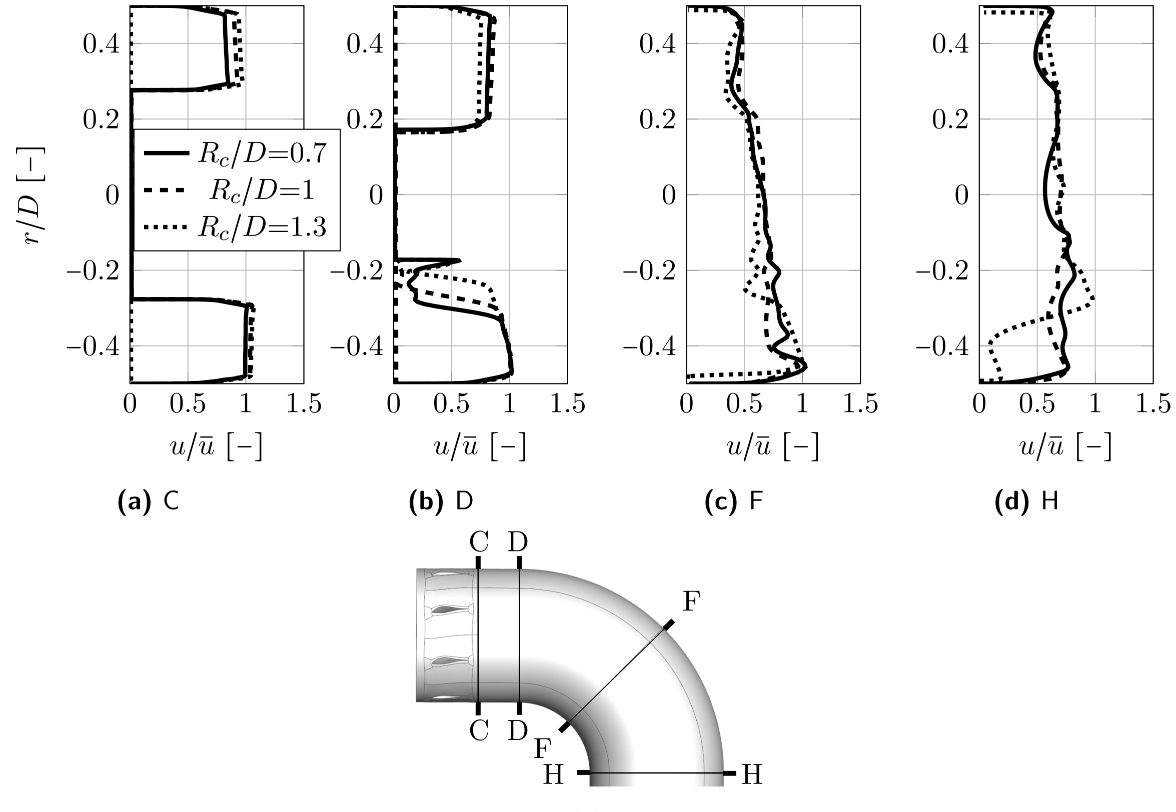

(a) C **(b)** D **(c)** F **(d)** H

(e)

Figure 4.15: Velocity profiles for curved ducts of different R_c/D at corresponding streamwise cross-sections

Table 4.2 shows how pressure losses are increasing with decreasing R_c/D. However, the complex mutual effects between individual separation zones can lead to outliers, as seen for the cases of $R_c/D > 1$. For very high R_c/D, flow separation on the convex wall becomes negligible and increasing R_c/D does not further increase the aerodynamic efficiency. When increasing R_c/D, the total mean-line length also increases, leading to higher friction losses. At very high R_c/D, this can offset the decrease of secondary flow losses, making any further increase of R_c/D undesirable. However, geometric restrictions for most aerospace applications will usually prevent such large bend radii.

$R_c/D\,[-]$	$\zeta_{v_{rel}}\,[-]$
0.7	1.403
0.85	1.065
1	1
1.15	1.013
1.3	0.889

Table 4.2: Pressure losses for different radii of curvature

4.2.2 Effect of bend radius on flow symmetry

Different bend radii R_c/D change the relative strength of secondary flows and therefore directly influence flow distortion both downstream of the bend and upstream of the exit guide vane. The parameters $DC60$ and $SC60$ are used to assess the flow asymmetry in terms of pressure

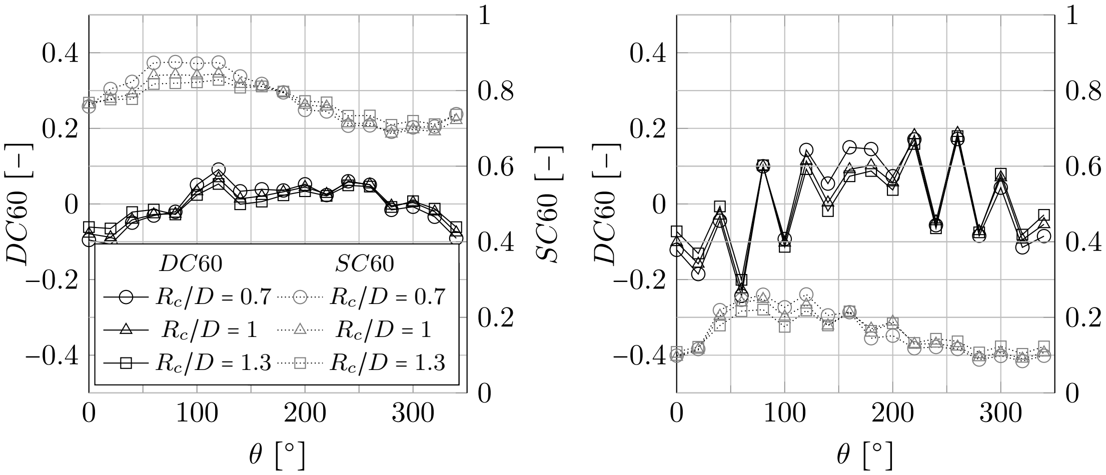

(a) Inlet - A

(b) EGV-Exit - C

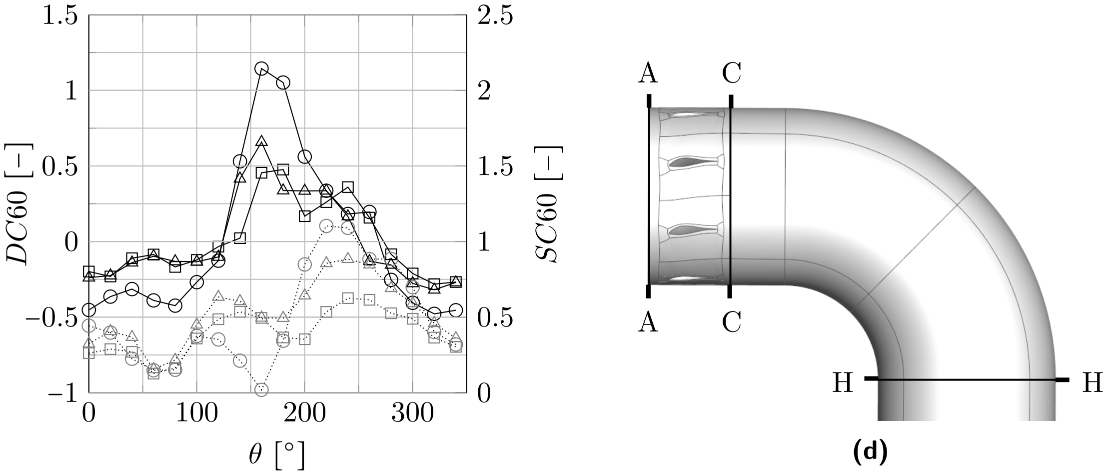

(d)

(c) 90° - H

Figure 4.16: Asymmetry parameters $DC60$ and $SC60$ at different aerodynamic interface planes

distortion and swirl, respectively. The circumferential distributions of $DC60$ and $SC60$ are calculated from the TRACE results at three aerodynamic interface planes: at the inlet, the EGV exit and after the bend. Three different bend radii are used, with R_c/D = 0.7, 1 and 1.3. The results are presented in Fig. 4.16a-4.16c, together with a definition of the aerodynamic interface planes in Fig. 4.16d.

While the average swirl at the inlet is positive, the circumferential variation, caused by the upstream effect of the Dean vortices, increases with decreasing bend radius R_c/D. The exit guide vanes remove most of the swirl, decreasing the average value of $SC60$ towards zero with only little swirl left. The circumferential variation, however, persists at the EGV exit and increases through the bend under the effect of the counter-rotating Dean vortices. This effect leads to strong secondary flows after the bend and increases further with smaller bend radii.

As secondary flows are a direct consequence of the driving pressure gradients, they increase with higher pressure distortions. From the $DC60$ distribution, it can be seen how pressure distortions, caused by the bend, exist upstream of the EGV and strongly increase through the duct. This effect is stronger for smaller R_c/D. The wake from the exit guide vanes can be seen in the periodic profile of the $DC60$ at the EGV exit in Fig. 4.16b and is similar for all calculated R_c/D.

4.2.3 Distance between the EGV and the bend

Due to the mutual influence of the EGV, the plug and the bend, the effect of the distance between these components on the flow field is investigated by varying the length between the EGV outlet and the bend, l/D. In order to find the influence of l/D on flow expansion and separation along the upper and lower duct sides, l/D is varied in steps. The corresponding flow fields and pressure losses are then calculated in TRACE. The resulting pressure losses for distances between l/D=0.1 and l/D=0.5 are listed in Table 4.3.

$R_c/D\,[-]$	$l/D\,[-]$	$\zeta_{v_{rel}}\,[-]$
1	0.5	0.930
1	0.4	0.984
1	0.3	1
1	0.2	1.124
1	0.1	1.212

Table 4.3: Pressure losses for different distances between the EGV and the bend, l/D

A close relation is observed between pressure losses and the distance l/D, with pressure losses increasing for smaller distances between the EGV and the bend. For larger l/D, the plug protrudes less into the bend. Both the expansion from an annular to a circular cross-section along the plug and the convex side of the bend represent zones susceptible to flow separation. The mutual influences of both zones make the distance l/D a crucial parameter for the aerodynamic efficiency. Higher values of l/D put the bend out of the flow expansion zone, decreasing the adverse pressure gradient in the bend. The flow therefore stays attached longer, leading to smaller separated regions and pressure losses. However, some exceptions of this rule can occur due to the complex interactions between different regions of flow separation and the increased friction losses for longer duct lengths. This is for example the case for $l/D = 0.3$, which presents a local minimum in pressure losses for $R_c/D = 1$. This could be due to a beneficial effect of the plug separation on the boundary layer on the convex side.

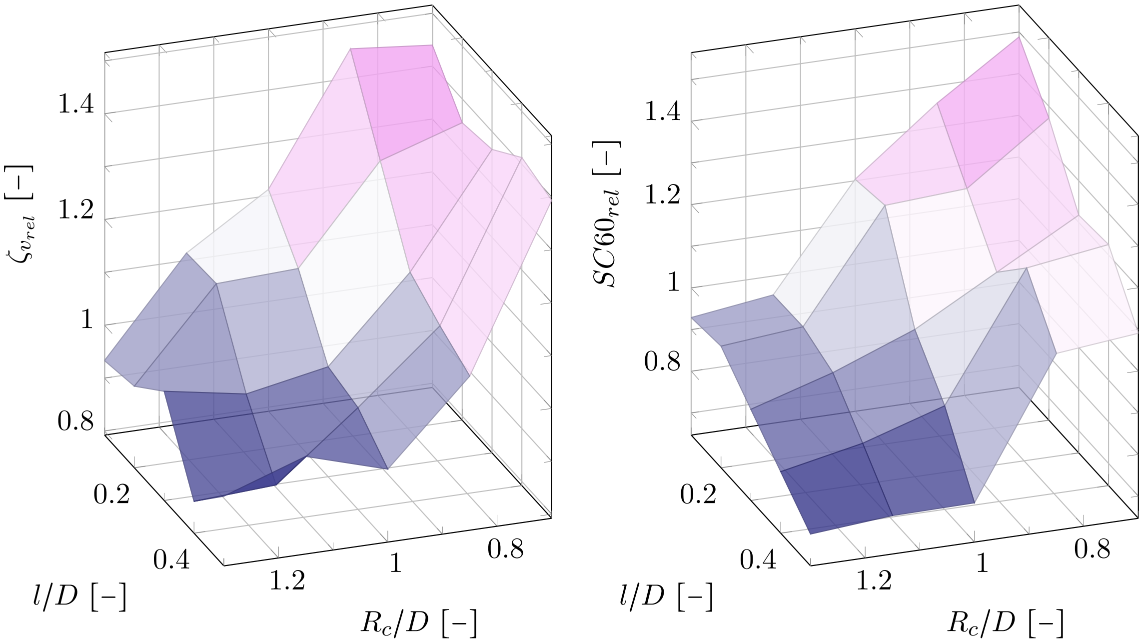

(a) Pressure losses **(b)** Asymmetry in Inlet Flow

Figure 4.17: Pressure loss and inflow asymmetry shown for different combinations of R_c/D and l/D

The combined influence of l/D and R_c/D on the pressure losses is shown in Fig. 4.17a. It presents the general trend of increasing pressure losses for smaller bend radii and smaller distances between the EGV and the bend. Some outliers exist, due to mutual effects of individual separation regions that can lead to local minima or maxima in the aerodynamic efficiency. The combined effect of both l/D and R_c/D on the inlet flow asymmetry is shown in Fig. 4.17b. It can be observed how both shorter distances l/D and smaller bend radii lead to a decrease in the inlet flow symmetry by increasing the upstream effect of the bend. The plotted quantity $SC60_{rel}$ is defined in Equ. 4.1 and gives an indication of the maximum swirl variation, when compared to the reference case with $R_c/D = 1$ and $l/D = 0.3$.

$$SC60_{rel} = \frac{SC60_{max} - SC60_{min}}{SC60_{max_{ref}} - SC60_{max_{ref}}} \tag{4.1}$$

4.2.4 Effect of swirl

As mentioned in Chapter 2, several studies and experiments conducted in the past confirm that swirl can decrease pressure losses in a curved duct. This increase in the aerodynamic efficiency is achieved by transporting more fluid towards the walls and delaying separation. At the same time, swirl decreases the relative angle between the flow and the streamwise adverse pressure gradient, further decreasing the risk of flow separation. However, minimizing pressure losses is not the only requirement of an EGV followed by a duct. The main task of the EGV in an aircraft engine is removing swirl and minimizing secondary flows. High streamwise total pressure is required that can be transformed into kinetic energy in the nozzle. Only the streamwise component of the dynamic pressure is therefore considered, as secondary flows with non-constant swirl after the bend are difficult to transform into propulsive energy. The streamwise total pressure is defined and non-dimensionalized in Equ. 3.10.

In order to investigate the effect of swirl on the duct flow, pressure losses and streamwise total pressure at the outlet, a slightly varied EGV geometry is constructed. The new EGV airfoils are designed to only slightly straighten the flow, leaving 10° of residual swirl. Figures 4.18 and 4.19 show the absolute velocities calculated with TRACE at y =0 for the duct geometry with R_c/D=1, comparing 0° and 10° of residual swirl.

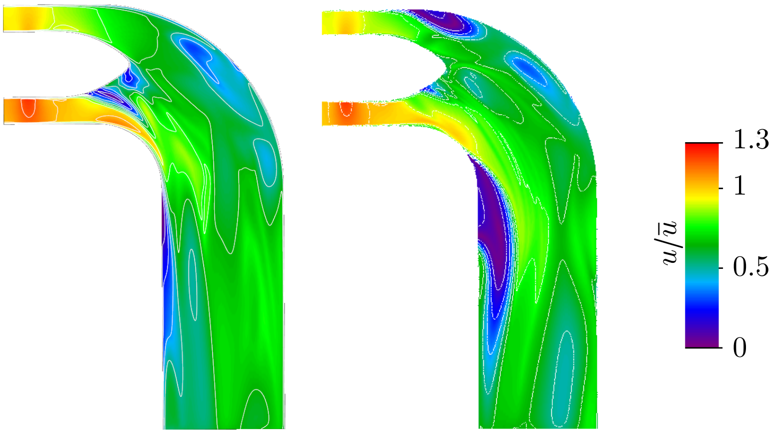

(a) α_2 = 0° **(b)** α_2 = 10°

Figure 4.18: Absolute flow velocity for different swirl angles at the EGV exit

When looking at Fig. 4.19, it appears that the residual swirl of 10° at the EGV exit is further increased along the plug walls due to the rapid decrease in hub diameter. This can also be seen from Fig. 4.19d, where a small vortex forms towards the tip of the plug. The increase in swirl energizes the flow close to the plug wall and decreases the effective angle with the adverse pressure gradient, making the boundary layer less susceptible to flow separation. Along the outer duct walls, the local swirl, while not being increased, also leads to a higher total flow velocity and smaller angle with the adverse pressure gradient, delaying separation at the outer walls. However, without swirl (α_2 = 0°) the separation zone at the lower plug side is essentially decreasing the cross-sectional area, accelerating the flow around the convex wall. This effect is missing for the case of α_2 = 10° swirl, leading to a larger separation zone on the convex side of the duct. The effect of swirl is increased at the hub, where it is not desired.

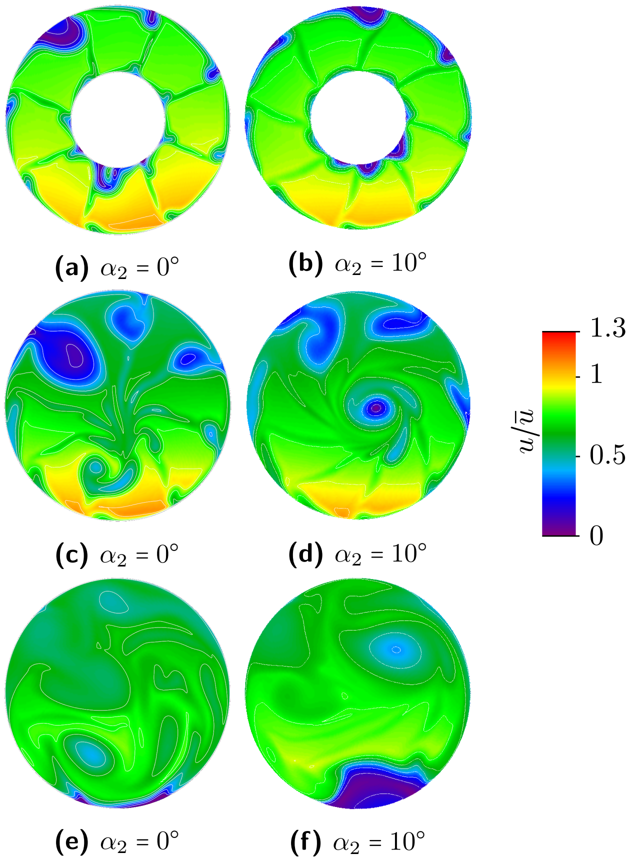

Figure 4.19: Absolute flow velocity for curved duct ($R_c/D = 1$) without residual swirl (left) and with a residual swirl of $\alpha = 10°$ (right). First row (**(a)**-**(b)**) at position $\phi = 0°$, second row (**(c)**-**(d)**) at $\phi = 30°$ and third row (**(e)**-**(f)**) at $\phi = 90°$

By following the plug longer without separating, more fluid is transported to the center of the duct, leading to lower velocities and increased flow separation on the convex wall. When comparing the total losses for the duct with a bend radius of $R_c/D = 1$, Table 4.4 shows higher overall losses for the case with $\alpha_2 = 10°$. Additionally, the EGV with complete swirl removal ($\alpha_2 = 0°$) leads to a higher streamwise total pressure at the exit. While swirl has been found to improve efficiency in many curved duct flow applications, the presence of the conical plug negates its positive effect for this configuration with $R_c/D = 1$. In engine applications where axial thrust is desired, the presence of secondary flow structures in the outlet can also represent a decrease in performance.

At sharper bend radii R_c/D, however, swirl can still prove beneficial. Table 4.4 shows the results calculated in TRACE for $R_c/D = 0.7$, 0.85 and 1, each with 0° and 10° residual swirl. For a bend sharpness of $R_c/D = 0.85$ a swirl of $\alpha = 10°$ improves the overall efficiency by decreasing the total pressure losses. However, streamwise total pressure at the exit is less than without swirl. When the radius is decreased further, the beneficial effect of swirl on the pressure losses becomes more dominant and even leads to higher streamwise total pressure at the outlet. This can be seen from Table 4.4 for $R_c/D = 0.7$, where pressure losses decrease by about 10% and streamwise total pressure at the exit is higher than without residual swirl.

$R_c/D\,[-]$	α_2	$\zeta_{v_{rel}}\,[-]$
1	0°	1
1	10°	1.036
0.85	0°	1.187
0.85	10°	1.151
0.7	0°	1.446
0.7	10°	1.324

Table 4.4: Total loss factors with and without complete swirl removal by the EGV

While for $R_c/D = 1$ swirl decreases both the aerodynamic efficiency and the total propulsive energy, swirl proves efficient for very sharp bends of compact, lightweight configurations with $R_c/D \leqq 0.7$.

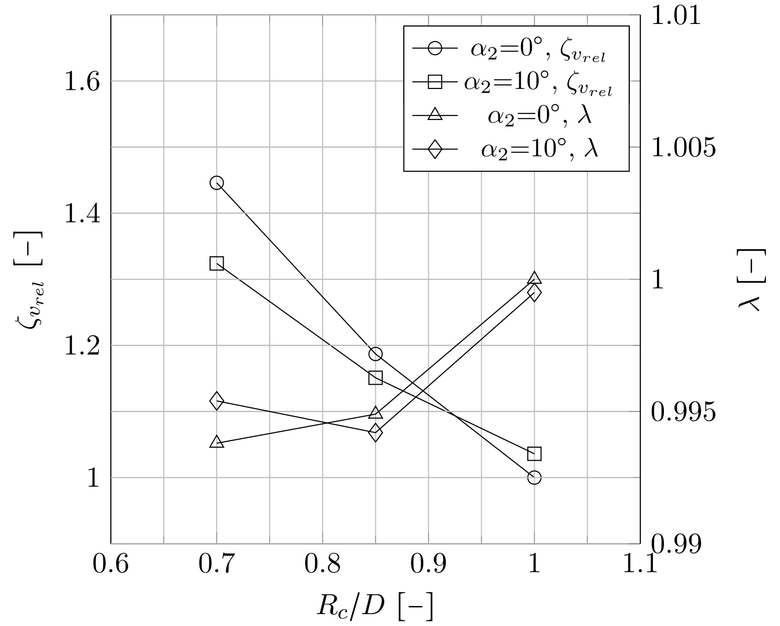

Figure 4.20: Effect of residual swirl on loss factor and streamwise total exit pressure for different R_c/D

4.2.5 Circumferential EGV positioning

During the aerodynamic analysis of the EGV with a curved duct, it is observed that the wake resulting from the vanes plays a critical role in the development of flow separation and pressure losses. This section therefore investigates the effect of the circumferential positioning of the exit guide vanes on the flow field. By varying the circumferential positions of the individual vanes, low velocity wakes are shifted to zones with lower adverse pressure gradients where separation is less likely to occur. In order to reduce design complexity and manufacturing cost to a minimum, the airfoil shape, blade angle and distance between two adjacent vanes is kept constant for all vanes. The only variation allowed is a uniform rotation (θ_{EGV}) of all vanes in circumferential direction θ.

In order to explore the whole design space, only the angular distance between two consecutive vanes needs to be analyzed, due to the periodicity of the geometry. With a total of eight vanes, the EGV geometry is therefore rotated in steps from $\theta_{EGV} = -22.5°$ to $\theta_{EGV} = 22.5°$ and the corresponding flow fields and pressure losses are calculated using TRACE. The resulting loss factors are shown in Fig. 4.21. A general increase in efficiency can be seen from $\theta_{EGV} = -22.5°$ towards $\theta_{EGV} = 17.5°$ with an optimum at $\theta_{EGV} = 17.5°$. Some outliers show the high sensitivity of the flow around the convex wall to small changes in the EGV wake position, leading to earlier flow separation and considerably increased pressure losses. Generally, however, it can be concluded that a slight asymmetric positioning of the vanes can have a positive effect on the aerodynamic efficiency of the duct.

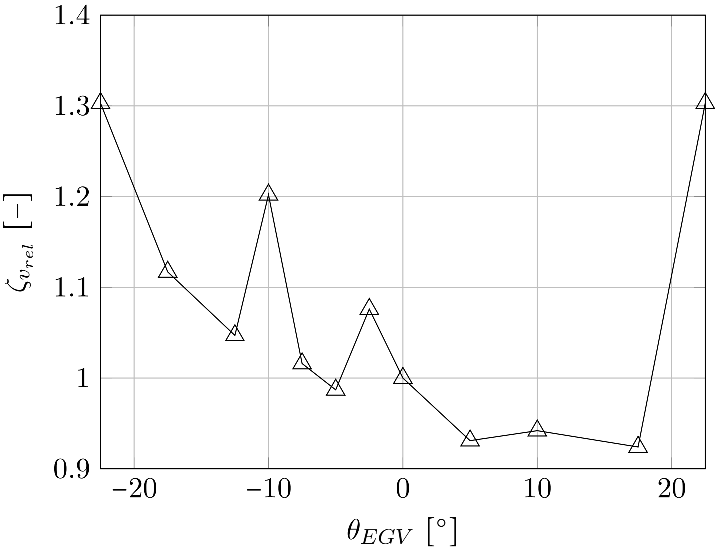

Figure 4.21: Loss factor for different circumferential guide vane positioning (rotated around the x-axis by θ)

To investigate the underlying effect of this change in the aerodynamic efficiency, the absolute flow velocities are compared for the standard geometry and a geometry where the vanes are uniformly rotated by $\theta_{EGV} = 17.5°$ around the x-axis. The resulting flow fields are shown at different streamwise positions in Fig. 4.22. It can be observed how the flow field with

$\theta_{EGV} = 17.5°$ is more symmetric and shows less flow separation, leading to the lower pressure losses presented in Fig. 4.21. Low velocity zones are more evenly distributed, avoiding large separation zones. This can be explained by the influence of θ_{EGV} on the aerodynamic blade loading and local adverse pressure gradient. Generally, as shown in Section 4.1.3, the blade loading is highest on the top left side, when viewed from the front, due to the upstream effect of the Dean vortices. This results in stronger wakes from the higher loaded vanes and a flow that is more susceptible to separation. By rotating the EGV slightly, the aerodynamic loading is decreased locally. At the same time, the vane is moved away from the concave side and to an area of smaller adverse pressure gradient. Both effects lead to a decrease in flow separation behind the vane. If rotated too far, however, the following vane will experience a high aerodynamic loading and adverse pressure gradient. An optimum has therefore to be found as presented in Fig. 4.21.

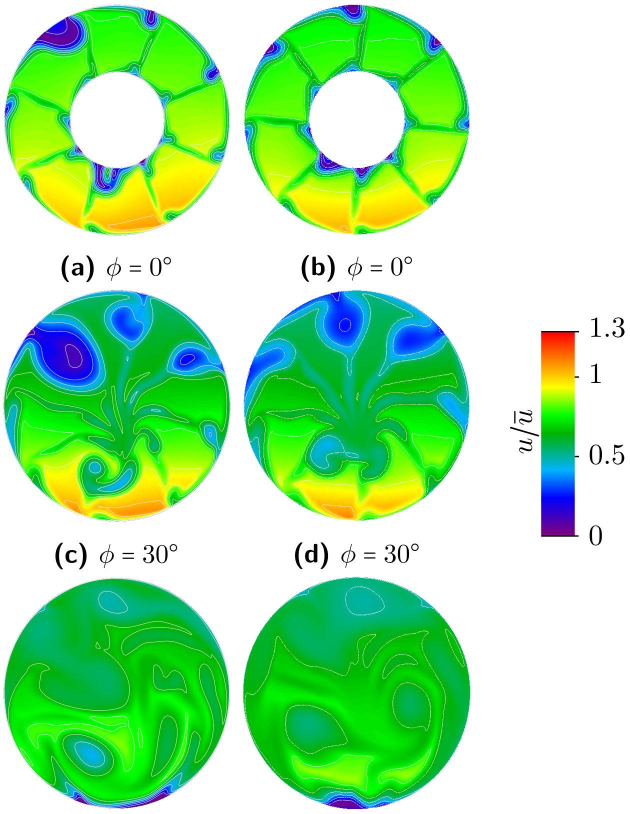

(a) $\phi = 0°$ **(b)** $\phi = 0°$

(c) $\phi = 30°$ **(d)** $\phi = 30°$

(e) $\phi = 90°$ **(f)** $\phi = 90°$

Figure 4.22: Absolute flow velocity for curved duct ($R_c/D = 1$) with symmetrical vane positioning (left) and $\theta_{EGV} = 17.5°$ (right) at different streamwise cross-sections (ϕ)

4.2.6 Plug shape

With a constant outer radius throughout the whole cylindrical duct, the decrease in inner radius at the plug leads to an increase in cross-sectionl area. This flow expansion results in a strong adverse pressure gradient, promoting a tendency for the flow to separate at the walls. At the same time, the curved duct accelerates the flow around the convex side of the bend and leads to an area of high pressure on the concave side of the duct, where - by the combination of a large cross-sectional area increase and bending of the flow - a considerable area of separated flow develops. The flow also separates at the lower side of the plug, where the flow is bend around the convex side of the duct and does not follow the entire plug geometry bending upwards. A third area of separation develops just after the bend on the convex side, where the flow is not able to follow the highly curved geometry. Together, these regions of separated flow lead to a loss of about 1.5% in total pressure, when compared to the straight duct reference geometry.

A variation in the plug geometry is therefore investigated to reduce the pressure losses with minimum weight increase. Seeing that the large and sudden increase in cross-sectional area is to a large part responsible for the occurring separation at the plug and concave side of the bend, different plugs are designed to minimize this effect. It is shown that a plug with increased length and curvature, decreasing the rate of flow expansion and pressure rise, can decrease separation at the inner plug and concave duct side considerably.

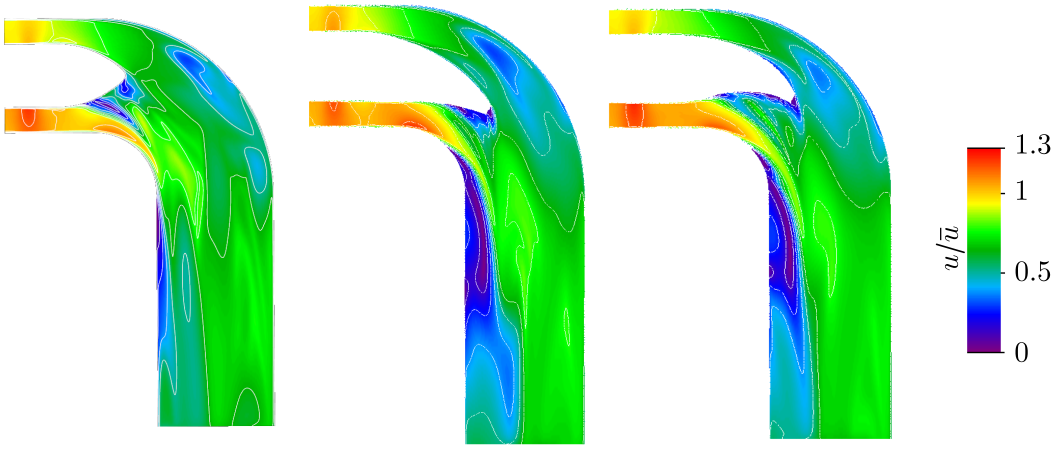

(a) standard plug

(b) variation 1

(c) variation 2

Figure 4.23: Absolute flow velocity for different spinner geometries

	$\zeta_{v_{rel}}$ [−]
Base plug	1
Long plug	0.964
Upper curv. plug	0.910

Table 4.5: Pressure losses for individual plug shapes

Figure 4.23a presents this effect by showing the decrease in separated flow regions compared to the original geometry in Fig. 4.23b. A more pronounced plug curvature towards the outer side of the bend, as shown in Fig. 4.23c, decreases the length of the separated area on the concave side further by decreasing the local flow expansion. More detail of the occurring separation zones on the concave and convex sides of the duct is shown in Fig. 4.24. The cuts are taken at positions just before the bend ($\phi = 0°$), along the bend and at its end ($\phi = 90°$), as indicated in the figure. Figure 4.24a shows the early separation due to the expansion and large adverse pressure gradient on the concave side of the bend. The cuts in Figures 4.24b to 4.24e show how this separation is delayed and decreased in size due to the slower expansion along a longer plug, represented by the white plug cross-section in the center. Flow separation on the convex side occurs slightly earlier for the longer plug shapes (Fig. 4.24g-4.24l). A similar effect could be achieved by employing a non-constant bend radius to allow for a more gradient expansion. Table 4.5 shows the differences in pressure loss for the individual plug shapes.

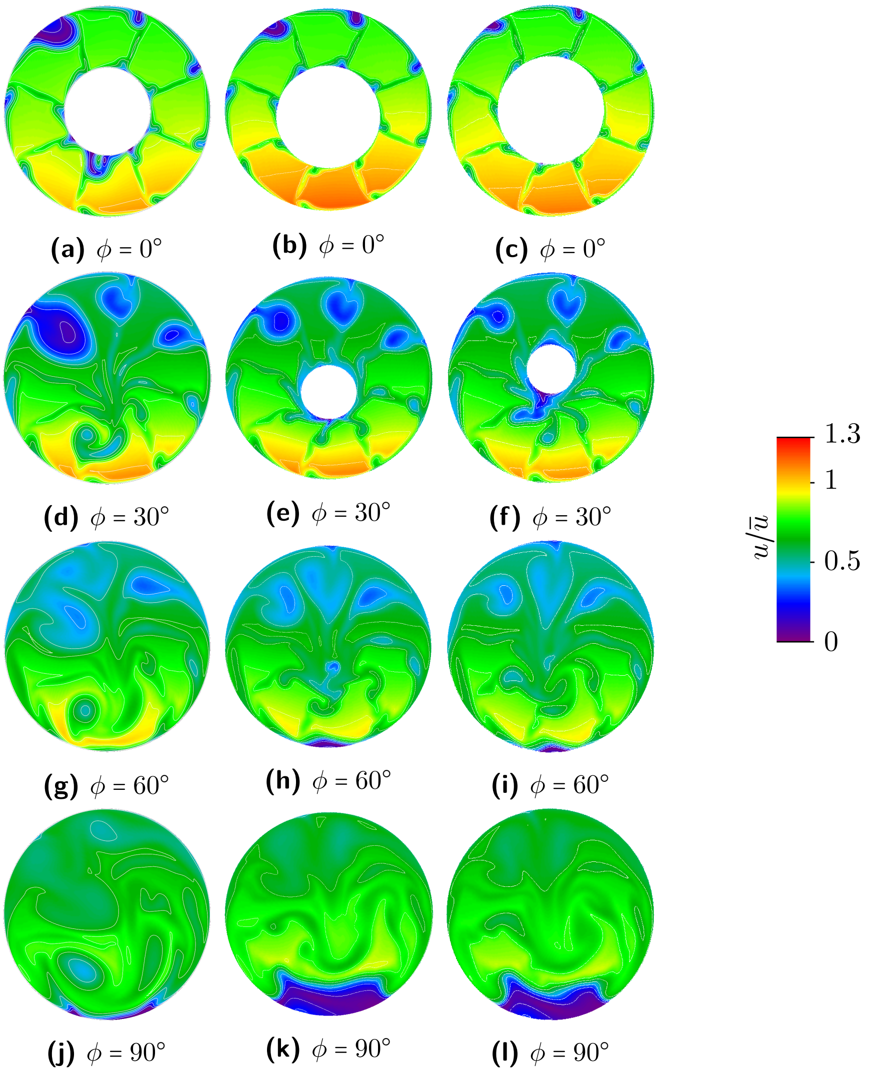

(a) $\phi = 0°$ **(b)** $\phi = 0°$ **(c)** $\phi = 0°$

(d) $\phi = 30°$ **(e)** $\phi = 30°$ **(f)** $\phi = 30°$

(g) $\phi = 60°$ **(h)** $\phi = 60°$ **(i)** $\phi = 60°$

(j) $\phi = 90°$ **(k)** $\phi = 90°$ **(l)** $\phi = 90°$

Figure 4.24: Absolute flow velocity for standard plug, increased length plug and plug with pronounced upper curvature (columns left to right) at different streamwise positions (ϕ) along the bend

4.3 Comparison of SU2 with TRACE results

During the whole aerodynamic study, the validated industry solver TRACE is used as the main tool for numerical analysis. In order to obtain a second numerical solution and an impression of the solution's independence of the solver, the curved duct EGV flow is also computed with the open-source solver SU2. This section gives an overview of the SU2 solution for the EGV flow problem with curved duct, compares it to the TRACE solution and discusses differences in the resulting flow fields.

During the validation in Section 3.5, SU2 has been used to calculate the test case of a curved duct flow and to compare the results with both experimental data and the solution obtained from TRACE. From the test case, SU2 is found to yield an earlier point of separation and later point of reattachment, leading to a larger separation area on a curved geometry. While TRACE is run with a typical configuration for internal flow problems, using the Wilcox $k-\omega$ turbulence model, SU2 does not yet include the option for this model. Instead, SU2 incorporates the Menter Shear Stress Transport (SST) model [16], a two-equation model that combines the traditional $k-\omega$ and $k-\epsilon$ models. For adverse pressure gradients in boundary layers, the traditional $k-\omega$ model tends to overestimate the shear stress and delays separation [55]. The newer SST model has been found to be less susceptible to these problems.

Figure 4.25 compares the absolute velocity fields obtained by TRACE and SU2 on the combined geometry of the EGV and the curved duct at $\phi = 0°$. The general pattern of separation occurring on the concave wall and lower plug side are obtained by both solvers. Both TRACE and SU2 show a non-symmetrical separation pattern with the largest area of separation on the left upper side (in Fig. 4.25). This behavior, as discussed in Section 4.1.3, is due to the Dean vortices leading to an inhomogeneous swirl angle, blade loading and EGV wake. The wake itself, as shown in Fig. 4.25, shows different behavior for both solvers. While the flow stays attached to the vanes in the TRACE solution, SU2 yields significant flow separation, starting from the hub side. This leads to stronger and more distorted wakes, as presented in Fig. 4.25. This behavior is assumed to result from the difference in turbulence model, as the $k-\omega$ model has been found to underestimate separation, as mentioned above.

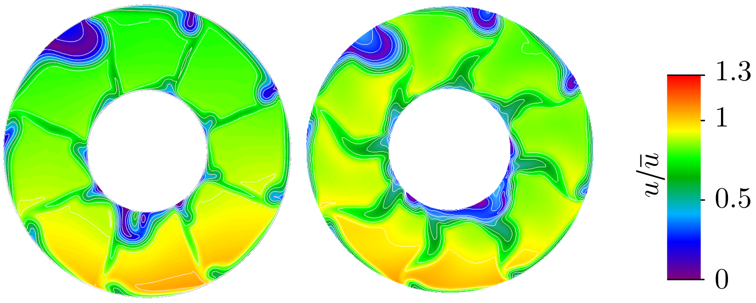

(a) TRACE **(b)** SU2

Figure 4.25: Absolute flow velocity obtained using the solvers SU2 and TRACE at $\phi = 0°$

The high sensitivity of the concave wall separation on the turbulence model becomes visible in Fig. 4.26. While the TRACE results show only little flow separation, the solution obtained by SU2 yields a considerably larger area of separation and earlier separation point.

The pressure disturbances occurring after the bend (at $\phi = 90°$) for TRACE and SU2 are

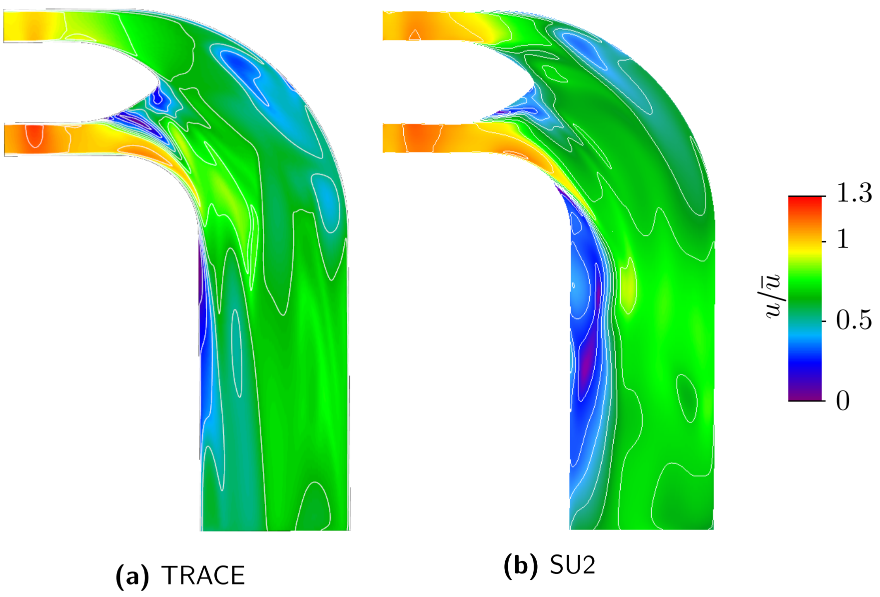

(a) TRACE

(b) SU2

Figure 4.26: Absolute flow velocity obtained using the solvers SU2 and TRACE at $y = 0$

shown in Fig. 4.27. It can be seen how areas of larger and smaller pressure perturbations, a measure of flow homogeneity and secondary flow strength, coincide. The calculations run with both TRACE and SU2 therefore yield similar secondary flow patterns.

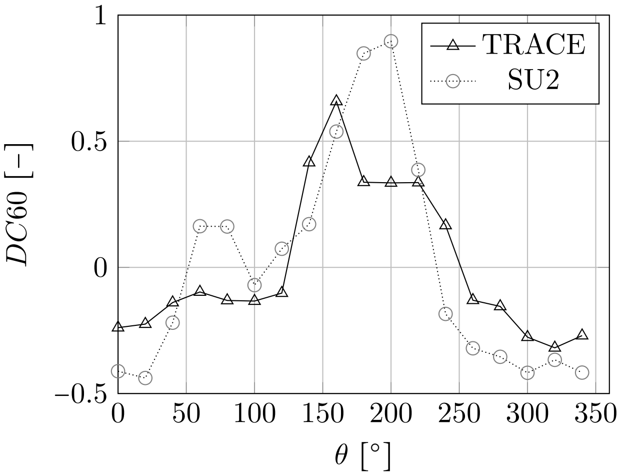

Figure 4.27: Comparison of circumferential $DC60$ distribution after the bend ($\phi = 90°$) for TRACE and SU2

The comparison of the two different solvers and turbulence models shows the strong sensitivity of flow separation to changes in the numerical scheme and turbulence model (Fig. 4.25 and 4.26). The main findings of this report, however, regarding the effect of R_c/D, l/D, swirl, plug shape and circumferential vane positioning, are of a qualitative nature and remain valid. The same main separation regions (Fig. 4.26) and secondary flow effects (Fig. 4.25 and 4.27) are found using both TRACE and SU2. The total pressure loss found in SU2 amounts to 96.9% of the value calculated in TRACE (Table 4.6). When used for more detailed geometry optimization of a curved duct geometry, further validation and testing of different turbulence models is recommended.

	$\zeta_{v_{rel}}$ [−]
TRACE	1
SU2	0.969

Table 4.6: Pressure losses obtained from TRACE and SU2

Chapter 5

Conclusion and Recommendations

5.1 Conclusion

From the results it is concluded that the method described in Chapter 3 presents an efficient way of investigating the aerodynamic flow phenomena occurring in an EGV with curved duct. Using a structured multi-block mesh and the RANS solver TRACE allows to calculate the flow field through the complex 360° geometry at a high Reynolds number ($Re \sim 10^6$) with reasonable computational cost and time. The parametric mesh provides a method to investigate the effect of different geometric parameters on the aerodynamic efficiency without extensive re-meshing. By validating the solver with experimental data from literature, it is shown that flow phenomena are resolved with sufficient accuracy in TRACE. From the comparison of TRACE and SU2, it is found that the curved internal flow shows a high sensitivity to the numerical treatment and turbulence model. The $k-\omega$ model used during the TRACE analysis, however, shows good agreement with experimental results during validation. During the subsequent analysis and sensitivity study, the research questions presented in Chapter 3 could therefore be answered. Compared to the flow field of an EGV with straight duct, the elbow duct is found to introduce separation zones on both the concave and convex sides of the bend, leading to significantly higher losses. Two counter-rotating vortices (called Dean vortices [4]) are observed in the curved duct, also influencing the flow field upstream of the EGV and leading to an asymmetric swirl and incidence angle. This results in a locally non-optimal design of the EGV blades.

During the sensitivity analysis it is shown that increasing either the radius of the bend or the distance between the EGV and the bend leads to a decrease in separation and pressure losses, but increases the overall duct length and weight. While swirl can generally increase the aerodynamic efficiency in curved duct by avoiding flow separation, it only provides an advantage for very small bend radii, due to its effect on streamwise total pressure and propulsive energy at the exit. Other methods of improving the aerodynamic efficiency without increasing weight are circumferential rotation of the EGV and changing the plug shape. Rotating the EGV in circumferential direction into a non-symmetric position can decrease the effect of the Dean vortices and lead to a more symmetric wake. Modifying the plug shape provides the means to achieve a smoother flow expansion, decreasing the risk of flow separation.

5.2 Recommendations

With the results presented and research questions answered, this section gives recommendations for the EGV design with a curved duct and provides an outlook for further research.

From an aerodynamic point of view, both R_c/D and the length between the EGV and the bend (l/D) should be as high as possible to limit pressure losses and increase the aerodynamic efficiency. Values of $R_c/D < 1$ should be avoided and the distance between the EGV and the bend be at least $l/D = 0.3$. While more compact designs can save weight, pressure losses rise considerably for such designs. In the case of very small bend radii with $R_c/D < 0.8$, it should be considered to not completely remove swirl in the EGV, in order to energize the boundary layer in the bend. For small bend radii, swirl can increase both the aerodynamic efficiency and the streamwise total pressure at the exit. Furthermore, the EGV should be rotated in circumferential direction until a symmetric wake pattern is achieved to minimize flow separation. The optimum angle of rotation depends on both the inflow profile and the residual swirl behind the EGV. In the example studied, a rotation from the symmetric position of $\theta_{EGV} = 17.5°$ presents an optimum in terms of the aerodynamic efficiency. If the EGV is produced from one piece, independent aerodynamic design of the individual vanes should be possible without a large increase in production or maintenance cost. This allows to adapt the EGV profiles to the inhomogeneous swirl angle caused by the upstream effect of the bend. The tailoring of the individual vane's geometry to the local flow angle and velocity leads to a more symmetric wake originating from the EGV, thereby decreasing separation and pressure losses in the bend. Changing the shape of the EGV thereby provides a weight-efficient way of increasing the aerodynamic efficiency without adding duct length.

For future studies it is recommended to further increase the design space by considering duct geometries of non-constant radius R_c and outer diameter D. This allows to control the flow expansion rate to delay flow separation more efficiently. Additionally, the plug shape should be studied and refined further. However, simple plug geometries are preferred from a production cost point of view.

References

[1] www.ihs.com. Jane's aero-engines database. *accessed on 21.02.2017*, 2017.

[2] Willy J. G. Braeunling. *Flugzeugtriebwerke*. Springer Vieweg, 2015.

[3] Steven J. Hulshoff. *Computation and Modelling of Turbulence, Lecture Notes AE4132 CFD II Part 2*. Faculty of Aerospace Engineering, Delft University of Technology, 2015.

[4] W. R. Dean and J. M. Hurst. Note on the motion of fluid in a curved pipe. *Mathematika*, 6:77–85, 1959.

[5] L. Tan, B. Zhu, Y. Wang, S. Cao, and K. Liang. Turbulent flow simulation using large eddy simulation combined with characteristic-based split scheme. *Computers & Fluids*, 94:161–172, 2014.

[6] D. S. Miller. *Internal Flow Systems*. BHRA, Cranfied, Bedford, UK, 1991.

[7] K. Sudo, M. Sumida, and H. Hibara. Experimental investigation on turbulent flow in a circular-sectioned 90-degree bend. *Experiments in Fluids*, 25:42–49, 1998.

[8] A. Ono, N. Kimura, H. Kamide, and A. Tobita. Influence of elbow curvature on flow structure at elbow outlet under high reynolds number condition. *Journal of Aerospace Engineering*, 241:4409–4419, 2011.

[9] P. Cardamone. *Aerodynamic Optimisation of Highly Loaded Turbine Cascade Blades for Heavy Duty Gas Turbine Applications*. Bundeswehr University Munich, Faculty of Aerospace Engineering, Department for Jet Propulsion, 2005.

[10] www.pointwise.com. Pointwise: Mesh generation software for cfd. *accessed on 20.02.2017*, 2017.

[11] www.innovative cfd.com. Section on structured grids. *accessed on 19.02.2017*, 2017.

[12] Cecil G Armstrong, Harold J Fogg, Christopher M Tierney, and Trevor T Robinson. Common themes in multi-block structured quad/hex mesh generation. *Procedia Engineering*, 124:70–82, 2015.

[13] Kai Becker, Kathrin Heitkamp, and Edmund Kuegeler. Recent progress in a hybrid-grid cfd solver for turbomachinery flows. In *Proc. 5th European Conference on Computational Fluid Dynamics ECCOMAS CFD*, 2010.

[14] www.liu.se/mai/bm/forskning. Research at computational mathematics - linkoeping university. *accessed on 23.02.2017*, 2017.

[15] N Crawford, S Spence, A Simpson, and G Cunningham. A numerical investigation of the flow structures and losses for turbulent flow in 90° elbow bends. *Proc. IMechE*, 223:27–45, 2008.

[16] Francisco Palacios, Michael R. Colonno, Aniket C. Aranake, Alejandro Campos, Sean R. Copeland, Thomas D. Economon, Amrita K. Lonkar, Trent W. Lukaczy, Thomas W. R. Taylor, and Juan J. Alonso. Stanford university unstructured (su2): An open-source integrated computational environment for multi-physics simulation and design. In *Proc. 51st AIAA Aerospace Sciences Meeting including New Horizons Forum and Aerospace Exposition (Dallas, Texas, January 2013)*. Stanford University, 2013.

[17] L. Helin, L. Thais, and G. Mompean. Numerical simulation of viscoelastic dean vortices in a curved duct. *Journal of Non-Newtonian Fluid Mechanics*, 156(1-2):84–94, 2009.

[18] Frans T.M. Nieuwstadt, Jerry Westerweel, and Bendiks J. Boersma. *Turbulence, Introduction to Theory and Applications of Turbulent Flows*. Springer, 2016.

[19] F. M. White. *Viscous fluid flow*. McGraw-Hill, Inc., 1991.

[20] E. Tulapurkara, A. Khoshnevis, and J. Narasimhan. Wake-boundary layer ineteraction subject to convex and concave curvatures and adverse pressure gradient. *Experiments in Fluids*, 31(6):697–707, 2001.

[21] E. Fried and I. E. Idelchik. *Flow Resistance: A Design Guide for Engineers*. Hemisphere Publishing Corporation, 1989.

[22] M. Tanaka and H. Ohshima. Numerical investigation on large scale eddy structure in unsteady pipe elbow flow at high reynolds number conditions with large eddy simulation approach. *Journal of Power and Energy Systems*, 6(2):210–228, 2012.

[23] A. Kalpakli, R. Oerlue, N. Tillmark, and H. Alfredsson. Pulsatile turbulent flow through pipe bends at high dean and womersley numbers. *Journal of Physics: Conference Series*, 318:092023, 2011.

[24] M. M. Enayet, M. M. Gibson, A. M. K. P. Taylor, and M. Yianneskis. Laser-doppler measurements of laminar and turbulent flow in a pipe bend. *International Journal of Heat and Fluid Flow*, 3(4):213–219, 1982.

[25] T. Kawamura, T. Nakao, and M. Takahashi. Reynolds number effect on turbulence downstream from elbow pipe. *Transactions of the Japan Society of Mechanical Engineers Series B*, 68(667):645–651, 2002.

[26] T. Shiraishi, H. Watakabe, H. Sago, M. Konomura, A. Yamaguchi, and T. Fujii. Resistance and fluctuating pressures of a large elbow in high reynolds numbers. *Journal of Fluids Engineering*, 128(5):1063–1073, 2006.

[27] J. Pruvost, J. Legrand, and P. Legentilhomme. Numerical investigation of bend and torus flows, part i: effect of swirl motion on flow structure in u-bend. *Chemical Engineering Science*, 59:3345–3357, 2004.

[28] J. Kim, M. Yadav, and S. Kim. Characteristics of secondary flow induced by 90-degree elbow in turbulent pipe flow. *Engineering Applications of Computational Fluid Mechanics*, 8(2):229–239, 2014.

[29] Philip A. J. Mees, K. Nandakumar, and J. H. Masliyah. Instability and transitions of flow in a curved square duct: the development of two pairs of dean vortices. *Journal of fluid mechanics*, 314:227–246, 1996.

[30] Kougen Ozaki and Hiroshi Maekawa. Curvature effects in the curved duct for the compressible viscous flow. In *Proc. 24th International congress of the aeronautical sciences (2004)*. Hiroshima University, 2004.

[31] C. Muench and O. Metais. Large eddy simulations in curved square ducts: variation of the curvature radius. *Journal of Turbulence*, 8(28), 2007.

[32] X.-L. Luo. Operator-splitting computation of turbulent flow in an axisymmetric 180 degree narrowing bend using several k-ϵ models and wall functions. *International journal for numerical methods in fluids*, 22:1189–1205, 1996.

[33] Jiang Luo and Budugur Lakshminarayana. Prediction of strongly curved turbulent duct flows with reynolds stress model. *AIAA Journal*, 35(1):91–98, 1997.

[34] J. Ma, F. Wang, Yu Xin, and Z. Liu. A partially averaged navier-stokes model for hill and curved duct flow. *Journal of Hydrodynamics*, 23(4):466–475, 2011.

[35] Jeremy Gartner and Michael Amitay. Effect of boundary layer thickness on secondary structures in a short inlet curved flow. *International Journal of Heat and Fluid Flow*, 50:467–478, 2014.

[36] Valery Solodov, Juriy Starodubtsev, Boris Isakov, and Valentin Fedan. Experimental and numerical study of gas dynamics of exhaust pipe gas turbine unit. *Journal of Thermal Science*, 13(1):34–39, 2013.

[37] B. Majumdar, R. Mohan, S. N. Singh, and D. P. Agrawal. Experimental study of flow in a high aspect ratio 90 deg curved diffuser. *Journal of Fluids Engineering*, 120(1):83–89, 1998.

[38] U. Roh, S. J. Song, and J. H. Im. Swirl effect on the flow field in a bent duct. In *Proc. 13th International Symposium on transport phenomena and dynamics of rotating machinery*, 2010.

[39] D. J. Cerantola and A. M. Birk. Experimental analysis of swirl in short annular diffusers with negative wall angles. *ASME Turbo Expo 2014*, 2A:paper no. GT2014–25563, 2014.

[40] A. Maqsood and A. M. Birk. Improving the performance of a bent ejector with inlet swirl. *ASME Turbo Expo 2008*, 6:23–32, 2008.

[41] Jing-Lun Fu and Jian-Jun Liu. Influences of inflow condition on non-axisymmetric flows in turbine exhaust hoods. *Journal of Thermal Science*, 17(4):305–313, 2008.

[42] S. Sun and R. Guo. Serpentine inlet performance enhancement using vortex generator based flow control. *Journal of Aeronautics*, 19:10–17, 2006.

[43] Hongtao Wang, Xiaocheng Zhu, and Zhaohui Du. Aerodynamic optimization for low pressure turbine exhaust hood using kriging surrogate model. *International Communications in Heat and Mass Transfer*, 37:998–1003, 2010.

[44] S. Lee, Saeil Lee, Kyu-Hong Kim, Dong-Ho Lee, Young-Seok Kang, and Dong-Ho Rhee. Optimization framework using surrogate model for aerodynamically improved 3d turbine blade design. *ASME Turbo Expo 2014*, 2B:paper no. GT 2014–26571, 2014.

[45] J. Backhaus, M. Aulich, C. Frey, T. Lengyel, and C Voss. gradient enhanced surrogate models based on adjoint cfd methods for the design of a counter rotating turbofan. *ASME Turbo Expo 2012*, 8:2319–2329, 2012.

[46] C. L. Dixon and C. A. Hall. *Fluid Mechanics and Thermodynamics of Turbomachinery.* Elsevier, 2010.

[47] N. Qin and X. Liu. Flow feature aligned grid adaptation. *Int. J. Numer. Methods Eng.*, 67(6):787–814, 2006.

[48] Zaib Ali, Paul G. Tucker, and Shahrokh Shahpar. Optimal mesh topology generation for cfd. *Computational Methods of Applied Mechanical Engineering*, 317:431–457, 2018.

[49] P. G. Tucker. Computation of unsteady turbomachinery flows: Part 1 - progress and challenges. *Progress in Aerospace Sciences*, 47:522–545, 2011.

[50] Yan Wang, Quanlin Dong, and Pengfei Wang. Numerical investigation on fluid flow in a 90 degree curved pipe with large curvature ratio. *Mathematical Problems in Engineering*, 2015.

[51] Huang Huang and Kivanc Ekici. An efficient harmonic balance method for unsteady flows in cascades. *Aerospace Science and Technology*, 29:144–154, 2013.

[52] L. He. Fourier methods for turbomachinery applications. *Progress in Aerospace Sciences*, 46:329–341, 2010.

[53] Michael B. Giles and Niles A. Pierce. An introduction to the adjoint approach to design. *Flow Turbulence and Combustion*, 65:393–415, 2000.

[54] Byung Joon Lee and Chongam Kim. Automated design method of turbulent internal flow using discrete adjoint formulation. *Aerospace Science and Technology*, 11:163–173, 2007.

[55] F. R. Menter. Zonal two equation k-ω turbulence models for aerodynamic flows. *AIAA Journal*, 32(8):1598–1605, 1994.

[56] Jiang Luo and Budugur Lakshminarayana. Analysis of streamline curvature effects on wall-bounded turbulent flows. *AIAA Journal*, 35(8):1273–1279, 1997.

[57] Gavin G. Lee, William D. E. Allan, and Kiari Goni Boulama. Flow and performance characteristics of an allison 250 gas turbine s-shaped diffuser: Effects of geometry variations. *International Journal of Heat and Fluid Flow*, 42:151–163, 2013.

[58] P. G. Tucker. Trends in turbomachinery turbulence treatments. *Progress in Aerospace Sciences*, 63:1–32, 2013.

[59] N. C. Bissinger and T. Breuer. *Encyclopedia of Aerospace Engineering - Volume 8 - Basic Principles - Gas Turbine Compatibility - Intake Aerodynamic Aspects*. John Wiley & Sons Ltd., 2010.

[60] N. R. Schmid, C. C. Leinos, and L. Fottner. Steady performance measurements of a turbofan engine with inlet distortions containing co- and counterrotating swirl from an intake diffuser for hypersonic flight. *Journal of Turbomachinery*, 123(2):379–385, 2000.